ROYAL SOCIETY
OF CHEMISTRY

REVIEW

Check for updates

Engineered cellulose-supported photocatalysts for clean energy and environmental remediation: progress and prospects

Akash Balakrishnan, [*a] Frency P. Mathew,[a] Milan Tom Joseph,[a] Mona Mary Varghese,[a] K. S. Aryamol,[a] Mahendra Chinthala, [b] Natarajan Rajamohan[*c] and Bo Weng [*de]

The growing global demand for sustainable energy and environmental remediation has accelerated interest in efficient, metal-free photocatalysts. Cellulose, known for its abundance, biodegradability, tunable chemistry, high surface area, and mechanical robustness, has emerged as an ideal support material for photocatalytic systems. This review presents a comprehensive evaluation of cellulose-supported photocatalysts, detailing their structural forms, physicochemical properties, preparation strategies, and design principles. The classification of cellulose-based composites and structured architectures into hydrogels, aerogels, membranes, and sponges highlights the versatility of cellulose in enhancing catalyst dispersion, charge separation, visible-light activity, and reusability. Their applications include hydrogen and hydrogen peroxide generation, nitrogen fixation, CO_2 reduction and wastewater treatment and disinfection. Strengths, weaknesses, opportunities, and threats (SWOT) analysis provides insights into their strengths, limitations, and research gaps, emphasizing challenges in large-scale fabrication, stability, and commercial viability. Furthermore, this review highlights the significance of environmental and economic analyses to guide their sustainable scale-up and market adoption. Future directions should focus on heterostructure engineering, defect modulation, green synthesis, AI-guided optimization, and integration into real-world systems. By bridging materials science, catalysis, and environmental engineering, cellulose-supported photocatalysts hold significant potential for scalable, eco-friendly, and multifunctional solutions aligned with the fundamentals of circular economy, green chemistry, and the United Nations Sustainable Development Goals.

1. Introduction

The accelerating convergence of the global energy crisis and environmental degradation driven by unchecked industrialization, urban sprawl, and fossil fuel dependence has intensified the demand for transformative solutions that can safeguard both ecological integrity and human well-being.[1,2] Conventional systems for energy production and wastewater treatment are no longer sufficient to meet the rising expectations for sustainability, particularly under the framework of the United Nations

Sustainable Development Goals.[3] The emergence of persistent organic pollutants and antibiotic-resistant microbes and the limited scalability of traditional treatment technologies further exacerbate this shortfall.[4,5] Simultaneously, the intermittent nature of renewable energy sources underscores the need for integrated systems that offer both environmental remediation and energy valorization.[6] In particular, multifunctional, low-cost, sustainable, and environmentally benign technologies are required that can integrate clean energy generation with efficient pollutant mitigation.[7]

In this context, photocatalysis has emerged as an efficient method for the mineralization of noxious contaminants and in energy-related applications such as hydrogen generation and nitrogen fixation.[8–11] Different photocatalysts, such as TiO_2,[8] ZnO,[12] ZnS,[13] CdS,[14] $g-C_3N_4$,[15] In_2S_3 [16] and WO_3,[17] are commonly employed in energy applications and environmental remediation due to their high redox potential and stability, but these catalysts face several practical challenges that limit their real-world applications.[18] Their key issues include limited absorption in the visible light spectrum, as seen in TiO_2 and ZnO, minimal adsorption capacity for recalcitrant compounds,

aInnovative Catalysis and Sustainability Group, Department of Chemical Engineering, Saintgits College of Engineering (Autonomous), Kottayam, Kerala 686532, India. E-mail: akash.balakrishnan@saintgits.org

bProcess Intensification Laboratory, Department of Chemical Engineering, National Institute of Technology Rourkela, Odisha 769 008, India

cChemical Engineering Section, Faculty of Engineering, Sohar University, Sohar, Oman. E-mail: rnatarajan@su.edu.om

dState Key Laboratory of Advanced Environmental Technology, Institute of Urban Environment, Chinese Academy of Sciences, Xiamen 361021, P.R. China. E-mail: bweng@iue.ac.cn

eUniversity of Chinese Academy of Sciences, Beijing 100049, China

This journal is © The Royal Society of Chemistry 2026

J. Mater. Chem. A, 2026, 14, 5473–5519 | 5473

recombination of charge carriers, poor catalyst dispersion in aqueous media, tedious and difficult catalyst recovery, and poor reusability.[19–21] Moreover, specific catalysts like CdS raise toxicity concerns, which further restrict their environmental applicability, mandating the need for environmentally benign and efficient photocatalysts.[22] Doping,[23] co-doping,[24] heterojunction construction,[25] defect engineering,[26] and morphology control[27] have been proposed to overcome the limitations of photocatalysts. These approaches have proven effective in enhancing visible light harvesting and charge separation and efficiency.[28] However, incorporating suitable support materials can further enhance the catalyst stability, prevent its aggregation, improve pollutant adsorption, and facilitate its recovery and reuse, making the system more practical and efficient for real-world applications.[29,30]

The concept of using support materials plays a crucial role in advancing photocatalytic systems, particularly by enhancing the stability, reusability, and recovery of catalysts in aqueous media.[31] Conventional supports such as silica, clay, perlite, and synthetic polymers have been utilized to mitigate challenges like catalyst aggregation and poor separation.[18] Notably, biopolymers have gained attention as eco-friendly alternatives, with cellulose standing out due to its abundance, renewability, and unique physicochemical features.[32] Its high surface area, excellent hydrophilicity, tunable porosity, mechanical flexibility, and chemical modifiability make it highly effective in anchoring photocatalysts, improving pollutant adsorption, light harvesting, and reusability.[33] Additionally, cellulose is environmentally benign, cost-effective, and compatible with green fabrication methods, making it highly attractive for scalable energy and environmental technologies.[34] These unique attributes of cellulose-supported photocatalysts make them suitable for application in energy generation and ecological remediation.[30,35,36] The publication trend from 2015 to 2025 shows a steady rise in research output, peaking in 2023, before gradually declining in the subsequent years. This pattern highlights a period of accelerated research activity and collaboration during 2020–2023, likely influenced by increased focus on emerging scientific challenges. The recent decline suggests a stabilization phase, indicating scope for renewed strategies to sustain consistent contributions (Fig. 1). However, a comprehensive review on cellulose-supported photocatalysts specifically tailored for energy and environmental applications is still lacking.

This review paper emphasizes the recent advancements in cellulose-supported photocatalyst for energy and environmental applications (Fig. 2). It begins with detailed insights into photocatalytic mechanisms, along with a critical evaluation of the common challenges and limitations in existing photocatalytic systems. A dedicated section focuses on cellulose, describing its types, structural features, and physicochemical properties relevant to the formation of composites. This review also discusses why cellulose is an ideal support material, highlighting its natural abundance, renewability, high surface area, mechanical strength, chemical modifiability, and biocompatibility, which together enhance the dispersion, stability, and reusability of photocatalysts. This is followed by an in-depth analysis of cellulose-supported photocatalysts, including key design considerations and preparation methods. Various categories of cellulose-supported catalysts are examined, such as metal oxide based, metal sulfide based, metal organic frameworks (MOFs), hydrogels, aerogels, and membranes. This review explores their wide-ranging applications, including photocatalytic hydrogen peroxide generation, hydrogen production, nitrogen fixation, carbon dioxide reduction, wastewater treatment, and disinfection. The final section outlines the advantages, limitations, and prospects of these systems, offering insights into their potential for scalable, multifunctional photocatalytic technologies.

2. Photocatalysis

Photocatalysis is emerging as a cost-effective and environmentally sustainable strategy for both energy and environmental applications. However, for its broader adoption, photocatalysts must be optimized to achieve high quantum yields, broad-spectrum light absorption, and enhanced reaction selectivity.[37] Advancing photocatalytic technology requires several aspects to be addressed, such as band gap tuning, catalyst immobilization, morphology control, reactor efficiency, and effective charge separation.[4,38] A key determinant of the performance of photocatalysts is its band gap, which describes the minimum photon energy needed to initiate the photocatalytic process. The photocatalytic process begins with photon absorption, exciting electrons from the valence band to the conduction band, forming electron–hole pairs.[39] These charge carriers generate reactive oxygen species like superoxide anion ($\cdot O_2^-$), hydroxyl radical (HO$\cdot$), and hydroperoxyl radicals ($HO_2^{\cdot}/HO_2^-$).[40,41] These ROS oxidize pollutants, and mineralize them into CO_2 and H_2O on the photocatalytic surfaces, further improving the electron transfer efficiency, with oxygen acting as a key electron acceptor.[42] In oxygen-rich environments, the
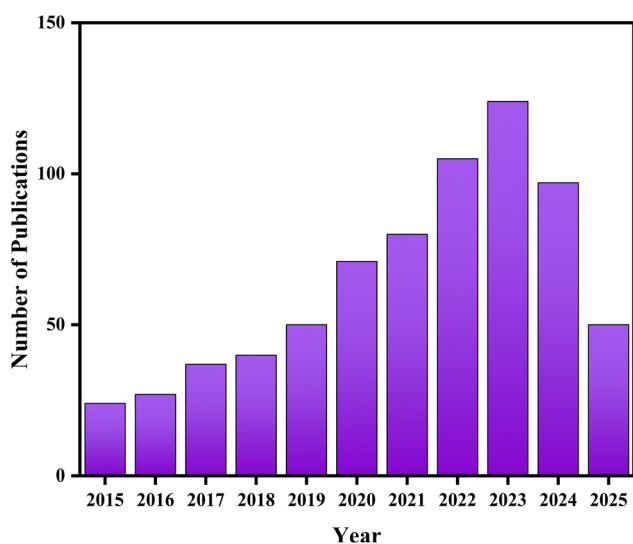

Fig. 1 Annual publication trends on cellulose-supported photocatalysts from 2015 to 2025 (source: Web of Science).

5474 | *J. Mater. Chem. A*, 2026, **14**, 5473–5519

This journal is © The Royal Society of Chemistry 2026

PREHISTORY TIMELINE

Cellulose-supported photocatalysts mark a sustainable shift in environmental remediation. Their evolution from raw cellulose composites to structured hydrogels and aerogels enables enhanced charge transfer, pollutant degradation, and visible light response. The integration of biopolymers with semiconductors continues to revolutionize green photocatalytic applications.

2002 Firstly Cellulose-TiO₂ based composites were prepared for environmental applications

2005 Cellulose-based membranes was firstly developed for wastewater remediation

2018 Utilization of cellulose-catalysts as activator for peroxymonosulfate systems

2017 Cellulose-based photocatalytic heterojunctions were prepared and firstly used for hydrogen production

2015 Cellulose-based photocatalysts were utilized for photo-Fenton systems

2014 Cellulose-based photocatalytic hydrogels and aerogels were developed

2019 Carbon dioxide reduction using hybrid cellulose-supported photocatalysts

2023 Cellulose impregnated photocatalysts were used for H₂O₂ production studies

2024 CMC/photocatalytic hydrogels were fabricated for nitrogen fixation

2025 It was employed in development of hybrid oxidation systems such as PSF-PMS, photo-self-Fenton
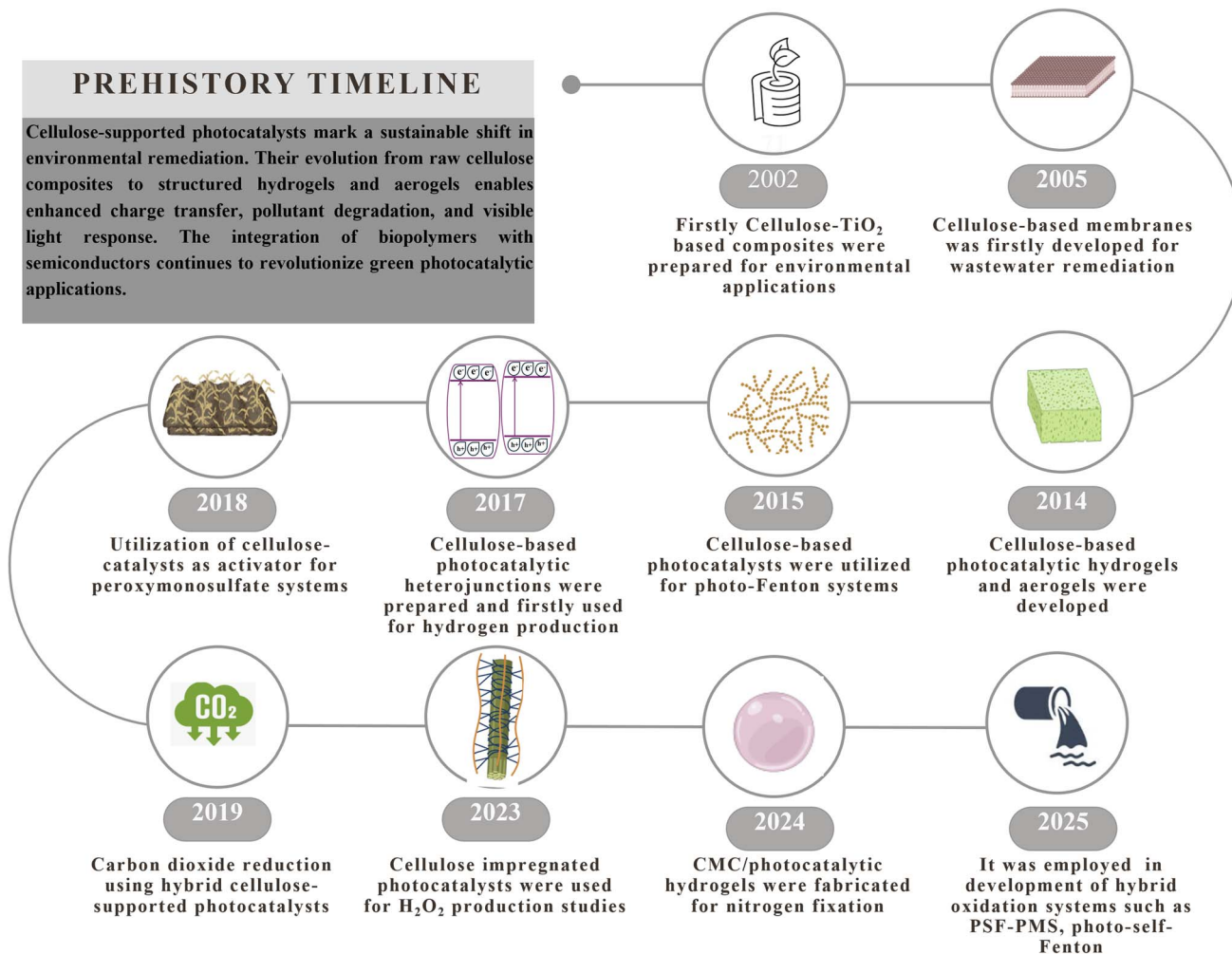
Fig. 2 Milestones in the evolution of cellulose-supported photocatalysts from 2002 to 2025. The timeline highlights key innovations ranging from early TiO₂–cellulose composite and wastewater membranes to modern hybrid systems enabling energy generation and multi-pollutant degradation. This chronological progression reflects the growing sophistication and multifunctionality of cellulose-integrated photocatalytic systems.

photocatalytic process proceeds efficiently, transforming organic pollutants into intermediate hydroxylated compounds, and eventually attaining complete mineralization into carbon dioxide and water.[31,43] Simultaneously, photogenerated holes in the valence band react with donor species, further promoting the breakdown of organic matter. Pre-adsorption of oxygen and water onto the photocatalytic surface enhances electron transfer, with oxygen serving as the primary electron acceptor in environmental remediation contexts. Thus, the interaction of ROS, free electrons, and holes with various pollutants, such as organic, inorganic, bacteria, and viruses, facilitates their complete decomposition into non-toxic by-products.[44,45] Alternatively, ROS species such as superoxide radicals undergo electron-assisted reduction reaction to yield sustainable fuels such as hydrogen, ammonia, and hydrogen peroxide, as discussed in Section 6.[46–48]

Bandgap is a fundamental property that governs the electronic behavior and light absorption capacity of photocatalysts. Practical band gap engineering is essential to maximize solar light harvesting and enhance the photocatalytic activity of materials.[37] One widely adopted approach involves modifying photocatalytic structures by incorporating suitable dopants. However, although doping can narrow the band gap and enhance visible light absorption, it may also introduce recombination centers, which hinder charge carrier mobility, thereby reducing the photocatalytic efficiency.[49,50] Thus to address this, alternative strategies have been explored, such as doping, material coupling, heterojunction, and dye sensitization (Table 1).[20] Photocatalysis is a multifaceted process involving simultaneous optical, electrical, and chemical interactions. Although photocatalysts are central to these interactions, the efficacy of the overall process is influenced by the compatibility and stability of the support materials used. The synergy between the photocatalyst and its support is critical for maintaining optimal light utilization, separation of charge carriers, and surface reactions throughout the process.[31,51]

Following the dissociation of excitons, the generated free electrons and holes drive redox reactions, which is an essential

This journal is © The Royal Society of Chemistry 2026

J. Mater. Chem. A, 2026, 14, 5473–5519 | 5475

Table 1 Comparison of different design engineering strategies adopted in photocatalysis[3,18,22,37,52,53]

Method	Explanation	Advantages	Disadvantages
Single-atom anchoring	Anchoring isolated single metal atoms (cobalt, nickel, *etc.*) onto the surface of a 2D photocatalyst to serve as active sites	(1) Improves charge separation (2) Tunable catalytic sites (3) Maximizes atom utilization	(1) Complex synthesis methods (2) Stability issues (3) Single atoms may agglomerate under reaction conditions
Defect engineering	Introduction of vacancies, dislocations, or other structural defects to modify electronic and catalytic properties	(1) Enhances active site density (2) Tunes the band gap (3) Improves light absorption	Defects may act as recombination centers, and controlling their concentration is challenging
Elemental doping	The incorporation of metal or non-metals into the lattice alters the electronic structure and optical properties	(1) Expands light absorption range (2) Improves conductivity (3) Tunes band gap	Leaching of dopants and probable risk of forming unwanted recombination centers
Coordination activation	Modifying the coordination environment around active metal sites to optimize catalytic performance	Ensures specific reaction pathways and improves the binding of target molecules	Requires precise control over coordination chemistry
Organic ligand modification	Attaching organic ligands or molecules to modify surface properties, band structure, and dispersion	(1) Improves solubility and dispersibility (2) Selective adsorption of reactants	The possibility of photodegradation of ligands and steric hindrance may influence the active sites
Heterojunction	Combining two or more semiconductors to form an interface that facilitates charge transfer	Promotes efficient charge separation and reduces the recombination ratio	Complexity in catalyst preparation and potential difference lattice matching

step in photocatalysis. The efficacy of dissociation is dependent on factors such as exciton binding energy, carrier mobility, and charge lifetime. However, structural defects in photocatalysts can trap charge carriers, leading to recombination losses.[31] Thus, to overcome this, heterojunction structures have been extensively explored to promote charge separation and minimize recombination.[54] A heterojunction photocatalyst is formed at the interface between two semiconductors or a semiconductor and a metal with mismatched band structures and electronic properties.[55] The proper design facilitates directional charge transfer, thereby enhancing its photocatalytic performance by suppressing electron–hole recombination.[56] The commonly employed heterojunction types include type-I, –II, and –III junctions, p–n junction, Schottky junction, and Z-scheme and S-scheme junctions.[52] More details about different design strategies are described in Table 1.

However, despite these advancements, photocatalysts still face several drawbacks that limit their real-world application. These issues include poor long-term stability, low efficiency under visible light, susceptibility to photocorrosion, and difficulty in recovering the catalyst after reuse, especially in liquid-phase systems.[8,57] In the case of environmental applications, the aggregation of photocatalyst nanoparticles leads to the loss of active surface area and hinders pollutant contact, while in solar fuel production, the rapid recombination of photoinduced charge carriers limits product yields.[20,58] In disinfection, reduced surface interactions with pathogens due to structural instability or fouling affect the efficacy. These challenges underscore the importance of incorporating suitable support materials that can address multiple functional needs.[59] An ideal support enhances the dispersion of photocatalyst particles,

maintains structural integrity under operational conditions, improves the mass transfer of reactants and products, and enables ease in recovery and reusability.[60] Moreover, it can actively assist in interfacial charge separation, prolong the carrier lifetimes and facilitate reaction pathways *via* synergistic interactions.[61]

An ideal support material for environmental applications must meet several key criteria to ensure effective and stable photocatalysis. It should be chemically stable, non-toxic, and have low water solubility to prevent degradation and secondary contamination.[62] Hydrophobicity is essential for attracting organic pollutants, while a dielectric constant in the range of 2.2 to 3.5 helps minimize charge loss. Strong adhesion with the photocatalyst prevents particle detachment, and transparency ensures maximum light utilization.[31] Additionally, flexibility allows application on curved surfaces, and a high surface area enhances interactions with pollutants. These requirements can be grouped into two categories: (a) practical aspects such as chemical stability, reusability, and cost-effectiveness and (b) features that enhance photocatalytic performance, including efficient light harvesting, reduced charge recombination, and improved contact with contaminants. The commonly employed photocatalytic supports are silica, glass, alumina, carbon, zeolite, and biopolymers.[5] Based on the comparative analysis of different supports (Table 2), biopolymers are ideal support materials for photocatalytic applications due to their abundance, renewability, and biodegradability, making them both sustainable and safe.[63] They offer excellent chemical stability and low water solubility, ensuring durability without leaching into treated water. Their high surface area and porous structure enhance pollutant adsorption and photocatalytic activity, while

5476 | *J. Mater. Chem. A*, 2026, **14**, 5473–5519

This journal is © The Royal Society of Chemistry 2026

Table 2 Comparative evaluation of different photocatalytic supports such as organic, inorganic, polymeric, biopolymeric, and hybrid supports[a]

Parameters	Supports				
	Inorganic materials	Organic materials	Polymers	Biopolymers	Hybrid supports
Examples	TiO_2, SiO_2	Biochar, graphene oxide	Polyvinyl alcohol, polyacrylonitrile	Cellulose, chitosan, and alginate	MOFs, COFs, and carbon nitrides
Surface area	average	good	average	good	good
Porosity	poor	average	average	good	good
Light permeability	poor	poor	average	good	poor
Biodegradability	poor	poor	poor	good	poor
Hydrophilicity	good	good	good	good	good
Adsorption potential	average	good	average	good	good
Chemical versatility	poor	good	good	good	good
Charge transfer	good	good	good	average	good
Stability	good	good	average	good	good
Sustainability	poor	poor	poor	good	poor
Cost efficiency	good	good	average	good	poor
Green compliance	poor	poor	poor	good	poor
Thermal stability	good	average	average	good	good
Reusability	good	average	average	good	good
ROS support capability	good	average	average	good	good
Mechanical strength	average	good	average	good	average
Pollutant selectivity	poor	good	average	good	good
Overall rating	average	average	average	good	good

[a] Where (hatched) is good, (open) is average and (dark hatched) is poor.

3. Cellulose

their modifiable surface allows strong adhesion with photocatalysts and tunable hydrophobicity.[64,65] Biopolymers can also facilitate electron transfer due to the presence of OH groups that can interact with photocatalysts, aiding in charge separation and reducing electron–hole recombination.[66] Biopolymers are flexible for use in various reactor configurations, such as thin films, hydrogels, aerogels, composites, and membranes, fulfilling both practical and photocatalytic efficiency requirements.[61,67] Among the different biopolymers, cellulose is often explored as a versatile biopolymer for energy and environmental applications.

Cellulose is the most abundant biopolymer in the world.[5] It is made up of D-glucose monomers $(C_6H_{10}O_5)_n$, which are connected through $\beta(1 \rightarrow 4)$ glycosidic bonds. The value of n is attributed to the degree of polymerization, which ranges from 10 000 to 15 000, based on the cellulose source.[68] Its structure is stabilized by extensive intra- and inter-molecular hydrogen bonding, yielding a semi-crystalline, mechanically robust, flexible, and biodegradable material sustainable for sustainable applications.[5,32] The dense hydrogen-bonding network in

This journal is © The Royal Society of Chemistry 2026

J. Mater. Chem. A, 2026, **14**, 5473–5519 | **5477**

cellulose imparts excellent barrier properties, enabling its use in packaging, biomedical systems, and environmental remediation.[33] Cellulose can be engineered into various structural forms such as thin films,[69] membranes,[70] hydrogels,[36] aerogels,[71] fibers,[72] nanoparticles,[73] and even 3D-printed architectures,[74] making it a versatile platform for integrating photocatalysts in environmental processes.

Cellulose exists in multiple polymorphic forms (Iα, Iβ, II, III, IV, V, and VI), each with distinct stability and structural characteristics.[33,75] The metastable Iα polymorph, predominantly found in algae and bacterial cellulose, can partially transform into the more stable Iβ form through hydrothermal annealing at 260 °C under basic conditions, although the conversion is often incomplete. Cellulose Iβ, the dominant form in higher plants, is the most abundant natural polymorph and is widely studied for industrial applications. Cellulose II, the thermodynamically stable polymorph, is produced via regeneration or mercerization using aqueous NaOH, enabling improved structural integrity, stability, and processability for films, fibers, and related products.[76] Cellulose III is generated from cellulose I or II through ammonia-based chemical processes, introducing substantial changes in its physical and chemical properties.[77] Subsequent thermal treatment converts cellulose III into cellulose IV, further enhancing its stability and expanding its material utility.[78] These controlled polymorphic transitions allow fine-tuning of the characteristics of cellulose for targeted applications. Cellulose is sourced from a wide range of renewable feedstocks, including agricultural residues, industrial waste streams, and lignocellulosic biomass such as cotton linters, wheat straw, sugar beet pulp, bagasse, municipal solid waste, corncob, and fruit/vegetable peels.[79,80] Marine tunicates (Ascidiacea; >2300 species) also provide highly crystalline cellulose. Algae and bacteria serve as important biological sources, offering unique structural variants and high-purity cellulose.[81]

Cellulose exists in diverse structural forms, each offering specific properties and application potential. These include wood fibres, microcrystalline cellulose (MCC), micro-fibrillated cellulose (MFC), nanocellulose, cellulose nanocrystals (CNCs), algal cellulose, bacterial cellulose, and plant fibres.[82] Bacterial cellulose, primarily produced by *Komagataeibacter xylinus*, exhibits exceptional purity, high crystallinity, and phenomenal mechanical strength, making it highly attractive for biomedical, food, and industrial uses.[83] Algal cellulose from red and green algae provides a renewable and biocompatible alternative source, supporting the development of sustainable materials.[83] Wood and plant fibres, typically derived from dissolved pulp, possess a hierarchical micro-scale structure (micron-diameter, millimeter-length) and comparatively lower crystallinity, making them suitable for paper, textile, and composite applications.[84] Table 3 presents a summary of the structural forms of cellulosic and nano-cellulosic catalysts with key properties and applications.

4. Cellulose-supported photocatalysts

The integration of cellulose with photocatalysts presents a promising strategy to address the limitations of conventional

Table 3 Summary of the structural forms of cellulosic and nano-cellulosic catalysts with preparation strategies, key properties, and applications[85–87]

Category	Types	Preparation strategy	Dimensions	Properties	Major applications
Bulk forms	Wood/plant fibres	Mechanical pulping, chemical pulping, bleaching	Diameter μm; length: mm	Hierarchical fibres, moderate crystallinity mechanically robust	Textile, paper, reinforcement
	Microcrystalline cellulose (MCC)	Controlled acid hydrolysis of plant fibres	10–50 μm	High crystallinity, high purity, excellent binding/compressibility	Pharmaceuticals, food, additives
	Algal cellulose	Extraction from red/green algae using alkaline treatment and purification	Varies	Renewable, biocompatible, moderate crystallinity	Biopolymers, biodegradable materials
	Bacterial cellulose (BC)	Microbial fermentation (*e.g.*, *Komagataeibacter xylinus*) under static/agitated culture	Nanoscale fibrillar network	High crystallinity; exceptional purity; high tensile strength; high water retention	Biomedical implants, wound dressings, membranes
Nano-cellulosic materials	Cellulose nanocrystals (CNCs)	Acid hydrolysis (commonly H_2SO_4 or HCl) followed by neutralisation & ultrasonication	3–20 nm (dia.); 50–500 nm (length)	Highly crystalline, stiff, rod-like; strong optical and rheological behaviour	Catalysis, sensing, nanocomposites, packaging
	Micro-fibrillated cellulose (MFC)	High-shear mechanical fibrillation, refining, homogenisation; sometimes enzymatic pretreatment	10–100 nm (dia.); μm-length	Mixed crystalline–amorphous; flexible; gel-forming; high water-holding	Coatings, emulsifiers, packaging, biomedical scaffolds
	Cellulose nanofibrils (CNFs)	Mechanical disintegration (homogenisation, microfluidisation); TEMPO-mediated oxidation optional	5–100 nm (dia.); μm-length	High aspect ratio; strong; flexible; high water retention; shear-thinning	Lightweight composites, barrier films, biomedical materials, paper reinforcement

5478 | *J. Mater. Chem. A*, 2026, **14**, 5473–5519

This journal is © The Royal Society of Chemistry 2026

photocatalysts, like low stability, difficult recovery, and photocatalyst leaching.[36] Numerous studies have highlighted the functionalization of cellulose and its derivatives with various photocatalysts such as MOFs, COFs, carbon nitride, metal oxides, and metal sulfides, resulting in the formation of hybrid catalysts with phenomenal catalytic activity. In most cases, the hybrid systems are stabilized through hydrogen bonding, electrostatic interaction, or covalent bonding between the functional groups on cellulose and the photocatalyst surface.[88] This functional integration results in enhanced dispersion of the catalyst, improved charge separation, and an enhanced surface area, leading to greater catalytic activity.[66] Along with this, cellulose also imparts flexibility, biodegradability, and mechanical reinforcement to hybrid systems. The incorporation of cellulose not only facilitates the recovery and reuse of the catalyst but also contributes to the environmental compatibility of the overall system.[89,90]

4.1 Design criterion for cellulose-supported catalysts

The rational design of cellulose-supported photocatalysts requires integrating structural, interfacial, and functional considerations to achieve high activity and operational stability. A primary requirement is establishing strong interfacial interactions between cellulose and the photocatalyst, which facilitates rapid charge transfer and suppresses electron–hole recombination. The inherent OH-rich chemistry of cellulose enables effective anchoring of semiconductor particles and allows targeted surface modification to enhance their dispersion, selectivity, and stability.[91] Cellulose derivatives (like nanofibers) offer high surface area and hierarchical porosity, increasing the density of accessible active sites and promoting efficient mass transport. The coupling these supports with visible light-responsive semiconductors such as carbon nitride, ZnO, and bismuth-based materials, and introducing heterojunctions or defect states (*e.g.*, oxygen vacancies), further improves their light harvesting and charge-separation efficiency.[66,92] Chemical crosslinking or polymer–inorganic hybridization enhances the mechanical robustness, suppresses the leaching, and enables the repeated reuse of photocatalysts, supporting their scalability for continuous applications. Environmental compatibility must also be considered; renewable cellulose and non-toxic semiconductor phases minimize secondary pollution and align with green chemistry principles. The critical design considerations are detailed as follows (Fig. 3):[3,93–96]

● Strong interfacial interactions: efficient charge transfer between the cellulose support and photocatalyst is fundamental to suppress electron–hole recombination, which directly affects the photocatalytic efficacy. This is attained through the formation of robust physical or chemical bonds at the interface, which can include hydrogen bonding, covalent bonding, or coordination interactions based on the functional groups present.
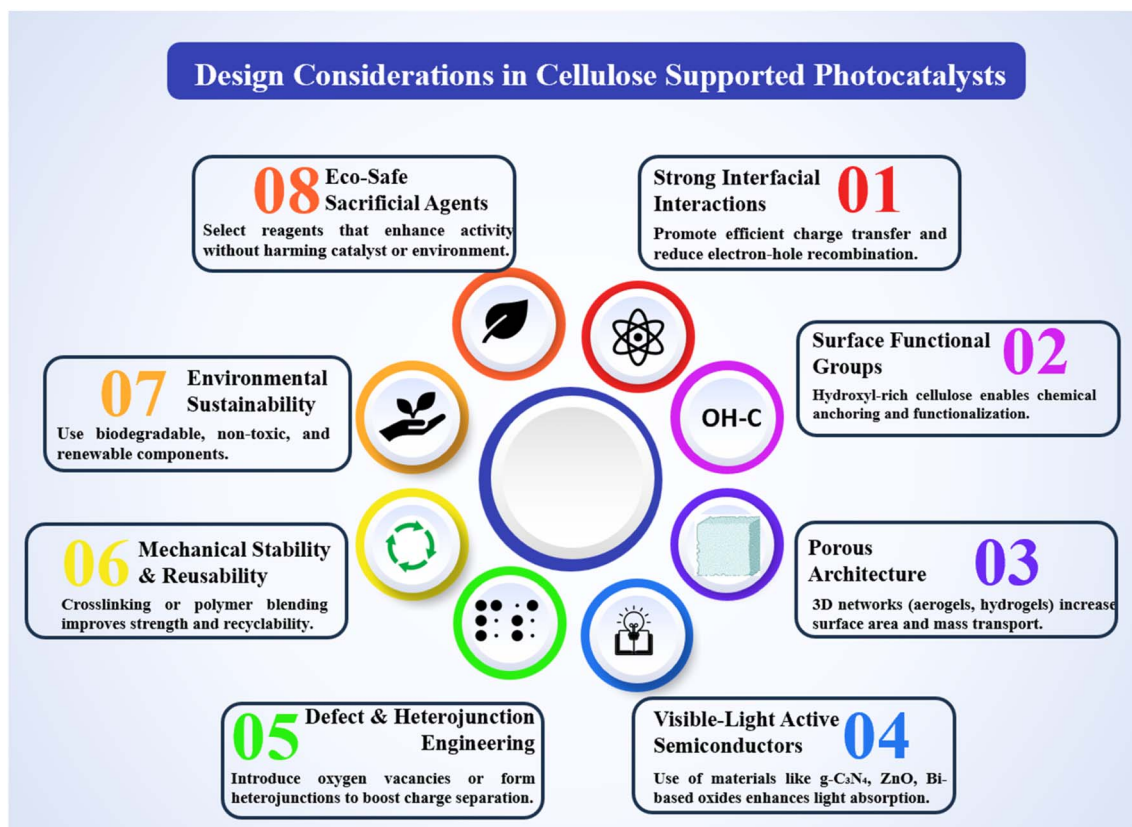

Design Considerations in Cellulose Supported Photocatalysts

08 Eco-Safe Sacrificial Agents Select reagents that enhance activity without harming catalyst or environment.

01 Strong Interfacial Interactions Promote efficient charge transfer and reduce electron-hole recombination.

07 Environmental Sustainability Use biodegradable, non-toxic, and renewable components.

02 Surface Functional Groups Hydroxyl-rich cellulose enables chemical anchoring and functionalization.

06 Mechanical Stability & Reusability Crosslinking or polymer blending improves strength and recyclability.

03 Porous Architecture 3D networks (aerogels, hydrogels) increase surface area and mass transport.

05 Defect & Heterojunction Engineering Introduce oxygen vacancies or form heterojunctions to boost charge separation.

04 Visible-Light Active Semiconductors Use of materials like g-C₃N₄, ZnO, Bi-based oxides enhances light absorption.

Fig. 3 Design considerations during the fabrication of cellulose-supported photocatalysts.

This journal is © The Royal Society of Chemistry 2026

J. Mater. Chem. A, 2026, **14**, 5473–5519 | **5479**

● Chemical functionality of cellulose: the surface of cellulose is rich in OH groups, which provide versatile sites for chemical modification and anchoring of photocatalytic nanoparticles. Functionalization strategies, such as carboxylation and amination, can tailor their surface charge, hydrophilicity, and affinity towards specific photocatalysts, improving their dispersion and preventing agglomeration, thus enhancing their catalytic activity and selectivity.

● Porous architecture and surface area: cellulose derivatives such as nanofibers, aerogels, and hydrogels offer a 3D porous network with greater surface area. This structure facilitates numerous catalytic sites and ensures the efficient diffusion of reactants and products, thereby reducing mass transport limitations and increases the photocatalytic reaction rate.[81]

● Mechanical robustness and reusability: chemical cross-linking or hybridization of cellulose with other polymers or inorganic materials significantly enhances its mechanical strength and minimizes the leaching and enables the easy recovery and reuse of the photocatalyst. These modifications extend the operational lifespan of the catalyst and lower the costs related to its frequent replacement or disposal.

● Environmental compatibility and sustainability: to prevent secondary pollution, both cellulose and the photocatalytic components must be environmentally benign, biodegradable, and non-toxic. Utilizing renewable cellulose as a support material aligns with the principles of green chemistry, while minimizing the use of hazardous substances in the photocatalyst formulation promotes safer and more sustainable applications.

● Selection of sacrificial agents: when sacrificial reagents are employed to scavenge photogenerated charge carriers and boost the photocatalytic efficiency, it is essential to evaluate their influence on the overall stability and environmental safety of the system. An ideal sacrificial agent should effectively enhance photocatalytic activity without accelerating catalyst degradation or producing hazardous by-products.

4.2 Mechanistic influence of cellulose characteristics on photocatalytic performance

The photocatalytic properties of cellulose-based photocatalysts are influenced not merely by the presence of cellulose as a scaffold, but by the synergistic interplay among their intrinsic morphological features, degree of crystallinity, surface functional chemistry, hierarchical porosity, and the nature of their interfacial electronic coupling with embedded semiconductor. Despite being intrinsically photocatalytically inert, cellulose exerts stronger mechanistic control over composite photocatalysts through its hierarchical architecture from nanofibrils to aerogels. These structural features regulate light management, charge separation, ROS generation and pollutant–catalyst interfacial reaction. Also, its crystallinity, porosity, and surface chemistry govern catalyst dispersion, interfacial electron–hole transfer, and suppression of charge recombination.

4.2.1 Surface chemistry and functional groups. Cellulose exhibits a highly reactive surface enriched with primary, secondary, and tertiary hydroxyl groups, which collectively

explains its interfacial behavior with photocatalysts.[97] These hydroxyl functionalities behave as versatile coordination sites capable of forming hydrogen bonds, dipole–dipole interactions, and metal–ligand complexes with metal oxides, metal ions and semiconductor precursors.[98] Because the electron-rich oxygen atoms of hydroxyl groups present strong affinity towards electropositive transition-metal centers, cellulose provides a chemically active platform that directs the nucleation, anchoring, and stabilization of photocatalysts. This interfacial affinity not only prevents the agglomeration of photocatalysts but also ensures the high-density, homogeneous distribution of photocatalyst domains, which is essential for optimizing light absorption and creating efficient charge-transfer channels in composite systems.

Apart from physical dispersion, the surface chemistry of cellulose directly modulates the photocatalytic charge-transfer dynamics.[99] Its hydrogen-bond network facilitates proton-coupled electron-transfer, enabling cellulose to transiently shuttle electrons or protons at the semiconductor interface, which lowers the interfacial charge transfer resistance.[100] The local polarity variations around the hydroxyl groups influence the band alignment of supported photocatalysts, which is beneficial to stabilize photoexcited carriers and reduce the recombination ratio.[101] Introducing additional functional groups such as carboxyl, aldehyde, sulfate, and grafted polymeric moieties further enhances metal-ion chelation, and increases the nucleation site density, leading to better-defined semiconductor domains and stronger electronic coupling. These chemical modifications can tune the surface charge, acidity, and redox potential, ultimately influencing the radical generation pathways and reaction selectivity during photocatalysis.[102]

The hierarchical distribution of functional groups in nanocellulose also amplifies these effects. CNC offers high crystallinity and densely packed surface hydroxyls, which facilitate strong electronic interactions with semiconductor clusters, whereas CNFs and bacterial cellulose provide more flexible networks capable of dynamically interacting with intermediates and ensuring mass transport.[34–91] The presence of amorphous regions may possibly introduce defects and reactive sites, which can promote localized charge accumulation or enhanced adsorption of pollutants prior to oxidation. In aqueous-phase photocatalysis, the hydrophilic nature of cellulose, arising directly from its surface chemistry, promotes water uptake, swelling, and formation of hydration shells around the catalyst nanoparticles. These microenvironments enhance the diffusion of ROS, promote pollutant catalyst contact, and maintain a continuous supply of reactants, ultimately improving the photocatalytic quantum efficiency.[103,104]

Alternatively, chemical functionalization further extends the mechanistic role of cellulose. Oxidized cellulose introduces aldehydes and carboxylates, which also coordinate with metal ions, improving the robustness of *in situ* precipitation routes and yielding a tightly bonded semiconductor–cellulose interface with superior charge-transfer characteristics.[91] Esterification, silylation, and graft polymerization introduce tailored hydrophobic/hydrophilic balances, enabling control over

5480 | *J. Mater. Chem. A*, 2026, **14**, 5473–5519

This journal is © The Royal Society of Chemistry 2026

interfacial wettability, pollutant adsorption kinetics, and light-scattering properties. These chemical strategies can shift the band gap energy, modulate the electron density around the catalytic sites, and create a synergistic interfacial electric field, which influence the photocatalytic rates.[34–105] Overall, the surface functional groups in cellulose are not passive stabilizers but active determinants of photocatalytic performance. By mediating both chemical and electronic interactions, cellulose transforms photocatalysts from simple nanoparticle ensembles into highly integrated, interfacial engineered hybrid systems with greater catalytic performance.

4.2.2 Hierarchical morphology. Cellulose exists in diverse nanoscale architectures, which imparts unique structural features. For example, cellulose nanocrystals (CNCs) are rigid rod-like crystallites with extremely high crystallinity and specific surface area. Cellulose nanofibers (CNF) are long flexible fibrils with relatively high aspect ratios, which entangle into continuous 3-D webs. Bacterial cellulose (BC) forms ultra-fine, highly pure nanofibrillar mats, which naturally assemble into porous pellicles with nano or microscale voids.[87] For example, Habibi *et al.* (2020) reported the use of CNFs as templates to coat TiO_2 *via* three routes, allowing the influence of CNF morphology and processing method on the final TiO_2 architecture to be evaluated. The CNF hydrogel (Fig. 4a) exhibited a highly entangled 3D network of long, flexible nanofibers (10–50 nm diameter), which directly entered the sol–gel process. However, excessive water triggered the uncontrolled hydrolysis of TTIP, causing the TiO_2 nanoparticles to aggregate along the fibers and form fused TiO_2–CNF bundles (Fig. 4b). Freeze-drying of the CNF hydrogel collapsed the native fibrous network due to the growth of ice-crystals, yielding sheet-like structures in the aerogel (Fig. 4c). Consequently, the aerogel–TiO_2 composite (Fig. 4d) inherited

this nanosheet morphology, with TiO_2 deposited on compacted cellulose sheets rather than on discrete fibers. In contrast, the CNF alcogel maintained the original fibrillar architecture (Fig. 4e), as solvent exchange with isopropanol prevented network collapse. This intact fibrous template enabled the heterogeneous nucleation of TiO_2 along individual CNFs, producing well-defined TiO_2 nanowhiskers (30–50 nm thick, 250–300 nm long), which closely replicated the morphology of the parent CNF network (Fig. 4f).[106] In another study, cellulose substrates with identical hydroxyl content but different network structures (regenerated cellulose scaffold (RC1W), RC1E, and RC1T) were prepared by regeneration in water, ethanol, and *tert*-butanol baths, respectively. Despite their varying pore sizes (276, 599, and 411 nm, respectively), all the corresponding AZO-loaded composites (AZOC1W/E/T) showed the same flake-like morphology, indicating that the spatial hindrance of cellulose does not control the shape of AZO when the –OH density is constant. To evaluate the role of hydroxyl content, RC1, RC2, and RC3 substrates were produced with increasing cellulose loadings, resulting in progressively higher –OH densities. This directly altered the morphology of AZO, where RC1 yielded flake-like AZO, RC2 generated fragmented flower-like structures, and RC3 produced well-defined flower-like architectures. Increasing the –OH density enhanced the Zn^{2+} coordination and nucleation site availability, driving the assembly of AZO nanosheets into hierarchical flowers. Al doping did not affect the morphology, confirming that the hydroxyl density in cellulose is the dominant regulator of the AZO structure.[107] Yan *et al.* (2023) performed SEM imaging and fractal analysis to track the morphology evolution during CNF etherification. All the ether-ified samples retained their fibrillar structure, but their surfaces became progressively rougher with an increase in DS. This trend
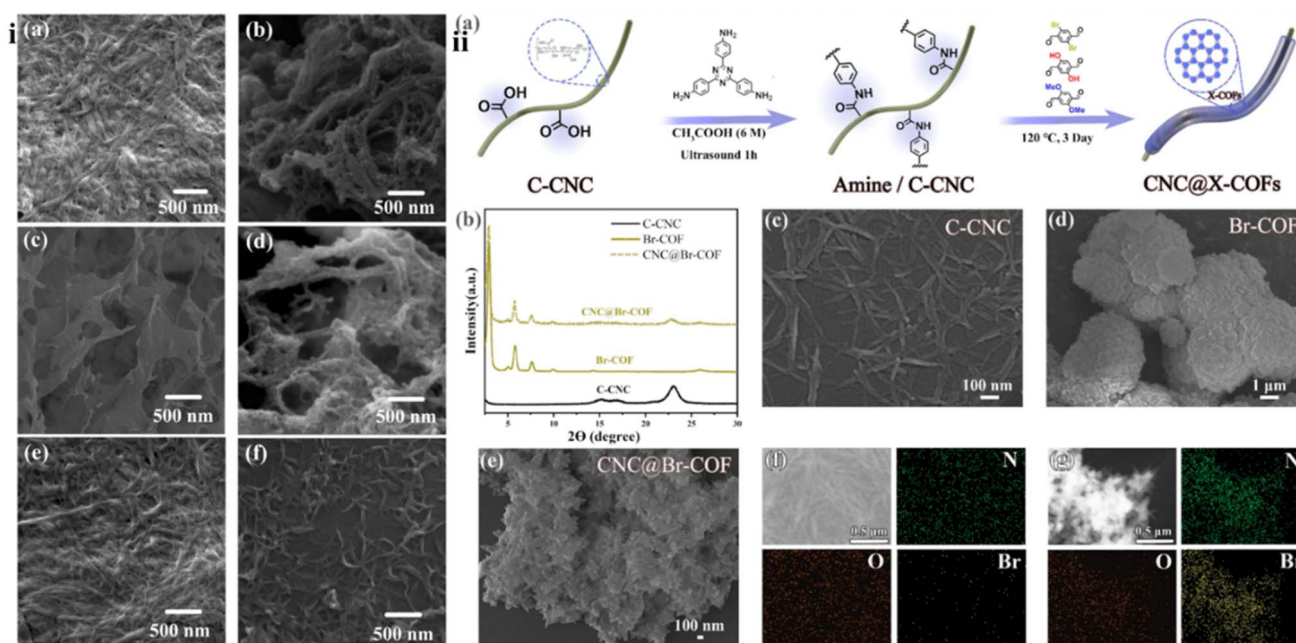

Fig. 4 (i) SEM images of (a) CNF hydrogel, (b) hydrogel–TiO_2, (c) CNF aerogel, (d) aerogel–TiO_2, (e) CNF alcogel, and (f) alcogel–TiO_2. Reprinted with permission from ref. 106, Elsevier (2020). (ii) (a) Schematic of the preparation of CNC@X-COFs, (b) XRD spectra, (c–e) SEM images, and (f–g) EDX spectra of C-CNC and CNC@Br–COFs. Reprinted with permission from ref. 109, Elsevier 2025.

This journal is © The Royal Society of Chemistry 2026

J. Mater. Chem. A, 2026, **14**, 5473–5519 | **5481**

was quantitatively confirmed by the box-counting fractal dimension (D), which increased from 1.37 to 1.47, indicating increasingly complex surface contours ($R^2 > 0.98$ for all fits). To eliminate the differences in diameter and surface roughness introduced by etherification, the samples were ground proportionally to their D values. After grinding, all the CNF and ECNF samples exhibited comparable morphologies, with similar fractal dimensions (1.50–1.53) and high fitting accuracy ($R^2 > 0.98$). ImageJ analysis further verified their uniform size distributions, where all the samples had mean diameters of 23 nm and lengths of ∼1.6–1.8 μm. Overall, CNFs with varying electronegative oxygen contents but nearly identical dimensions and surface morphologies were successfully obtained.[108] Liu *et al.* (2025) interfacial synthesis enabled the uniform growth of X-COFs on C-CNC surfaces, yielding CNC@Br-COF, CNC@OH-COF, and CNC@OMe-COF nanocomposites (Fig. 4iia and b). Their PXRD patterns retained the characteristic reflections of both COFs and C-CNC, confirming the successful formation of the hybrid (Fig. 4iib). SEM images showed well-defined core–shell structures, with the COF shells markedly thicker (Br-COF: 72–107 nm; OH-COF: 64–78 nm; and OMe-COF: 125–165 nm) than the pristine C-CNC (30 nm) (Fig. 4iic–e).[109]

4.2.3 Chirality. Cellulose is intrinsically chiral due to the presence of asymmetric carbon centers in each β-D-glucopyranose unit, which give rise to helical chain conformations and chiral nematic phases in CNC and CNF-based architectures. Hierarchical chirality influences photocatalysis through the chiral surfaces acting as enantioselective templates during semiconductor nucleation. Wang *et al.* (2020) reported that the helical arrangement of –OH groups can influence the crystal orientation of photocatalysts, promote controlled facet exposure and enhance charge separation. The hierarchical chirality in biopolymeric scaffolds can significantly influence the photocatalytic performance by acting as enantioselective templates during semiconductor nucleation. The helical arrangement of surface –OH groups creates an asymmetric chemical environment that biases crystal growth, guiding preferential facet exposure in emerging photocatalyst domains. This chiral templating can modulate the charge distribution and electron–hole separation pathways, thereby enhancing the photocatalytic efficiency.[110] A few researchers emphasized CNC-based structures as photon architectures. The periodic helical order can generate photonic band gaps, slow photon transport, and enable local magnetic fields, and thereby strengthen visible light harvesting in composite photocatalysts. A hybrid material was constructed by orienting anisotropic AgNWs within an optically tunable cholesteric CNC matrix, giving rise to a well-defined interplay between the CNC photonic bandgap and the localized surface plasmon resonances of the nanowires. The resultant photonic–plasmonic coupling mediated by the interaction of PBG-supported electromagnetic modes with AgNW plasmon modes enables precise control over electromagnetic energy transfer and yields selective modulation of plasmonic features within a confined spectral region. Importantly, this coupling persists under dynamic excitation, as evidenced by pronounced transient optical responses in pump–probe measurements.[111] Overall, cellulose chirality acted as an optical and interfacial modulator guiding semiconductor growth, tuning light–matter interactions and enhancing photocatalytic pathways.

4.2.4 Surface area. The inherently high surface area and tunable porosity of cellulose-based scaffolds significantly boost the photocatalytic performance by facilitating catalyst dispersion and mass transport. Shi *et al.* (2021) reported that the N_2 adsorption–desorption isotherms of Ag–ZnO/C nanocomposites exhibited a type IV profile, confirming their mesoporous nature. An increase in grinding time significantly influenced the development of the cellulose fiber network, leading to reduced pore diameters (90.43, 54.48, and 43.76 nm for Ag–ZnO/C10, C20, and C30) and increased specific surface areas (25.06, 31.49, and 40.64 m^2 g^{-1}), respectively. These trends are consistent with SEM observations, demonstrating that Ag–ZnO/C30 possesses the most developed porous structure, providing a larger effective surface for dye adsorption and photocatalytic degradation.[112]

The fibrillar cellulose networks prevent nanoparticle aggregation and maximize the number of exposed catalytic sites, ensuring effective interaction with organic contaminants. For example, Yan *et al.* (2023) emphasized that the specific surface area of CNF and ethylated CNF (ECNF) samples increases with the degree of substitution (DS), from 28.03 m^2 g^{-1} for CNF to 37.12 m^2 g^{-1} for ECNF-4, while SEM analysis confirmed that their morphology and size remain similar. A higher content of surface ethoxy groups promotes the formation of a 3D network with increased pore density due to electrostatic repulsion. Nitrogen adsorption–desorption isotherms (type III with H3 hysteresis) and FHH fractal analysis show that the surface roughness (D1) increases with DS, whereas the overall structural complexity (D2) remains comparable.[108] Alternatively, an interconnected porous architecture provides a large interfacial contact area, promoting rapid adsorption, accelerated reactant diffusion, and oxygen penetration in the catalyst unit. Liu *et al.* (2025) reported that the surface, cross-sectional, and longitudinal morphologies of CTC aerogels reveal a well-developed three-dimensional porous framework with a rough surface. This structure results from the light-weight network formed during the freezing process, with the aerogel density measuring 12.92 mg cm^{-3}. This highly porous architecture significantly enhances the surface activity of the composite. The SEM observations further show that TiO_2 nanoparticles are densely and uniformly anchored onto the aerogel skeleton (scale 5 μm), confirming their effective integration within the porous network.[113] In short, porous nano-cellulose scaffolds provide a huge contact area for both catalyst and pollutants, increasing the number of adsorption sites and ensuring that the reactants and oxygen diffuse quickly into the photocatalytic network.

5. Cellulose-supported photocatalysts

Cellulose-supported photocatalysts can be broadly classified into two general categories based on their material
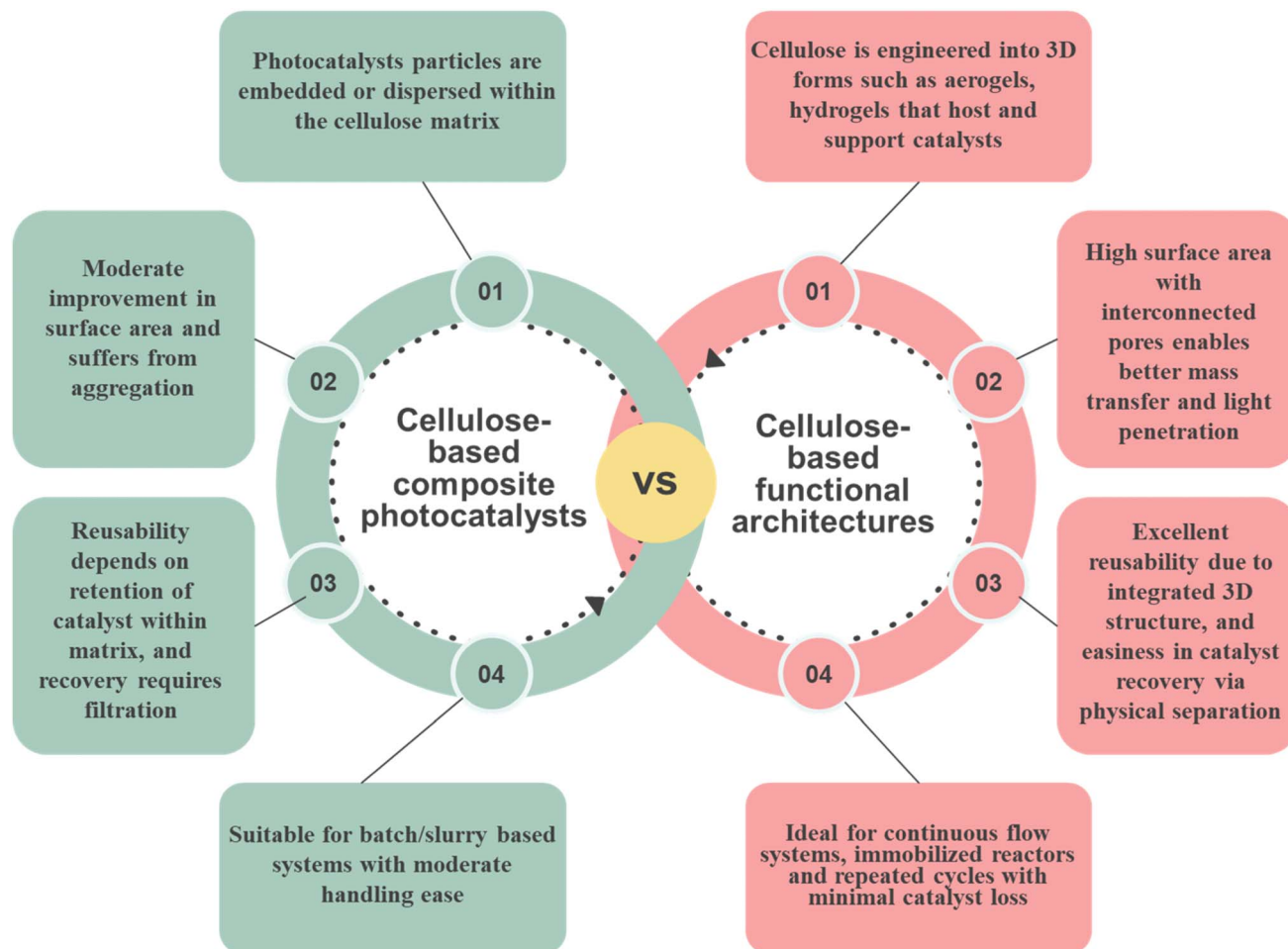
5482 | *J. Mater. Chem. A*, 2026, **14**, 5473–5519

This journal is © The Royal Society of Chemistry 2026

Fig. 5 Comparison between cellulose-supported photocatalysts with composite and functional architectures.

configuration and functional applications: (a) cellulose-based composite photocatalysts and (b) cellulose-based functional architecture photocatalysts. The first category of composite photocatalysts involves the direct integration of photocatalytic materials into a cellulose matrix to form homogeneous composites to enhance their dispersion, surface area, and charge separation. Structured systems, including hydrogels, aerogels, membranes, and 3D-printed forms, offer defined architecture, improved reusability and efficient mass transfer, making them suitable for continuous and multifunctional processes. The major differences between composite photocatalysts and cellulose-based functional architecture photocatalysts are presented in Fig. 5.

5.1 Cellulose-supported composite photocatalysts

Cellulose-based composite photocatalysts refer to hybrid materials in which photocatalytic components such as metal oxides (TiO_2 and ZnO), metal sulfides, carbon nitride, and MOFs are embedded or anchored onto a cellulose matrix. These composites leverage the high surface area, tunable porosity, and abundant functional groups of cellulose to enhance the dispersion, light absorption, and pollutant adsorption by the

photocatalyst. They are broadly classified into (i) metal-oxide cellulose-composite catalysts, (ii) metal sulfide cellulose catalysts, (iii) carbon nitride-supported cellulose catalysts, and (iv) MOF-supported cellulose catalysts.

5.1.1 Metal oxides. Metal oxides (ZnO, TiO_2, SnO_2, and ZrO_2) remain among the most widely employed photocatalysts due to their environmental compatibility, chemical robustness, and cost-effectiveness.[114,115] However, their intrinsic drawbacks such as wide band gaps, fast charge recombination, and morphology-dependent activity often limit their visible light performance.[116,117] In this case, integrating these oxides with cellulose-based biopolymers introduces structural and electronic advantages including improved dispersion, defect engineering, and enhanced adsorption, making cellulose–metal oxide hybrids a promising class of photocatalysts.

TiO_2 and ZnO are the most extensively investigated owing to their stability, abundance, and low toxicity.[20,118] However, their wide band gaps (3.2 and 3.37 eV, respectively) inherently restrict solar utilization, highlighting the importance of composite design strategies such as doping, heterojunction formation and morphology modulation.[119,120] A nano-chitosan (NCS), CMC, and TiO_2 composite was synthesized using a sol–gel strategy, where the incorporation of CMC induced visible light

This journal is © The Royal Society of Chemistry 2026

J. Mater. Chem. A, 2026, 14, 5473–5519 | 5483

absorption, with a redshift in absorption from 291 nm to 430 nm. The inclusion of CMC markedly transformed the morphology of TiO_2 from irregular, ruptured surfaces in NCS/TiO_2 to a more defined, needle-like and highly porous structure. This modification indicates the improved dispersion of TiO_2, enhanced lattice defects, and increased surface area, all contributing to more abundant active sites. This is correlated with the 95% degradation of crystal violet, underscoring that cellulose modifications can transcend mere dispersion and actively tune the electronic behavior of TiO_2. TGA and DSC analyses revealed high thermal stability, with 44.2% decomposition at 600 °C and a glass transition temperature of around 250 °C. These results collectively suggest that the extent to which cellulose influences the performance of TiO_2 is highly dependent on the synthesis strategy and interfacial bonding, not solely on the type of biopolymer employed.[121]

ZnO-based systems exhibit similar cellulose-dependent effects. Janpetch *et al.* (2016) fabricated ZnO/bacterial cellulose (BC) *via* solution plasma processing (SSP), where the BC nanofiber network served as a 3D scaffold guiding the diffusion and nucleation of Zn^{2+}. The strong dependence of the morphology of ZnO such as plate-like, rod-like (zinc nitrate) and multilayered sheets (zinc acetate) on the precursor and synthesis routes highlights a key advantage of cellulose, *i.e.*, its ability to modulate nanostructure evolution by ion anchoring and templating. SEM analysis showed that bacterial cellulose exhibited a web-like nanofiber structure, making it ideal for supporting the formation of ZnO (Fig. 6i). The ZnO/BC composites synthesized through SPP exhibited strong antibacterial activity against *E. coli* and *S. aureus*, primarily due to their Zn^{2+} ion release mechanism.[122] Li *et al.* (2020) further demonstrated that micro/nano-cellulose fibrils (MNCFs) significantly influence the growth kinetics of ZnO. Porous Al-doped ZnO/cellulose composites were prepared *via* chemical deposition, utilizing micro/nano cellulose fibers (MNCFs) as the substrate. The characterization studies reported a reduced fiber diameter from 100 to 31 nm, markedly decreased ZnO crystallite size from 40.6 to 14.2 nm, increased surface area of 27.5 $m^2 g^{-1}$, and enhanced porosity of 94.6%. Al-doping combined with the cellulose nanofibril scaffold lowered the band gap from 3.06 to
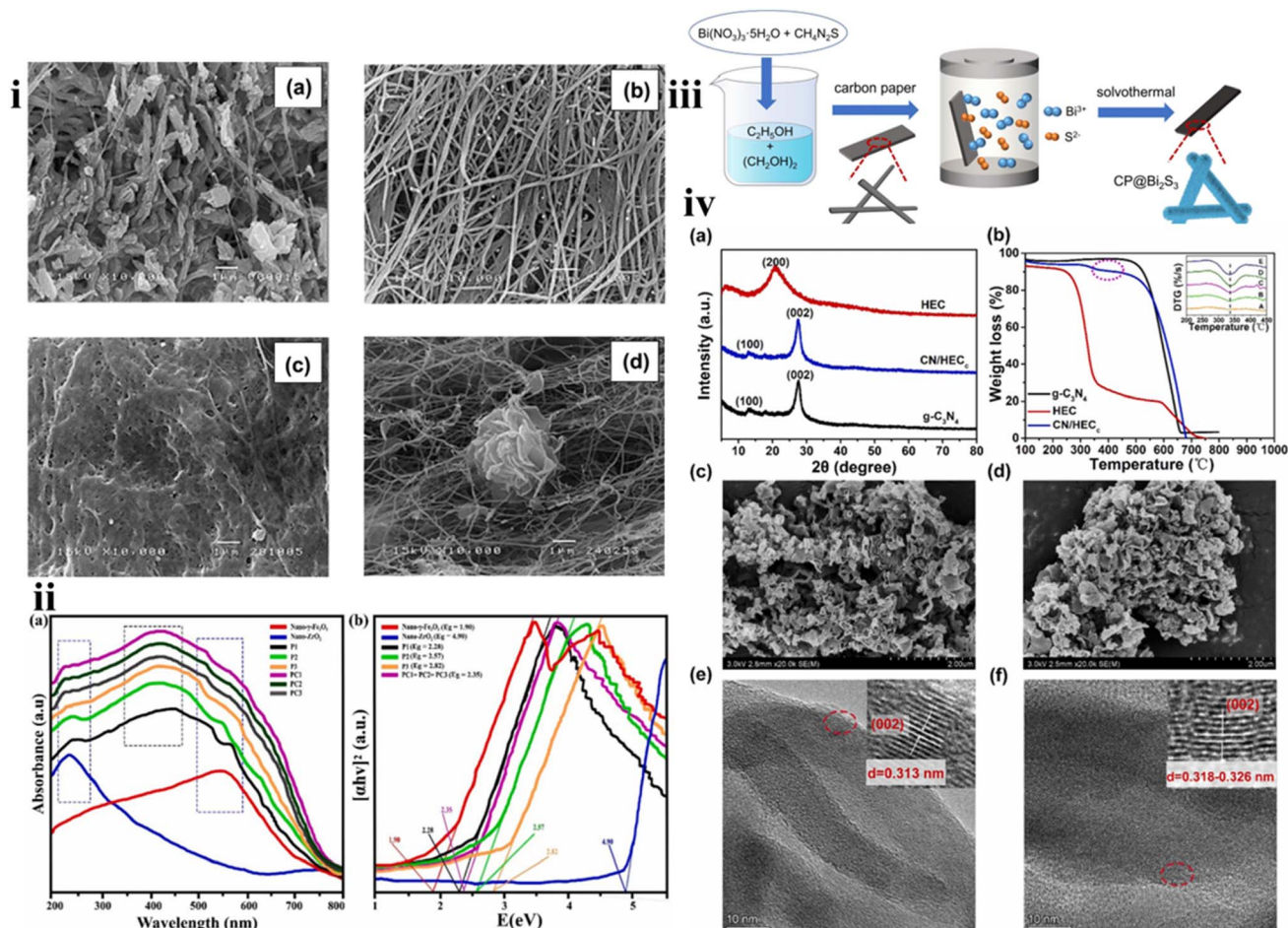

Fig. 6 (i(a–d)) SEM images of ZnO/BC composites. Reprinted with permission from ref. 122, Elsevier (2016). (ii) (a) UV-Vis DRS spectra and (b) band gap energy of different catalysts. Reprinted with permission from ref. 124, Elsevier (2022). (iii) Preparation of rime-like carbon paper@Bi_2S_3 hybrids *via* a one-step solvothermal process. Reprinted with permission from ref. 125, Elsevier (2022). (iv) (a) XRD spectra and (b) TGA curve of GCN-based photocatalyst. SEM images of (c) GCN and (d) GCN/HEC. TEM images of (e) GCN and (f) GCN/HEC. Reprinted with permission from ref. 126, Elsevier (2022).

5484 | *J. Mater. Chem. A*, 2026, **14**, 5473–5519

This journal is © The Royal Society of Chemistry 2026

2.92 eV and yielded 89% degradation of methyl orange under visible light. Notably, this system exhibited a synergistic interplay between cellulose microstructure and dopant chemistry, unlike the undoped systems where cellulose primarily influenced their morphology but not electronic structure. The thermal stability increased due to the presence of metal oxides, and UV-Vis analysis revealed a red shift in absorption with Al-doping and fiber interaction.[123]

Cellulose-based-γ-Fe$_2$O$_3$–ZrO$_2$ nanocomposites prepared *via* a simple sol–gel method demonstrated even more pronounced electric effects. The incorporation of ZrO$_2$ reduced the band gap of γ-Fe$_2$O$_3$ from 4.90 eV to 2.28 eV, enabling strong-light absorption, while cellulose enhanced the dispersion and surface roughness (Fig. 6ii). The nanocellulose did not considerably alter the band gap, it contributed to better dispersion and morphology, supporting the uniform distribution of the metal oxides. Microscopy revealed spherical to oval nanostructures with high surface roughness and porosity, while BET analysis indicated an increase in surface area from 412 m^2 g^{-1} for pure cellulose to 530 m^2 g^{-1} for the composite. The cellulose/γ-Fe$_2$O$_3$–ZrO$_2$ nanocomposite exhibited a crystallite size of 41.46 nm. Nanocellulose serves as a high-surface-area support in γ-Fe$_2$O$_3$–ZrO$_2$ heterojunction photocatalysts, enhancing electron–hole separation and pollutant adsorption, which synergistically boosted the visible light-driven degradation of Congo red up to 98.5%. Nanocellulose, with its high surface area, acts as an effective support for γ-Fe$_2$O$_3$–ZrO$_2$ heterojunction photocatalysts, synergistically enhancing electron–hole separation and pollutant adsorption. Compared to ZnO and TiO$_2$ systems, the Fe$_2$O$_3$–ZrO$_2$ heterojunction clearly benefitted more from cellulose-induced charge handling enhancements than from mere structural templating.[124]

The green synthesis of cellulose/ZrO$_2$ nanocomposites was achieved using a co-precipitation method *via* the incorporation of tetragonal ZrO$_2$ into a cellulose matrix without altering the crystal phase of cellulose. The FESEM and TEM analyses revealed the uniform dispersion of ZrO$_2$ nanoparticles within the biopolymer matrix, with no aggregation. The optical studies indicated a bathochromic shift in the UV-Vis absorption spectrum of the nanocomposite (from 258 nm to 288 nm) and a corresponding decrease in its band gap from 4.81 eV (ZrO$_2$) to 4.31 eV (cellulose/ZrO$_2$), which is attributed to its enhanced crystallinity and quantum confinement effects. The cellulose/ZrO$_2$ nanocomposite exhibited an enhanced performance for the photocatalytic degradation of methyl orange, achieving 76% within 50 min compared to 66% in pure ZrO$_2$ nanoparticles over 80 min.[127] This comparatively lower performance highlights that the cellulose–metal oxide synergy varies strongly with the electronic structure of the oxide, and thus wide band gap materials like ZrO$_2$ require additional interface engineering beyond the incorporation of cellulose to achieve meaningful photocatalytic gains.

Across, the metal oxide-based photocatalytic systems, a clear trend emerges, as follows: (i) cellulose enhances the dispersion, porosity, and adsorption in all the systems, (ii) electronic tuning occurs only when cellulose participates in chemical coordination or when combined with dopants or heterojunctions, and

(iii) mixed oxides show the strongest synergistic enhancement due to their complementary band structures and improved interfacial charge transfer. Thus, the performance window (76% to 98% degradation under visible light) is dictated not by the cellulose type alone but by the interplay between oxide electronic structure cellulose–oxide interfacial chemistry, and morphological engineering. These insights highlight that cellulose–metal oxide composites act as modular platforms, where their targeted chemical and structural design can unlock significantly enhanced visible light photocatalytic activity for diverse applications.

5.1.2 Metal sulfides. Metal sulphide-based semiconductors have emerged as promising photocatalysts due to their narrow band gaps, strong visible light absorption, abundant active sites, and favorable redox potentials.[128] Compared to conventional metal oxides, metal sulfides like CdS, CuS, ZnS, MoS$_2$, and Bi$_2$S$_3$ exhibit superior hydrogen generation capabilities and enhanced photoactivity towards wastewater remediation. Their electronic structures featuring d^{10} cations and S 3p orbitals contribute to efficient charge separation and light harvesting.[129] Moreover, their unique nanostructures and surface-active sites, particularly at the S-edge and defect zones, further boost their catalytic activity. Integrating metal sulfides with cellulose enhances their dispersion, stability, and reusability. This synergistic combination holds great potential for developing efficient and eco-friendly photocatalytic systems.

Zhang *et al.* engineered a uniformly anchored CuS–cellulose composite using polydopamine (PDA) as a robust bio-inspired adhesive. PDA enabled strong Cu^{2+} chelation through its abundant catechol groups, promoting homogeneous CuS nucleation on the cellulose fibers and effectively suppressing photocorrosion. The pre-doping strategy ensured the maximum metal–ligand coordination, while *in situ* polymerization and sulfide treatment yielded flexible CuS-coated cellulose paper through conventional papermaking. The SEM/EDS analysis confirmed that PDA transformed the inherently agglomerated CuS morphology into a densely distributed nanostructure, while BET measurements revealed a markedly increased surface area (48 m^2 g^{-1}). The improved dispersion and the PDA-mediated charge-separation pathway enhanced the photocatalytic activity, with the composite showing up to a 5.8-fold higher degradation efficiency than CuS on untreated fibers.[130] Wang *et al.* constructed multifunctional photocatalytic paper by coupling reduced graphene oxide (rGO) and CuS with dialdehyde cellulose fibers (DACF) through hyperbranched polyamide-amine (HPAMAM), which served as both a covalent linker and a nanoreactor for the controlled growth of CuS. The Schiff-base bonding between DACF and HPAMAM/rGO facilitated stable immobilization, while the branched polymer confined the nucleation of CuS into uniformly dispersed nanoclusters. The structural analyses showed the retention of the cellulose I framework with increased amorphous character, weakened rGO stacking, and well-defined CuS diffraction peaks. SEM revealed that HPAMAM was essential for avoiding the agglomeration of rGO/CuS and achieving intimate nanoscale contact. The hierarchical structure improved charge separation and mechanical stability, leading to a 2.7-fold increase in the

This journal is © The Royal Society of Chemistry 2026

J. Mater. Chem. A, 2026, **14**, 5473–5519 | **5485**

degradation rate of RhB and excellent reusability (>90% after ten cycles).[131]

Xu et al. (2022) synthesized rime-like carbon paper@Bi_2S_3 hybrids via a one-step solvothermal process (Fig. 6iii), where the precursor concentration controlled the density and morphology of Bi_2S_3 nanorods. The cellulose-derived carbon fibers (8 μm), retaining surface hydroxyl residues, intrinsic chirality, and a naturally wrinkled porous texture, provided abundant nucleation sites, which directed the crystallization of Bi_2S_3. The low precursor levels (CB-1) yielded sparse deposition, whereas CB-2 and CB-3 supported the formation of dense, flower-like Bi_2S_3 clusters by elongated nanorods through accelerated axial growth and Ostwald ripening. XRD, Raman spectroscopy, and XPS confirmed the presence of orthorhombic Bi_2S_3, preserved carbon structure, and strong Bi–S–C interfacial contact. Importantly, the hierarchical carbon scaffold enhanced the anchoring of Bi_2S_3, improved the interfacial polarization, and strengthened the impedance matching attributes directly related to the cellulose-origin hydroxyl functionality, chiral microstructure, and high porosity. These synergistic interfaces enabled multiple attenuation pathways, resulting in a significantly improved microwave absorption performance.[125]

Jiang et al. (2020) synthesized berry-like CdS/MoS_2 structures using bacterial cellulose (BC) as a bio-template, where the intrinsic hydroxyl-rich, chiral nanofibrillar network of BC played a decisive role in directing the nucleation of CdS. The abundant surface –OH groups and the naturally twisted, porous architecture enabled uniform Cd^{2+} anchoring and confined CdS crystallization into nanoscale domains, effectively suppressing agglomeration and increasing the active surface area. The subsequent integration of ultrathin MoS_2 nanosheets produced tightly interfaced $CdS–MoS_2$ heterojunctions, which facilitated rapid charge transfer. The optimized composite exhibited a higher surface area (21.8 m^2 g^{-1}) and enlarged mesopores (6.95 nm), attributes arising from the BC-derived scaffold, which enhanced the light harvesting and reaction-site accessibility. High-resolution analyses confirmed the intimate MoS_2–CdS contact and homogeneous elemental distribution. Benefiting from both the heterojunction and the cellulose-origin structural features (hydroxyl coordination, chiral fiber templating, and hierarchical porosity), the composite achieved an impressive H_2 evolution rate of 63.59 ± 1.20 mmol g^{-1} h^{-1} with strong recyclability driven by its stabilized charge separation and improved catalyst dispersion.[132] Tavker et al. (2020) synthesized MoS_2 nano-petals anchored on cellulose through an in situ hydrothermal method, where the hydroxyl-rich, chiral, and porous microfibrillar structure of cellulose acted as a sustainable scaffold that directed the nucleation and orientation of MoS_2. The abundant –OH groups on cellulose promoted strong interfacial bonding with the Mo precursors, enabling the uniform growth of MoS_2 and preventing the restacking of the nanosheets, while the intrinsic helical fibril arrangement and porous network provided spatial confinement for the formation of petal-like architectures. XRD, XPS, HRTEM, and SAED confirmed the formation of well-defined MoS_2 nano-petals with robust MoS_2 cellulose interactions. The resulting composite displayed a high surface area (60 m^2 g^{-1}) and

reduced pore size (2 nm), enhancing dye adsorption and light utilization. This cellulose-guided architecture facilitated efficient charge transfer, suppressed electron–hole recombination, and improved carrier mobility, while the hierarchical nanopetals increased the light scattering and active-site density. Consequently, the MoS_2@cellulose system delivered rapid photocatalytic degradation of RhB and industrial dyes within 25 min, with its performance directly linked to the synergistic effects of the hydroxyl functionality, chiral templating, and porous structure of cellulose.[133]

Liao et al. (2023) constructed a 3D Z-scheme In_2S_3–C/Fe_3C photocatalyst in which the conductive carbon framework derived from cellulose played a central role in mediating charge flow and stabilizing its active components. The cellulose precursor, which is rich in OH groups, chiral microfibril ordering, and hierarchical porosity, enabled uniform impregnation and carbonization, generating a high-surface-area carbon scaffold with abundant anchoring sites for In_2S_3 nucleation. The band alignment and photo-deposition results showed that In_2S_3 and Fe_3C serve as the reduction and oxidation centers, respectively, while DFT calculations revealed that Fe_3C lowers the barrier for *CO → *COH coupling and weakens the In–S bonds, enhancing the selectivity for acetate. Compared with pristine In_2S_3 (λ < 545 nm), the composite exhibited broad-spectrum absorption due to its metallic carbon–Fe_3C matrix. The Z-scheme electron-transfer pathway between Fe_3C and In_2S_3 facilitated by the cellulose-derived conductive network suppressed photocorrosion, promoted charge separation, and increased the accessible active sites. These synergistic effects resulted in efficient and selective acetate production (11.33 μmol h^{-1} g^{-1}, 89% selectivity) with excellent structural and photocatalytic stability, which are directly linked to the templating, porosity, and electron-transport properties imparted by the cellulose backbone.[134]

Liang et al. (2023) synthesized a $Bi_2O_3/Zn_3In_2S_6$ (BO/ZIS) S-type heterojunction via a hydrothermal route and immobilized it on sugarcane-bagasse-derived cellulose (SBC). SEM imaging confirmed that the flower-like $Zn_3In_2S_6$ and flaky Bi_2O_3 were assembled into compact nanospheres that were uniformly anchored onto the cellulose fibers. The abundant –OH groups, hierarchical porosity, and microfibrillar network of SBC promoted strong interfacial bonding, homogeneous nanoparticle dispersion, and efficient deposition of the BO/ZIS units. The BET analysis revealed that supporting the catalyst on SBC significantly increased its specific surface area (91.79 m^2 g^{-1}), while preserving its mesoporosity, thereby improving the adsorption of pollutants and the reactant–catalyst contact. The photophysical characterization (PL, photocurrent response, and EIS) demonstrated that the cellulose scaffold further enhanced the charge separation within the S-type heterojunction by providing a conductive, low-resistance interface, which facilitated electron transport and reduced recombination. The improved dispersion and stabilized interfacial architecture contributed to faster mass transfer, higher density of accessible active sites, and better utilization of photogenerated carriers. Catalytically, SBC/BO/ZIS-30 achieved 97% degradation of 2,4-

5486 | J. Mater. Chem. A, 2026, **14**, 5473–5519

This journal is © The Royal Society of Chemistry 2026

DCP at neutral pH (0.3 g L^{-1}), outperforming the unsupported BO/ZIS composite.[135]

Across these reports, the response of different metal sulfides to the cellulose support varies according to their crystal structures, intrinsic stability, and surface chemistry. CuS, which readily undergoes photocorrosion, shows the strongest improvement when cellulose introduces chelating groups (PDA–catechol), which stabilize Cu^{2+} and promote its uniform nucleation. Differently, CdS benefits primarily from photocorrosion suppression and heterojunction formation, where the BC scaffold regulates its particle size and enables intimate CdS–MoS$_2$ contact. The layered MoS$_2$ interacts differently, as cellulose templating directs the formation of nanosheets or petals, increasing the edge-site density and accelerating charge transport. In contrast, Bi$_2$S$_3$, as an anisotropic 1D sulfide, exhibits morphology-dependent growth on carbonized cellulose due to its improved axial orientation and interfacial polarization. In the case of In$_2$S$_3$, cellulose-derived carbon frameworks provide conductivity and Z-scheme electron mediation, mitigating self-corrosion. Zn$_3$In$_2$S$_6$ shows an enhanced photocatalytic response when cellulose stabilizes S-type heterojunctions and maintains the mesoporosity. These differences demonstrate that cellulose does not act uniformly across all metal sulfides; rather, its hydroxyl-rich, porous, and tunable surface interacts uniquely with the growth mechanism, band structure, and stability of each sulfide, generating distinct performance outcomes.

5.1.3 Cellulose-supported carbon nitride photocatalysts. Cellulose-based carbon nitride photocatalysts represent a rapidly emerging class of metal-free hybrid materials engineered to overcome the intrinsic drawbacks of pristine g-C$_3$N$_4$ (GCN), namely its low surface area, limited active sites, and inefficient charge separation. Across recent studies, cellulose has consistently demonstrated a dual functional role: (i) a structural scaffold enabling nanoscale dispersion, hierarchical porosity, and chemical stability and (ii) an electronic/proton mediator, introducing interfacial interactions that facilitate charge transport, suppress recombination, and enhance redox reaction kinetics. A critical comparison of the representative systems highlights how the chemistry, morphology, and surface functionality of cellulose directly dictate photocatalytic outcomes.

In the GCN/hydroxyethyl cellulose (HEC) system reported by Zhang *et al.*, HEC acts as a solid proton donor, creating hydrogen-bond networks that promote proton-coupled electron transfer (PCET). Alternatively, HEC$_c$ reduces the BET surface area (71.70 to 51.79 m^2 g^{-1}). SEM and TEM confirm that GCN/HEC$_c$ retains the nanosheet morphology, while HEC$_c$ uniformly modifies GCN, slightly expanding its interplanar spacing, which facilitates enhanced charge transfer and H$_2$O$_2$ generation. The characteristic peaks at 27.64° and 13.19° indicated the presence of conjugated aromatic stacking and tri-*s*-triazine units, with a crystallite size of 9.3 nm (Fig. 6iva). TGA/DTG analysis (Fig. 6ivb) shows that HEC undergoes major decomposition (73%) at 220–380 °C, while g-C$_3$N$_4$ remains stable, and the GCN/HEC$_c$ composites only exhibit slight weight loss (0–5.1%), which increases with the HEC$_c$ content. The SEM (Fig. 6ivc and d) and XRD results show an expanded interlayer spacing and improved

nanosheet integrity, enabling more efficient charge transport. The optical absorption studies revealed that the band gap (2.93 eV) remained unchanged upon modification with HEC$_c$, indicating no significant alteration in electronic structure. The resulting 52.6% enhancement in H$_2$O$_2$ production and twofold increase in photocurrent explicitly validate the role of cellulose as an electronic modulator, independent of the surface-area-driven pathways.[126]

Xu *et al.* (2023) synthesized a BiYO$_3$/GCN/CNF composite *via* electrostatic self-assembly, achieving notable improvements in visible-light photocatalytic activity. The formation of a heterojunction between BiYO$_3$ and GCN facilitates efficient charge separation and transfer, mitigating the rapid electron–hole recombination commonly observed in pure GCN. The CNFs act as a high-surface-area, porous scaffold, preventing the agglomeration of the nanoparticles and enhancing their dispersibility, which increases the accessibility to the active sites and improves the adsorption of pollutants. SEM and TEM analyses revealed that the BiYO$_3$ nanosheet petals and GCN nanoflakes form a tight nanosheet structure, enabling intimate interfacial contact for the rapid migration of photogenerated carriers. The BET and BJH measurements showed that the inclusion of CNFs increased the surface area from 47 to 66 m^2 g^{-1} and pore volume to 0.35 cm^3 g^{-1}, directly correlating with the enhanced adsorption of tetracycline (TC) molecules and faster photocatalytic reactions. The optical studies demonstrated narrowed band gaps for GCN (2.54 eV) and BiYO$_3$ (2.61 eV), with well-aligned conduction and valence band positions, promoting effective electron transfer within the heterojunction. Consequently, the BiYO$_3$/GCN/CNF composite achieved 97% TC degradation. Critically, the CNFs not only serve as a structural support but also synergistically enhance the photocatalytic performance by combining adsorption with light-driven charge separation, while facilitating easy catalyst recovery and recyclability.[136]

Zhao *et al.* (2021) constructed a ternary Z-scheme photocatalyst composed of carbon-doped GCN and WO$_3$, which was synthesized through a multi-step process involving hydrothermal impregnation with nanocrystals, high-temperature calcination, and electrostatic self-assembly with WO$_3$ nanocuboids. The prepared composites exhibited the beneficial of a porous structure, a high specific surface area of 57 m^2 g^{-1}, carbon substitution, and the construction of a Z-scheme heterojunction. These features collectively contributed to a narrowed band gap, enhanced visible light absorption, improved charge carrier separation, and redox capabilities.[137] Kapok fiber (t-KF), a cellulose-based microtubular structure, has been employed as a solid electron donor to enhance the photocatalytic activity of carbon-doped GCN (CCN) *via* the ligand-to-metal charge transfer (LMCT) mechanism. The cellulose scaffold provides a high-surface-area and biocompatible support that improves the dispersibility, structural integrity, and accessibility to the active sites of CCN. Using succinic acid (SA) as a cross-linker, CCN was successfully grafted onto t-KF through a hydrothermal process, forming a hybrid complex with the uniform distribution of CCN on the fiber surface and inner tubular structure. FESEM and TEM analyses confirmed

This journal is © The Royal Society of Chemistry 2026

J. Mater. Chem. A, 2026, **14**, 5473–5519 | **5487**

the formation of well-dispersed, thicker CCN layers in CCN-SA/t-KF, while FTIR spectra indicated the effective immobilization of CCN without altering its characteristic structure. BET/BJH analysis revealed that the incorporation of SA enhanced the surface area and mesoporosity, further facilitating the adsorption of the reactants and charge transfer. The LMCT interactions between the hydroxyl groups of cellulose and amine groups on CCN synergistically improved the interfacial electron transfer, resulting in 1.8-fold higher H_2O_2 generation under visible light compared to pristine GCN. This study underscores the critical role of cellulose as a structural and functional support, enabling better dispersion, enhanced charge separation, and improved photocatalytic performance.[138]

Cellulose is not a passive support but an active photocatalytic co-participant whose chemical identity, degree of substitution, and multiscale morphology determine the governing mechanism such as PCET (HEC), adsorption–charge synergy (CNFs), and LMCT (t-KF). Key comparative insights include: (i) charge transport: HEC and t-KF outperform CNFs in electronic modulation due to the stronger proton- or ligand-mediated coupling with g-C_3N_4. (ii) Surface area and adsorption: CNFs deliver the most substantial textural enhancements, resulting in superior pollutant preconcentration and more complete degradation pathways. (iii) Interfacial integration: kapok fibers enable the thickest and most uniform CN deposition, enhancing long-term recyclability and mechanical durability. Collectively, these studies underscore that cellulose selection is a decisive variable not a secondary material component in dictating the architecture, interfacial electronic coupling, and reaction kinetics of g-C_3N_4 photocatalysts. Strategic control over the chemistry and multiscale structure of cellulose enables the fabrication of tailored hybrid systems with enhanced redox potential, enriched active sites, and superior charge–mass transport characteristics. Thus, the high-level synergy between the cellulose framework and GCN represents a powerful blueprint for next-generation sustainable photocatalysts, with direct implications for environmental remediation, energy conversion, and green chemical synthesis.

5.1.4 Cellulose-supported MOFs. The integration of metal–organic frameworks (MOFs) with cellulose has emerged as a powerful strategy to overcome the longstanding challenges associated with the fragility, particle agglomeration, and limited processability of MOFs. MOFs offer exceptional porosity, tunable chemistry, and strong visible-light responsiveness; however, their standalone performance is often compromised by their poor mechanical robustness and inefficient charge utilization. Cellulose, whether as carboxymethyl cellulose (CMC), bacterial cellulose (BC), carbonized fibers (CCF), or cotton fabric, functions as more than a passive support. Its hydroxyl-rich, hydrophilic, and hierarchically structured architecture enables precise control over the nucleation, dispersion, charge transport, and macroscopic formability of MOFs, making cellulose-supported MOFs compelling platforms for photocatalysis.[139–141]

Khodayari et al. (2024) reported the successful fabrication of CMC/MIL-101(Fe)/CuO biocomposites for photocatalytic applications. MIL-101(Fe) retains its characteristic octahedral morphology upon integration with CMC and CuO, indicating its high structural stability. FTIR, XRD, SEM, and DRS analyses confirmed the successful synthesis of the CMC/MIL/CuO biocomposite, with CMC providing abundant OH^- groups that enhance the binding, dispersion, and stability of MIL-101(Fe) and CuO. The amorphous CMC matrix acts as a scaffold, preventing aggregation and preserving the crystalline structure of MIL-101(Fe), while promoting synergistic interactions that lower the band gap to 2.1 eV. Here, CMC not only enhances the dispersion of MIL-101(Fe) and CuO but also promotes interfacial charge transfer, enabling >90% pollutant removal under visible light. The synergistic interaction between the hydroxyl groups of CMC and Fe–O clusters of MIL-101(Fe) demonstrates the ability of cellulose to modulate electronic structure through chemical coupling.[142] Zheng et al. (2024) developed a photocatalyst by integrating MOF-derived carbon skeleton (MDCS)-encapsulated Ni nanoparticles and BiOBr onto carbonized cellulose fibers (CCF) using polydopamine as a template and anchoring agent. In contrast, CCF/PDA-C/Ni@MDCS/BiOBr composites employ cellulose fibers as a thermally resilient scaffold that enables the targeted growth of Ni-MOFs, which are converted into MOF-derived carbon skeletons (MDCS). The resulting hierarchical structure (surface area > 1100 m^2 g^{-1}) significantly enhances the charge mobility and reactant diffusion. Here, cellulose indirectly governs photocatalytic performance by dictating the spatial organization of Ni nanoparticles and BiOBr nanosheets, yielding narrowed band gaps (1.49 eV) and high stability over 10 cycles. This study exemplifies the ability of cellulose to accommodate multi-component hybrid architectures without compromising structural coherence. This highlights the synergistic role of CCF in improving the photocatalytic efficiency, structural robustness, and reactant diffusion.[143]

Cellulose nanocrystals (CNCs), owing to their inherent helical rod-like morphology, impart topological chirality when integrated into ZIF-8, forming CNCs@ZIF-8 3D networks that link individual ZIF-8 crystals into ordered architectures. This chiral structuring enhances the spatial confinement of the micro- and nano-scale reaction sites, improves light penetration, and facilitates mass transport, distinguishing it from pristine ZIF-8, which lacks optical activity and forms isolated truncated rhombic dodecahedra. Optical characterization reveals that CNCs@ZIF-8 exhibits positive optical rotation (α = +12.224 to +21.290) and circular dichroism signals, with higher chirality correlating positively with photocatalytic CO_2 reduction (up to 301.16 μmol g^{-1} for α = +21.290, 9.43-times higher than ZIF-8), highlighting the functional role of chirality in enhancing light–matter interactions and charge separation. The interfacial formation of Zn–O–S and Zn–N–S bonds promotes electron delocalization and reduces electron–hole recombination, as confirmed by photoluminescence studies, while the negative surface charge from CNCs stabilizes the 3D network via electrostatic assembly. Despite the decrease in specific surface area and mesoporosity at higher CNC content (from 1084.27 to 226.25 m^2 g^{-1}), the chiral network maintains recyclability and structural robustness over multiple cycles, underscoring the dual structural and electronic role of CNCs. Overall, CNCs

5488 | J. Mater. Chem. A, 2026, **14**, 5473–5519

This journal is © The Royal Society of Chemistry 2026

function not merely as passive scaffolds but as active chiral auxiliaries that simultaneously modulate the network topology, optical properties, and electron transport, providing a novel strategy for enhancing the performance of metal-free photocatalysts in CO_2 reduction.[144]

Jiang et al. (2024) proposed Zr-MOF exhibiting strong aggregation-induced emission, which was successfully synthesized in situ on bacterial cellulose, forming fluorescent nanofibers. By optimizing the $ZrCl_4$ to BC ratio and using regulators, a uniform monolayer MOF coating was attained using the solvothermal method. The hydroxyl-rich BC served as a growth template, enabling uniform MOF deposition and yielding a core–shell, string-bead morphology with well-dispersed 150 nm MOF nanoparticles. This composite displayed a significantly enhanced surface area of 1116 m^2 g^{-1} and microporous structure, outperforming pristine MOFs due to the restricted agglomeration and optimized crystal growth via the spatial confinement of BC. Additionally, BC@Zr-MOF showed improved thermal stability and stronger fluorescence with better pH resistance compared to pure MOFs, highlighting its potential in optical sensing and catalytic applications.[145] Yuan et al. (2023) constructed shapeable and rebuildable MIL-53@cellulose fiber composites by ultrasonically integrating MIL-53(Fe) with cellulose fibers. Nitrogen adsorption isotherms showed type IV behavior with pronounced hysteresis, confirming well-developed mesoporosity and a surface area of 9.75 m^2 g^{-1}. The MIL-53 (De) crystals uniformly grew on CF and bonded with surface nanofibrils via hydrogen bonding and physical

crosslinking, yielding a high compressive strength of 3.53 MPa. Cellulose provided abundant hydroxyl groups, which facilitated adsorption and supported the uniform dispersion of the photocatalyst, enabling >95% TC degradation in 15 min with H_2O_2 under visible light. CF enhances the porosity and surface area and reinforces the mechanical strength, ensuring both structural integrity and high adsorption/photocatalytic performance.[146]

Across these systems, three unifying structure–property relationships emerge: (i) dispersion and interface engineering: the abundant –OH groups in cellulose strongly interact with the MOF metal nodes and organic linkers, preventing the aggregation and enabling the uniform distribution of the nanoparticles. Systems with highest uniformity (e.g., Ni@MDCS/BiOBr and Zr-MOF@BC) exhibit the largest improvements in charge separation efficiency and photocatalytic rate constants. (ii) Hierarchical porosity and mass transport: cellulose supports from nanofibrils to woven cotton govern macroscopic porosity, facilitating reactant accessibility and light penetration. Composites with multiscale porosity (CCF/PDA-C/Ni@MDCS/BiOBr) consistently achieve superior dye degradation due to their enhanced substrate–catalyst contact. (iii) Electronic modulation and band-gap tailoring: interfacial interactions with cellulose can tune band gaps and alter defect states, as observed in CMC/MIL-101(Fe)/CuO and Ag_3VO_4@MIL-125-NH_2@cotton. The cellulose–MOF junction promotes charge transfer by creating a local electric field, improving the photocatalytic quantum efficiency. Overall, cellulose acts as
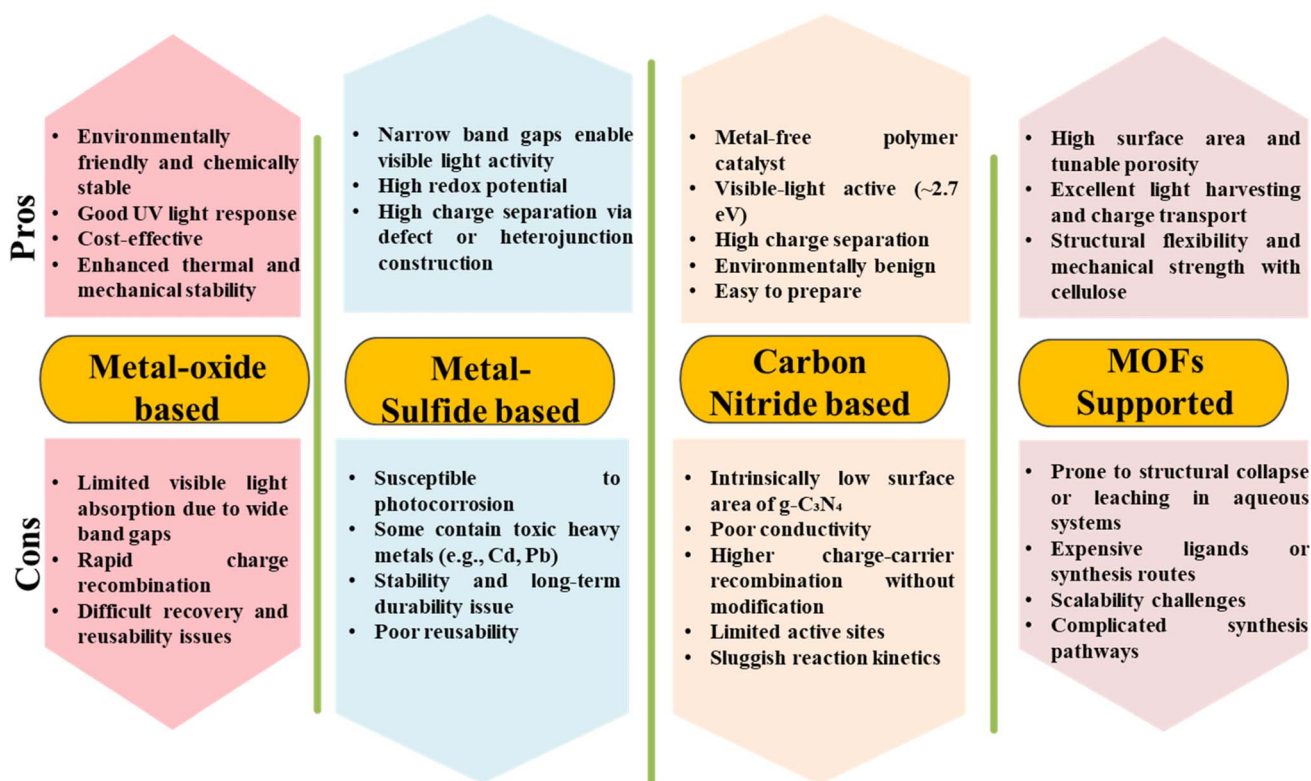

Fig. 7 Pros and cons of cellulose-supported composite photocatalysts employed in diverse applications.

This journal is © The Royal Society of Chemistry 2026

J. Mater. Chem. A, 2026, **14**, 5473–5519 | **5489**

a structural, chemical, and electronic regulator within MOF-based photocatalysts. Its influence extends from nanoscale MOF nucleation and band-gap engineering to macroscopic reusability and processability. The current body of work unequivocally demonstrates that cellulose is not merely a support material but a decisive performance-enabling component, determining photocatalytic efficiency, stability, and architectural versatility.

A horizontal comparison of cellulose-based composite catalysts illuminate that cellulose not only enhances the catalytic activity, but it influences the intrinsic band structure, chemistry and stability of photocatalysts. Fig. 7 presents an overview of the advantages and limitations of four major classes of cellulose-supported photocatalysts. In the case of metal oxides, cellulose primarily improves their dispersion, introduces hydroxyl-rich anchoring sites, and enhances the adsorption of pollutants; however, their broad band gaps and high recombination ratios limit the utilization of visible light even in the presence of cellulose. Metal sulfides exhibit a more pronounced response because their narrow band gaps and defect densities permit stronger interfacial electronic coupling with cellulose *via* electron/proton donation, though photocorrosion remains a major performance-limiting parameter, which cellulose can partially mitigate in photocatalysis. Cellulose-GCN hybrids display the strongest synergistic effects *via* their hydrogen-bonded networks, proton-coupled electron transfer pathways, and strengthened heterointerfaces, which significantly boost charge mobility, lower the recombination ratio, and enrich the availability of active sites. MOF-supported systems feature tunable porosity, large surface area, and structural synergy with cellulose, but face issues of structural collapse in aqueous media, high synthesis costs, and scalability constraints. These differences arise from the variations in their interfacial electron transfer compatibility with the functional groups in cellulose, band alignment and charge-carrier kinetics, and ability of cellulose to modulate the electron density at the interface of semiconductors.

5.2 Structured cellulose-based photocatalytic systems

Cellulose-derived functional structures are engineered materials developed from cellulose that are designed to perform specific tasks such as catalysis and adsorption, often through chemical modification and the incorporation of functional agents. The processing of cellulose into forms such as sponges, hydrogels, and aerogels enables it to serve as a porous, flexible, and mechanically stable scaffold. The construction of functional structures is ideal for photocatalytic applications due to (i) the improved utilization of visible light *via* electron supply, (ii) higher reusability and ease of recovery, (iii) enhanced oxygen adsorption, (iv) excellent structural stability and mechanical strength, (v) tunable porosity for efficient mass transfer, and (vi) the ability to support multifunctional catalytic sites for synergistic reactions. Table 4 presents a detailed comparative overview of cellulose-based hydrogels, sponges, and aerogels, and membrane-based photocatalysts.

5.2.1 Hydrogels. Cellulose-based hydrogels have emerged as a versatile class of photocatalytic platforms owing to their intrinsic biodegradability, hydrophilicity, and facile chemical tunability. However, pristine cellulose hydrogels suffer from low mechanical strength, insufficient visible-light activity, and limited adsorption capacity, restricting their standalone photocatalytic applicability. Recent studies have addressed these limitations through the rational integration of functional nanomaterials, and a comparative evaluation of these systems highlights the active, system-defining role of cellulose far beyond that of a passive supporting matrix.[32] Ren *et al.* (2022) demonstrated that cellulose can serve as an interfacial engineering framework, enabling the *in situ* nucleation and homogeneous distribution of SiO_2 and ZnO within a hydrogel. Unlike conventional hydrogel scaffolds, where inorganic fillers tend to aggregate, the abundant –OH groups on cellulose nanofibrils function as specific nucleation centers, generating a highly interconnected ZnO/SiO_2 heterojunction with defect-rich interfaces. This controlled architecture not only enhanced electron migration (ZnO $\rightarrow$ SiO_2 impurity levels) but also improved the mechanical integrity and porosity. Consequently, this system achieved 95% MB degradation within 120 min and maintained >90% efficiency after eight cycles, underscoring the critical role of cellulose in structural robustness and long-term catalytic durability.[147]

A distinct yet complementary function of cellulose is evident in the CMC–NGO–ZnO–ZnO_2 hydrogel.[148] Here, CMC directed the nanoscale dispersion and chemical integration of dual Zn-based phases on amine-modified graphene oxide. SEM and TEM analyses revealed that the cellulose matrix prevented rod-like ZnO and particulate ZnO_2 aggregation, while mediating tight heterojunction interfaces, which are essential conditions for rapid interfacial charge migration. Chemical analyses (FTIR and XPS) confirmed strong bonding among CMC, NGO, and Zn-based oxides. These interactions not only lowered the band gap (3.17 eV $\rightarrow$ 3.11 eV) but also promoted synergistic radical generation ($^{\bullet}O_2^-$, and $^{\bullet}OH$), enabling 100% dye degradation. The contrast with the system reported by Ren *et al.* highlights an important distinction, *i.e.*, while cellulose in ZnO/SiO_2 strengthened the mechanical and interfacial frameworks, CMC here functioned as an electron transport mediator and heterojunction stabilizer, directly influencing the band structure and charge dynamics.[149] Comparing these two systems underscores that the functional form of cellulose (nanofibrillar cellulose *vs.* CMC) fundamentally dictates the photocatalyst architecture, interface chemistry, and electronic behavior, positioning cellulose as an active modulator of both physicochemical and photocatalytic properties.

Qi *et al.* (2024) employed cellulose nanofibrils (CN) as a high-surface-area reinforcement scaffold in a titanate nanofiber–CdS (TN–CdS) hydrogel. Unlike the previous two systems, where cellulose primarily served interfacial electronic roles, here cellulose dictated the mass transfer, swelling behavior, and accessible surface area. The formation of a 3D porous hydrogel increased the BET surface area dramatically (31.9 m^2 g^{-1} *vs.* 6.70 m^2 g^{-1} for CN and 0.56 m^2 g^{-1} for TN–CdS). This cellulose-

5490 | *J. Mater. Chem. A*, 2026, **14**, 5473–5519

This journal is © The Royal Society of Chemistry 2026

Table 4 Comparative overview of cellulose-supported hydrogels, sponges, aerogels, and membranes for photocatalysis

Criteria	Hydrogels	Sponges	Aerogels	Membranes
Structure	3D-crosslinked hydrophilic network; water-swollen	Macroporous 3D framework with moderate porosity	Ultra-light 3D porous network with very high porosity and surface area	Thin 2D layer or fibrous mat with controlled porosity
Porosity	Moderate to high	Moderate	Very high (>90%)	Variable, often lower than aerogels
Preparation methods	Simple polymerization and crosslinking	Freeze-drying or thermal foaming	Sol–gel process and freeze drying	Electrospinning, casting, and phase inversion
Mechanical strength	Soft, elastic, weak when swollen	Higher strength, compressible	Fragile without reinforcement	High mechanical stability and flexibility
Surface area	Moderate	Low to moderate	High (up to 500 $m^2\ g^{-1}$)	Moderate
Photocatalytic efficiency	Moderate; affected by diffusion limits	Moderate; better for floating catalysts	High due to high active area	High with good contact and flow-through operation
Reusability	Can be reused; shape may deform	Reusable; compressible	Reusable; may need crosslinking for stability	Highly reusable; easy to handle and wash
Advantages	-Biocompatible	-Easy handling	-Highest porosity and surface area	-Good scalability
	-High water uptake	-Good mechanical stability	-Lightweight	-Ideal for continuous-flow systems
	-Easy synthesis	-Suitable for floating systems	-Excellent for adsorption–photocatalysis	
Disadvantages	-Swelling can weaken the structure	-Lower surface area	-Brittle unless reinforced	-Possible nanoparticle leaching
	-Low mechanical integrity	-Limited catalyst loading	-Complex fabrication	-Lower surface area than aerogels
			-Not ideal for flow systems	
Challenges	-Maintaining shape and structure during operation	-Uniformity in structure	-High energy consumption for dryingp	-Achieving homogeneous nanoparticle distribution
	-Ensuring catalyst stability	-Long-term stability in harsh conditions	-Scaling up with uniformity	-Managing fouling and long-term use

enabled structural openness significantly improved the dispersion and facilitated efficient light harvesting and reactant diffusion. As a result, the composite achieved a reduction rate constant of 0.0586 min^{-1}. Additionally, CdS functioned within a Z-scheme mechanism, benefiting from the stable, hydrated cellulose matrix, which prevented nanoparticle recombination and deactivation. In this system, cellulose is not primarily an electronic mediator but a mass-transfer enhancer and structural stabilizer, enabling high photocatalytic efficiency through improved accessibility and reactant mobility.[150]

The integration of photocatalysts into cellulose-based hydrogels enables the creation of multifunctional composites, where cellulose governs their mechanical durability, porous architecture, charge separation dynamics, and catalytic stability. A critical comparison reveals that the role of cellulose transitions from a structural stabilizer (ZnO/SiO_2) to electron-mobility facilitator (CMC–NGO–ZnO–ZnO_2) to mass-transfer enhancer (CTH–TN–CdS), positioning cellulose as a uniquely adaptive material capable of driving performance enhancements in diverse photocatalytic systems. Future work should prioritize the mechanistic mapping of the cellulose–photocatalyst interactions and controlled structural optimization to fully unlock the potential of cellulose in scalable environmental remediation technologies.

5.2.2 Sponges. Sponges are 3D, porous, and mechanically resilient architectures valued for their high surface area, low

density, and efficient fluid uptake-release dynamics, which collectively enable rapid mass transfer during photocatalytic reactions.[151] They are commonly fabricated using natural or synthetic polymers, and their interconnected microporous networks facilitate efficient photon penetration, reactant diffusion, and pollutant–catalyst interaction.[4,152] Among the natural sponge matrices, cellulose-based sponges stand out due to their biodegradability, abundant surface OH groups, and chemical tunability, enabling diverse functionalization strategies and nanoparticle anchoring.[153] These features make cellulose a privileged scaffold for designing next-generation photocatalytic platforms.

Liu *et al.* (2023) employed hydrothermally induced phase separation coupled with *in situ* synthesis nucleation to immobilize $NaBiS_2$ within chitosan/cellulose sponges. The resulting hierarchical macro-sponges had a size ranging from 150–1500 μm, and supported uniformly distributed $NaBiS_2$ nanoparticles with a size of 70–90 nm. The sponges exhibited a narrow band gap of 1.18 eV, high photocurrent density (0.74 μA cm^{-2}), and excellent mechanical compressibility. The combination of the hydrogen-bonded framework of cellulose with the functionality of chitosan enabled enhanced mechanical stability and efficient light harvesting. NaBiCCSs combine their high affinity for dyes with a synergistic adsorption–photocatalytic degradation process, achieving a methylene blue removal efficiency of 98.38% under visible light and showing excellent reusability.[30]

Similarly, You *et al.* (2022) fabricated ZnS nanoparticle-decorated cellulose–chitosan sponges *via* the hydrothermal decomposition of xanthates and *in situ* synthesis of ZnS nanoparticles. The sponges exhibited high porosity, very low bulk density, and uniform distribution of ZnS, while maintaining their structural integrity even after 80% severe compression fatigue cycles. The reduced band gap of the ZnS sponges (3.2–3.55 eV) relative to bulk ZnS arose from the quantum confinement effect due to its minimized agglomeration, an effect made possible by the cellulose scaffold preventing particle coalescence. This underscores the critical role of cellulose in stabilizing nanoscale photocatalysts. ZnCCSs exhibit a high Congo red removal efficiency of 96.53% and maintain excellent stability over multiple reusability cycles.[154]

In another example, self-supporting and floating photocatalytic cellulose sponges were engineered by anchoring BiOX nanosheets, aided by sodium alginate to improve the electrostatic attraction of Bi and O ions, which helps in promoting the nucleation of BiOX crystals. The hybrid sponges exhibited visible-light-active band gaps of 1.85 eV, and a hydrophobic water contact angle of 125°, owing to the ordered nanosheet alignment. Their buoyancy allowed enhanced light exposure and oxygen availability conditions that are unavailable in denser slurry catalysts. The hydrophobicity of the sponge places it in a transitional wetting state between the Wenzel and Cassie models, suggesting balanced interfacial properties suitable for aqueous-phase photocatalysis.[153] The low density and modifiable surface chemistry of cellulose were essential in achieving these functionalities. Assanvo *et al.* (2023) developed a low-cost, environmentally friendly, and biodegradable magnetic hybrid biosponge composite using collagen and kenaf fibre cellulose (KFCC) loaded with TiO_2 and Fe_3O_4. The hybrid sponges exhibited ferromagnetism (saturation magnetization = 8.6 emu g^{-1}), tunable mesoporosity (40 m^2 g^{-1}), surface area of 40 m^2 g^{-1} and pore volume (0.042 cm^3 g^{-1}). The as-prepared magnetic hybrid bio-sponge achieved a photocatalytic degradation efficiency of 91.2% for crystal violet under visible light and 86.6% under direct sunlight.[155] Recently, Xia *et al.* (2025) synthesized $ZnIn_2S_4$ nanoparticle-loaded cellulose/chitosan composite sponges *via in situ* hydrothermal phase separation. The $ZnIn_2S_4$ composite sponges displayed interconnected macropores of 150–500 μm, with uniformly distributed nanoparticles of 15 nm in size, a narrow band gap of 2.88 eV, and excellent compressibility. The abundant hydroxyl and amino groups on cellulose/chitosan facilitated dense nanoparticle anchoring and improved adsorption of pollutants, enabling a synergistic adsorption-photocatalyst performance. The prepared $ZnIn_2S_4$ composite sponge achieved a tetracycline removal efficiency of up to 91.5% under sunlight irradiation and retained its performance after eight consecutive cycles.[156]

In summary, cellulose-based photocatalytic sponges function as lightweight, microporous and chemically versatile platforms that uniquely support high nanoparticle dispersion, tunable band structures, and robust mechanical behavior. Across the surveyed systems, from $NaBiS_2$ to ZnS, BiOX, TiO_2–Fe_3O_4, and $ZnIn_2S_4$, the role of cellulose is consistently central, *i.e.*, it governs nanoparticle nucleation, minimizes agglomeration, enhances charge transfer interfaces, enabling floating or magnetically recoverable designs and provides abundant active sites for adsorption–photocatalysis coupling. These attributes highlight that cellulose is not merely a structural filler but acts as a functional co-component that significantly elevates the photocatalytic efficiency. Collectively, cellulose-engineered sponges represent a low-cost, sustainable, and highly adaptable class of photocatalysts with strong potential for large-scale environmental remediation.

5.2.3 Aerogels. Aerogels are highly porous, lightweight solid materials characterized by a low density and high surface area, porosity, and adsorption capacity.[157] These spongy-like structures are formed by replacing the liquid component of gels with gas, while preserving their solid network, which makes them suitable for environmental applications.[158] Aerogels ensure the rapid diffusion of pollutants and efficient interaction with active sites. For example, Amaly *et al.* (2022) reported the construction of a flexible and reusable metal-free aerogel composite composed of montmorillonite hosting methylene blue and microcrystalline cellulose (MCC). MCC served as the base for the construction of the aerogel, owing to its strength, water compatibility, and affordability. Additionally, montmorillonite was incorporated to support MB and enhance pollutant adsorption through an ion exchange process with Al^{3+}. The hydrogen bonds between MCC and montmorillonite helped to form a highly stable structure, and the freeze drying of hydrogels led to the formation of lightweight, porous aerogels. The surface area and density of the aerogel were 148 m^2 g^{-1} and 40 mg cm^{-3}, respectively. The MCC/MT-MB aerogel achieved 97% tetracycline removal within 120 min, owing to its MCC-derived 3D porous network, which enhanced pollutant adsorption, improved catalyst dispersion, and accelerated mass transfer throughout the photocatalytic process.[159]

Liu *et al.* (2025) developed GCN/reduced graphene oxide (rGO)/CNF aerogels through a facile bidirectional freeze drying and thermal reduction strategy. rGO acted both as a support and an electron transfer channel, helping to speed up electron–hole separation and transport. The dispersed CNFs supported the structure and likely improved the mechanical strength of the aerogel. The GCN/rGO/CNF aerogels exhibited a very low density of 6.45 mg cm^{-3} and layered structures with a spacing of 19 μm. Conversely, the aerogels prepared without CNF collapsed and lost their shape, showing that CNF helped to prevent the restacking of rGO/GCN and acted as a structural skeleton to enhance the strength. The carbon nitride/rGO/CNF aerogels exhibited superior compressibility and strength, retaining 96.1% height and 92.7% stress after 100 cycles, due to the strong interactions between rGO and the carbon nitride layers. The GCN/rGO/CNF aerogels had a specific surface area of 32.85 m^2 g^{-1} and a pore volume of 0.11 cm^3 g^{-1}, which increased with the carbon nitride content, reaching a maximum surface area of 66.63 m^2 g^{-1}. The GCN/rGO/CNF aerogels exhibited enhanced visible light absorption and suppressed recombination, which is ascribed to their 3D structure, promoting multiple light reflections.[113] Hexagonal nanocrystalline CdS was synthesized *via* a solvothermal method, loaded onto PEI-modified cellulose, and fabricated into

5492 | *J. Mater. Chem. A*, 2026, **14**, 5473–5519

This journal is © The Royal Society of Chemistry 2026

aerogels (PNFCA/CdS-2) through freeze drying. The resulting aerogel exhibited a staggered 3D network with uneven mesopores (2–50 nm), offering a high surface area, and abundant active sites conductive to the transport and adsorption of pollutants. Nitrogen adsorption–desorption isotherms confirmed their type IV behavior, indicating the presence of mesoporosity. The hybrid aerogels exhibited a higher surface area, enhancing their photocatalytic performance by increasing the number of redox-active sites and promoting visible light absorption. PNFCA/CdS-2 exhibited a reduced band gap of 1.9 eV from 2.17 eV (CdS), also facilitating efficient electron generation and transfer under visible light irradiation. Under the optimized conditions, the MO and MB removal efficiencies reached 99.56% and 100%, respectively.[160]

Zou et al. (2022) developed a sulfated lignocellulose nanofibril/TiO$_2$ (C-SLCNF–TNP) hybrid aerogel using a deep-eutectic-solvent-assisted extraction route, which introduced ionic groups and weakened the internal hydrogen bonding, enabling the formation of a highly porous, hydroxyl-rich 3D network. The resulting aerogel exhibited a high surface area (95 m^2 g^{-1}), elevated charge density (1.78 mmol g^{-1}), low swelling, and strong mechanical stability, providing an ideal scaffold for uniform TiO$_2$ anchoring through covalent and hydrogen-bond interactions. These cellulose–TiO$_2$ interfacial interactions reduced the band gap from 3.20 to 2.74 eV and enhanced charge separation by enabling the SLCNF matrix to act as an electron acceptor. The porous lignocellulosic framework delivered exceptional adsorption capacity toward tetracycline (70 mg g^{-1}), exceeding that of the cellulose-only and TiO$_2$-only controls, while the integrated adsorption–photocatalysis system achieved 94.9% removal.[161] However, although cellulose-based aerogels demonstrate impressive photocatalytic efficiencies owing to their high porosity, 3D mass-transfer pathways, and ease of functionalization, several key limitations remain unresolved. Most reported systems rely on optimized laboratory conditions, and their performance under realistic matrices, variable pH, or competing pollutants is largely untested. Moreover, differences in their fabrication routes including freeze-drying, solvothermal loading, and bidirectional freezing introduce challenges in reproducibility and scalability that are rarely quantified. Also, although band-gap tuning and heterojunction engineering improve their visible-light response, a mechanistic understanding of the charge migration within the cellulose framework is still limited. Overall, cellulose aerogels offer a compelling platform, but their practical deployment will require standardized benchmarking, long-term stability assessment, and scalable synthesis strategies.

5.2.4 Membranes. Cellulose-based photocatalytic membranes have emerged as highly versatile platforms for environmental remediation, combining sustainability, mechanical robustness, and excellent film-forming ability.[162] Unlike conventional polymeric supports, cellulose functions as an active functional matrix, whose abundant hydroxyl groups enable the strong anchoring of photocatalytic nanoparticles, facilitate surface modification, and regulate interfacial interactions. These properties enhance mass transfer, light

penetration, and pollutant adsorption, establishing cellulose as a key determinant of membrane performance.[163]

For example, Lu et al. (2021) fabricated a cellulose-based β-FeOOH@MIL-100(Fe)/polyvinyl pyrrolidone electrospun nanofiber membrane via electrospinning and in situ synthesis. Here, deacetylated cellulose acetate/polyvinyl pyrrolidone nanofibers serve as a flexible porous core, supporting a photocatalytically active sheath of β-FeOOH@MIL-100(Fe) heterojunctions. The high surface reactivity, tunable porosity, and abundant hydroxyl groups in cellulose enable the strong anchoring and uniform dispersion of catalysts. This core-sheath structured ENM features an ultrahigh catalyst loading (78 wt%), large surface area (1105 m^2 g^{-1}), and enhanced hydrophilicity, transitioning from a WCA of 133° to super hydrophilic (0°) after surface functionalization. The flexible biodegradable matrix ensured environmental safety, while the rough, hydrophilic surface architectures boost oil-water separation.[164] Similarly, cellulose-MIL-88A membranes were prepared via one-step deposition, highlighting cellulose-mediated MOF immobilization through hydrogen bonding and coordination interactions. The hydrophilicity of the membrane increased with an increase in the MIL-88A loading, as evidenced by a reduction in water contact angle from 86.2° to 4.8°, which facilitated water permeation and promoted efficient radical generation during photo-Fenton reaction (100% degradation). The fibrous morphology and hydrogen-bond network also provide mechanical flexibility and structural integrity, enabling repeated filtration–regeneration cycles. This underscores the dual role of cellulose of stabilizing the catalyst, while actively controlling the mass transport and catalytic efficiency.[165]

Mixed matrix membranes (MMMs) represent a promising class of composite materials that synergistically integrate the desirable properties of polymeric matrices with functional fillers, such as photocatalysts, to enhance their separation performance, stability, and functionality. Wu et al. (2020) constructed a mixed matrix membrane composed of carbon-sphere–TiO$_2$ as the core–shell and hydrophilic CNF via a simple vacuum filtration method. In the CNF membranes with embedded TiO$_2$–carbon spheres, the cellulose fibers create a porous, interwoven network, which ensures uniform particle dispersion, improved mesoporosity, and enhanced water permeability. These features make TiO$_2$@carbon spheres more effective for photocatalytic water treatment than their Pt/TiO$_2$ counterparts. In contrast, Pt/TiO$_2$ nanoparticles tend to aggregate, limiting light scattering and reducing the photocatalytic efficiency. Here, cellulose not only supports the filler physically but modulates the light penetration, mass transport, and antifouling properties, resulting in a superior water treatment performance compared to conventional polymeric MMMs. The presence of CNF in the membrane scatters light and modulates light penetration, impacting its photocatalytic activity, water permeability, and antifouling performance.[166] Rajeswari et al. (2017) reported the fabrication of a cellulose acetate-polyurethane membrane incorporated with ZnO nanoparticles using a blending technique. The SEM analysis revealed the uniform rod-like morphology of ZnO and pore formation on the membrane surface, indicating an asymmetric structure with

This journal is © The Royal Society of Chemistry 2026

J. Mater. Chem. A, 2026, 14, 5473–5519 | 5493

microcavities. AFM analysis showed that the incorporation of ZnO led to a smoother, more uniform surface with reduced surface roughness compared to the valley-like texture of the pristine CA-PU membrane. Thermal analysis demonstrated enhanced thermal stability in the ZnO-loaded membrane, with the maximum degradation shifting from 170 °C to 280 °C, which is attributed to solvent evaporation and water loss. The ZnO-blended CA–PU membrane exhibited enhanced water flux and superior photocatalytic degradation of Reactive Red 11 and Reactive Orange 84 dyes.[167]

Yin *et al.* (2022) developed a superhydrophobic cellulose membrane through the *in situ* deposition of MnO_2 micro/nanoparticles, followed by stearic acid (STA) modification. The membrane exhibited enhanced mechanical strength (+2.6%) and remarkable environmental durability, including its resistance to acids, alkali, high temperature, abrasion, and self-cleaning functionality. FESEM images confirmed that the MnO_2 nanoparticles were tightly anchored onto the cellulose microfibers, creating a multiscale rough architecture essential for superhydrophobicity. STA encapsulation further established a stacked, air–trapping interface. This synergistic roughness–chemistry combination yielded an ultrahigh water contact angle of 162° ± 2°. The structural analyses (XRD, FT-IR, and XPS) verified the incorporation of MnO_2 and reduced surface energy after STA coating. The superhydrophobic CM sample showed a strong photocatalytic performance, achieving over 98%

degradation of MB. The reactive hydroxyl groups, tunable porosity, and flexible fiber network rof cellulose enabled efficient nanoparticle immobilization and formation of hierarchical roughness.[168]

Across these systems, cellulose consistently acts as the primary performance regulator, where it dictates the dispersion, interfacial interactions, wettability, mass transfer, and structural stability of the catalyst. Although the choice of photocatalyst governs the chemical activity, cellulose determines how efficiently catalysts are deployed in practical membranes. Its hydroxyl-rich fiber network enables hydrogen-bonding and coordination interactions, modulates light scattering, and creates stable hydration layers, facilitating superior water permeability, pollutant accessibility, and recyclability. Compared to conventional polymeric supports, cellulose-based membranes integrate multifunctionality, structural resilience, and environmental compatibility, establishing cellulose as an indispensable component in next-generation photocatalytic membranes.

6. Applications of cellulose-supported photocatalysts

6.1 Energy

The extensive use of fossil fuels has enabled industrial and economic growth but has caused major environmental issues,
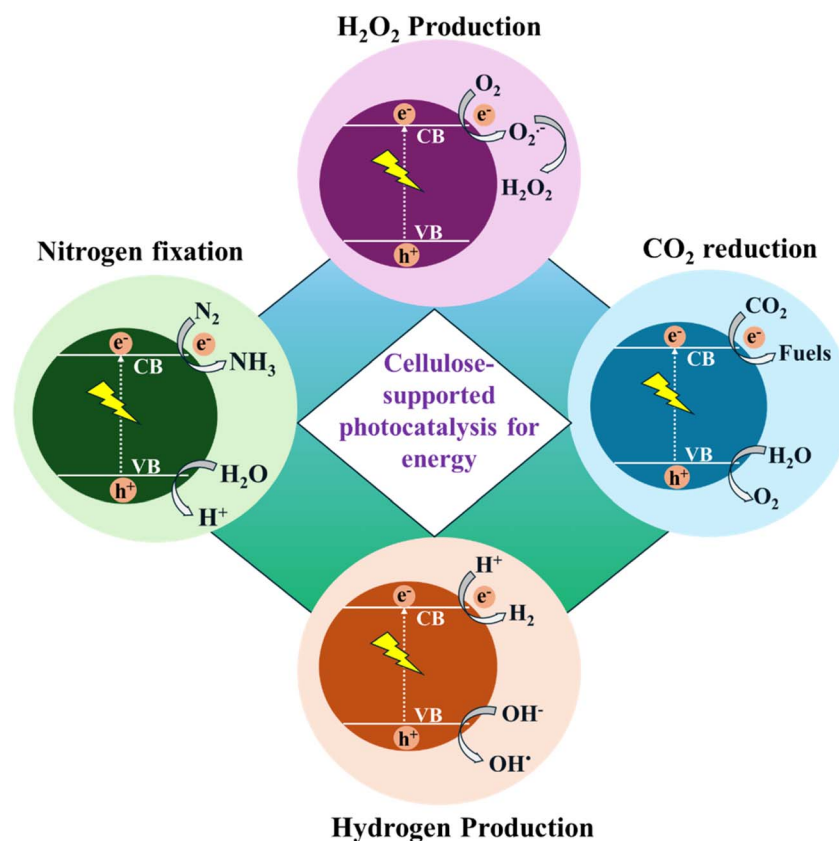

Fig. 8 Potential applications of cellulose-supported photocatalysts in energy remediation, including hydrogen, hydrogen peroxide, and ammonia production and carbon dioxide reduction.

including pollution, greenhouse gas emissions, and resource depletion,[169] which threaten the well-being of both humans and the ecology. As a result, global research is shifting toward clean, renewable energy options.[170] Solar energy, being abundant and sustainable, is especially attractive, and its conversion into fuels such as hydrogen provides a strong pathway toward energy security and reduced environmental impact.[46] In this context, cellulose-semiconductor photocatalysis has gained attention for the solar-driven production of hydrogen, H_2O_2, NH_3, and CO_2-derived value-added carbon products (Fig. 8). Photocatalysis operates by absorbing sunlight in a semiconductor with a suitable bandgap, producing electron–hole pairs. The excited electrons drive the reduction of H^+, O_2, N_2, or CO_2, while holes oxidize water or sacrificial agents to balance charge. The efficiency of these reactions relies on strong charge separation, proper band-edge alignment with redox potentials, and the effective adsorption and activation of reactants.

6.1.1 Hydrogen production. Photocatalysis harnesses sunlight to generate electron–hole pairs, which drive redox reactions, enabling the direct conversion of solar energy into chemical fuels. One of the most promising applications of this process is water splitting for sustainable hydrogen production. During the hydrogen evolution reaction (HER), photoexcited electrons reduce protons at the catalyst surface to generate hydrogen gas, while the corresponding holes oxidize water or a sacrificial agent.[171] This dual process prevents electron–hole recombination and maintains charge neutrality, ensuring continued photocatalytic activity.

Zhou et al. (2019) developed a 2D porous CdS nanosheet supported on bacterial cellulose (BC@CdS), which was synthesized via a bio-templating method. The BC scaffold provided structural control and enhanced photocatalytic performance under visible light, achieving an H_2 evolution rate of 928 μmol h^{-1} g^{-1} with reusability of five cycles. The enhanced performance arises from (i) the clean 2D CdS architecture, which increases light absorption, accelerates charge separation, and improves the redox ability, and (ii) tunable BC nano-windows, which promote efficient interfacial contact and mass diffusion. The FTIR analysis revealed strong interactions between the CdS nanocrystals and BC hydroxyl groups, as evidenced by broadening of the –OH peaks and shifts in the δC–H vibrations.[172] The hierarchical bi-nano-composite foam composed of $Zn_xCd_{1-x}S$ nanoparticles embedded within BC demonstrated higher visible light-driven H_2 production. The photocatalysts were synthesized via templated mineralization and ion exchange seeded growth. The optimized $Zn_{0.09}Cd_{0.91}S/BC$ composite achieved an impressive H_2 evolution rate of 1450 μmol h^{-1} g^{-1} with an apparent quantum efficiency of 12% at 420 nm. Among the $Zn_xCd_{1-x}S/BC$ samples, the highest photocatalytic activity was observed for $Zn_{0.09}Cd_{0.91}S/BC$, correlating with its large surface area, abundant surface defects (lowest PL intensity), and suitable band gap (2.33 eV). These features enhance electron–hole separation and provide more active sites for water-splitting H_2 evolution, with S^{2-} and SO_3^{2-} acting as hole scavengers, highlighting the integrated role of surface structure, defects, and crystallinity in boosting the photocatalytic performance.[173]

Chen et al. (2023) developed an edge-modified CN photocatalyst (CHC-CN5) by grafting cellulose-derived carbon species onto CN edges, where the cellulose component served as electron-attracting sites that promoted directional electron migration, enhanced charge separation, and reduced e^-–h^+ recombination. This modification also broadened the light absorption and improved carrier transport by lowering the resistivity, leading to a superior photocatalytic performance with a hydrogen evolution rate of 3436 μmol h^{-1} g^{-1} and 80.2% tetracycline degradation in 60 min, markedly outperforming pristine CN (Fig. 9ia and b).[174] CdS nanoparticles immobilized within porous regenerated cellulose films have been explored for hydrogen production under visible light. By adjusting the cellulose solution concentration, the mean pore size of the RC films was tuned from 57 to 20 nm with a simultaneous increment in CdS loading. The embedded CdS nanoparticles were well dispersed within the cellulose matrix, which enhanced their light absorption and improved their mechanical properties. The Pt-loaded CdS/RC film prepared from 4.5% cellulose solution exhibited a high H_2 evolution rate of 1.323 mmol h^{-1} g^{-1} (Fig. 9ic), which is attributed to efficient light harvesting, rapid charge transfer, and robust catalyst–electrolyte interaction.[175] In the CF/PDA/ZnS composite paper, cellulose fibers act as a robust, porous scaffold, which enhances its mechanical stability, provides a high surface area for uniform ZnS nanoparticle dispersion, and ensures the strong anchoring of the photocatalyst via PDA, preventing particle loss during repeated cycles. This structural support facilitates efficient contact between the reactants and active sites, while the ZnS/PDA type-II heterojunction on the cellulose surface promotes directional electron transfer, reduces electron–hole recombination, and boosts the photocatalytic redox activity. Consequently, the composite exhibits a superior hydrogen evolution rate (18 706 μmol h^{-1} g^{-1}), high apparent quantum yield (11.6%), and excellent durability (96% retention after three cycles) (Fig. 9id).[176]

The integration of cellulose with semiconductor photocatalysts presents a sustainable and versatile platform for hydrogen production (Table 5). Cellulose-supported photocatalysts demonstrate a dramatically improved performance over their non-cellulose counterparts. For example, porous CdS sheets anchored on cellulose achieved 928 μmol h^{-1} g^{-1} compared to 36 μmol h^{-1} g^{-1} for pristine CdS, and CHC-CN5 showed an increase from ~600 μmol h^{-1} g^{-1} to 3634 μmol h^{-1} g^{-1} under visible light. These enhancements highlight the role of cellulose in providing a high-surface-area scaffold, improving charge separation and facilitating reactant adsorption, resulting in both higher activity and sustained reusability. However, some limitations remain, including the relatively high cost and limited long-term stability of noble metal cocatalysts, as well as reduced efficiency under natural irradiation compared to simulated light. Addressing these issues is critical for practical deployment. Moving forward, several key perspectives can guide further research, as follows:

• Although several cellulose-based systems exhibit excellent lab-scale apparent quantum efficiencies, achieving high quantum efficiencies under natural sunlight remains

This journal is © The Royal Society of Chemistry 2026

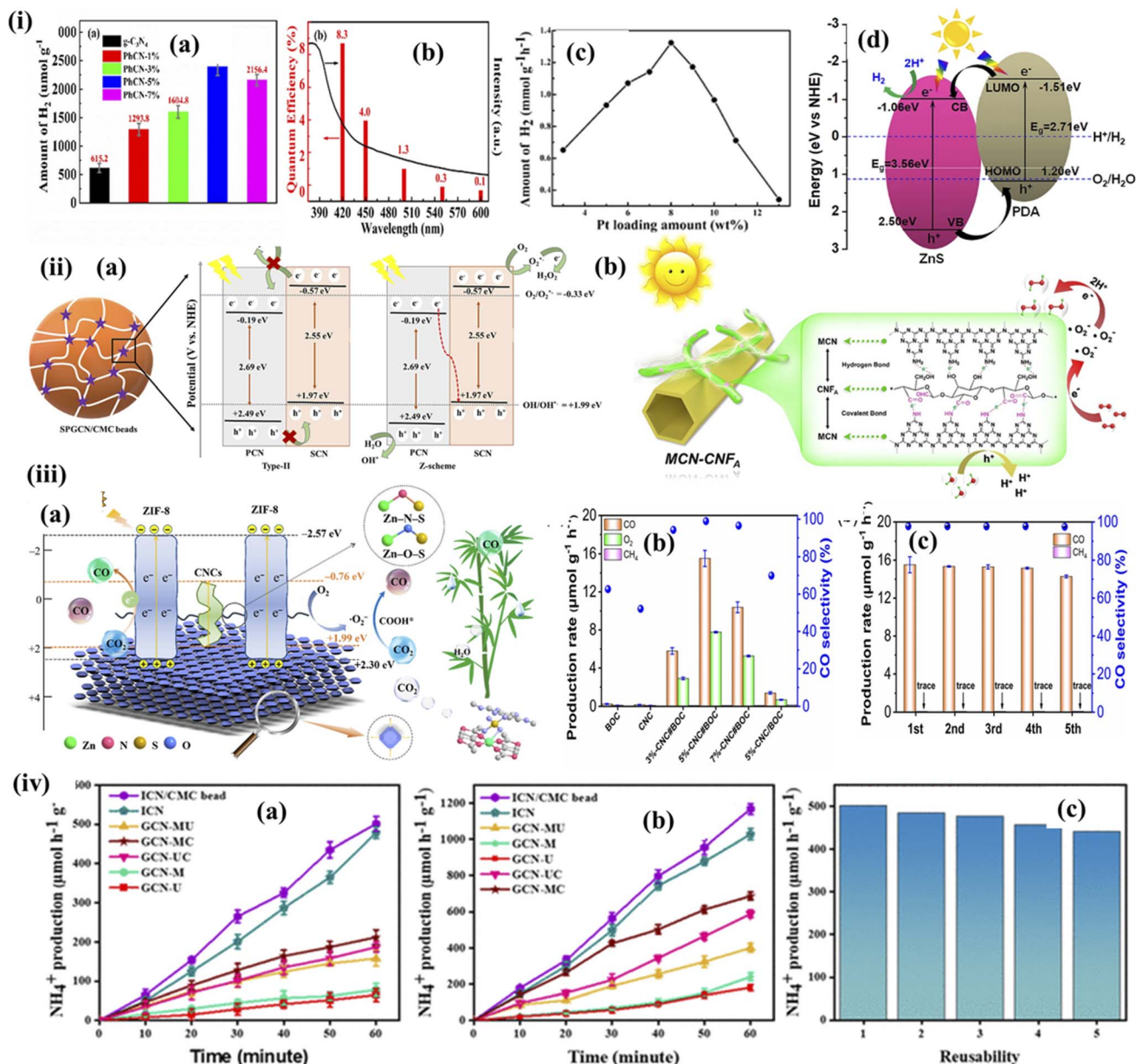J. Mater. Chem. A, 2026, 14, 5473–5519 | 5495

Fig. 9 (i) (a) Photocatalytic hydrogen evolution. (b) Reusability of CHC-CN5 photocatalyst. Reprinted with permission from ref. 174, the American Chemical Society (2023). (c) Influence of platinum-loading amount on photocatalytic hydrogen evolution rate using CdS/RC-4.5 films. Reprinted with permission from ref. 175, the American Chemical Society (2009). (d) Band structures of ZnS and PDA charge transfer pathway in ZnS/PDA heterojunction. Reprinted with permission from ref. 176, Springer (2024). (ii) (a) Proposed Z-scheme heterojunction mechanism for H_2O_2 production using SPGCN/CMC beads. Reprinted with permission from ref. 36, Elsevier (2024). (b) Mechanism of photocatalytic H_2O_2 production using MCN-CNF$_A$. Reprinted with permission from ref. 177, Elsevier (2024). (iii) (a) Mechanism of photocatalytic CO_2 reduction using CNC@ZIF-8 3D network. Reprinted with permission from ref. 144, Elsevier (2024) (b) photocatalytic CO_2 reduction performance of CNC@BOC. (c) Recovery experiments using the 5% CNC@BOC sample. Reprinted with permission from ref. 178, Elsevier (2024). (iv) Photocatalytic nitrogen fixation efficacy of ICN/CMC beads (a) using water and (b) using sacrificial agents. (c) Reusability of ICN/CMC beads towards nitrogen fixation. Reprinted with permission from ref. 179, the American Chemical Society (2024).

a challenge. Future research should focus on band gap engineering and heterojunction design to broaden light absorption across the visible and near infrared regions.

- The development of cellulose-based photocatalytic papers, foam, and hydrogels will support device-level scalability. These systems enable floating, solid–gas biphasic configurations, which not only reduce mass transfer limitations but also show

great potential for outdoor hydrogen production from humid air or solar steam.

- Cellulose-based photocatalysts could be integrated into photoelectrochemical systems, serving as flexible, porous photocatalytic layers that facilitate gas evolution and electrolyte diffusion, enhancing the overall efficacy of the system.

5496 | J. Mater. Chem. A, 2026, 14, 5473–5519

This journal is © The Royal Society of Chemistry 2026

Table 5 Summary of different catalysts used for hydrogen production *via* photocatalysis

Catalyst system	Light source	Non-cellulose benchmark performance	Cellulose-supported photocatalyst performance	Reusability	Reference
Porous CdS sheets	300 W Xe lamp	CdS: 36 $\mu mol\ h^{-1}\ g^{-1}$	928 $\mu mol\ h^{-1}\ g^{-1}$	4	172
CHC-CN5	Visible lamp	CN: 600 $\mu mol\ h^{-1}\ g^{-1}$	3634 $\mu mol\ h^{-1}\ g^{-1}$	4	174
Pt–CdS/regenerated cellulose film	250 W Xe	CdS film: 0.652 $mmol\ g^{-1}\ h^{-1}$	1.323 $mmol\ g^{-1}\ h^{-1}$	3	175
CF/PDA/ZnS composite	300 W Xe lamp	CF/ZnS: 5805 $\mu mol\ h^{-1}\ g^{-1}$	18 706.8 $\mu mol\ h^{-1}\ g^{-1}$	3	176
Cu/Ni–TiO$_2$ cellulose	UV LED lamp	TiO$_2$: 125 $\mu mol\ h^{-1}\ g^{-1}$	489 $\mu mol\ h^{-1}\ g^{-1}$	—	180

6.1.2 Hydrogen peroxide production. Hydrogen peroxide (H_2O_2) has garnered significant attention as a green oxidant due to its high active oxygen content, environmentally benign byproducts, and broad applicability in the medical, chemical, energy, and environmental sectors.[181] However, its conventional production methods, such as the anthraquinone process, are energy-intensive and environmentally burdensome, while its direct synthesis from hydrogen and oxygen involves safety and scalability challenges.[15] In this context, the photocatalytic production of H_2O_2 using solar energy offers a sustainable, safe, and decentralized alternative.[170] Cellulose-supported photocatalysts have shown great promise, leveraging the structural tunability and functional diversity of cellulose to enhance light absorption, charge transfer, and oxygen activation for efficient H_2O_2 generation.[36,72] In H_2O_2 production, the CB electrons reduce molecular oxygen (O_2) *via* a two-electron pathway to form H_2O_2, rather than the four-electron pathway to water. This selectivity is favored by appropriate tuning of the band positions and surface sites in the catalyst. Concurrently, the holes oxidize water or organic donors to regenerate the catalyst surface.[36,182]

Highly efficient GCN/carboxylated cellulose nanofibers (CNF) were developed by rationally extending the hydrogen bond/π-bond intermolecular networks between GCN and carboxylated CNF and polydopamine to enhance solar-driven peroxide synthesis. This photocatalyst exhibited a remarkable H_2O_2 generation rate of 130 $\mu mol\ L^{-1}\ h^{-1}$, significantly surpassing that of pure GCN. This improvement was attributed to the enhanced interaction between GCN and carboxylated CNF through hydrogen bonding and π–π stacking, which facilitated superior oxygen adsorption, accelerated charge carrier separation, and efficient charge transfer. *In situ* FT-IR spectroscopy showed bands at 1156, 1278, and 1362 cm^{-1}, which corresponded to $\cdot O_2^-$, O–O stretching of surface-adsorbed $\cdot OOH$, and bending mode of $\cdot HOOH$, respectively, confirming H_2O_2 formation *via* an $\cdot O_2^-$ intermediate pathway. The bands at 1103 and 1434 cm^{-1}, attributed to C–OH and C–O bonds, respectively, indicated the presence of OH species, a key intermediate in this process. The theoretical calculations and experimental data confirm that the introduction of CNF enhances O_2 adsorption and separation and transfer of photogenerated charge carriers.[66] Balakrishnan *et al.* (2024) synthesized a homojunction through a simple wet impregnation method, comprising phosphorylated and sulfur-self-doped

g-C_3N_4 (SPGCN). Subsequently, this homojunction system was integrated into hydrogel beads using CMC through a cross-linking reaction, resulting in the formation of SPGCN/CMC beads. The photocatalytic studies demonstrated a notable H_2O_2 production of 3.5 mM after 60 min with a reusability of 10 cycles. The higher catalytic activity is attributed to the improved visible light absorption through proper tuning of the band gap, which ensures the utilization of light in a broader spectrum. The suppression of electron–hole pairs is achieved through the construction of a Z-scheme between phosphorylated and sulfur-self-doped g-C_3N_4 (Fig. 9iia). The mechanistic studies also indicated that superoxide radicals were involved in the generation of H_2O_2, with the reaction following a selective two-electron reduction pathway.[36]

In another study, hydrothermal carbonaceous carbon (HCC) was assessed for H_2O_2 production due to its semiconductor properties, despite its slower charge carrier separation and energy utilization. Thus, pyrrole-doped HCC (PHCC) was prepared using cellulose from balsa wood and pyrrole. The resulting π-conjugated structure, formed by the stacking of electron-donor furan units and acceptor pyrrole units, reduces the band gap, enhances light absorption and accelerates charge transfer, while reducing its particle size to expose more active sites. PHCC achieved an impressive H_2O_2 production of 1.4 mM under simulated sunlight, which is 3.8-times higher than the pyrrole-free catalyst. This enhancement is ascribed to the improved energy utilization, faster oxygen reduction kinetics, and a photothermal-assisted effect. Theoretical calculations showed that furan-pyrrole-alternating structures may optimize the energy levels, improve the charge separation efficacy and enhance oxygen adsorption/activation, driving an increase in photocatalytic H_2O_2 synthesis.[183] Zhou *et al.* (2024) proposed the anchoring of aldehyde-functionalized cellulose nanofibers onto GCN microtubes through covalent and hydrogen bonding. The grafting of functionalized nanofibers onto GCN microtubes is achieved *via* amide bonding between the aldehyde groups of the nanofiber and amino groups at the edge of the GCN microtube heptazine ring. Their incorporation significantly improved the wettability of GCN, promoting the adsorption of oxygen. The experimental results and DFT calculations revealed that the firm surface interfacial interactions boosted the electron transfer, facilitating an efficient single-electron oxygen reduction reaction for H_2O_2 production of 67.44 $\mu mol\ L^{-1}$. As highlighted in Fig. 9iib, under visible light illumination,

This journal is © The Royal Society of Chemistry 2026

J. Mater. Chem. A, 2026, **14**, 5473–5519 | **5497**

Table 6 Summary of different photocatalysts employed for hydrogen peroxide production

Catalyst	Light source	Non-cellulose benchmark performance	Cellulose-supported photocatalyst performance	Reusability	Pathway	Reference
KOH-activated bagasse cellulose carbon aerogel ZnO composite	300 W Xe lamp	NA	96.39 mmol L^{-1}	5	Two-step-two-electron oxygen reduction	184
Spent coffee ground-derived biochar	300 W Xe lamp	Hydrochar: 0.341 mmol L^{-1}	0.61 mmol L^{-1}	5	One-electron reduction oxygen reaction	185
Aldehyde cellulose nanofibers/GCN	300 W Xe lamp	CN: 0.01679 mmol L^{-1}	67 μmol L^{-1}	—	Two-step-two-electron oxygen reduction	177
Furan-resin-structured hydrothermal carbon	300× white LED light	—	480 μmol L^{-1}	6	Two-step-two-electron oxygen reduction	186
GCN homojunction with nanofibrous carbon	300 W Xe lamp	GCN: 27.5 μmol L^{-1}	136.9 μmol L^{-1}	—	Two-step-two-electron oxygen reduction	187
Hydrothermal carbonaceous carbon	300 W Xe lamp	NA	1.16 mmol h^{-1} g^{-1}	—	Two-step-two-electron oxygen reduction	188
Metal-free catalyst from cellulose	Visible	NA	2.09 mmol h^{-1} g^{-1}	—	Two-step-two-electron oxygen reduction	189
Defect-rich and dimensionally confined double functionalized GCN homojunction hydrogel	250 W medium-pressure Hg lamp	GCN: 0.075 mmol h^{-1} g^{-1}	1.05 mmol h^{-1} g^{-1}	6	Two-step-two-electron oxygen reduction	93
In$_2$S$_3$/Bi$_2$WO$_6$/CdS hydrogel	250 W medium-pressure Hg lamp	GCN: <100 μmol L^{-1}	302 μmol L^{-1}	5	Two-step-two-electron oxygen reduction	190
Ternary carbon nitride homojunction hydrogels	250 W medium-pressure Hg lamp	Bi$_2$WO$_6$: 125 μM	1204 μmol L^{-1}	5	Two-step-two-electron oxygen reduction	56

photoexcited electrons migrate to the aldehyde-functionalized CNF, facilitating H$_2$O$_2$ generation *via* a two-step single-electron oxygen reduction pathway.[177]

Cellulose-supported photocatalysts have emerged as up-and-coming platforms for the sustainable and efficient production of H$_2$O$_2$ (Table 6), owing to their abundant functional groups, high surface area, and excellent structural tunability. For instance, the activity of g-C$_3$N$_4$ homojunctions with nanofibrous carbon reached 136.9 μmol L^{-1} *versus* 27.5 μmol L^{-1} for pristine GCN, and metal-free cellulose-derived catalysts achieved 2.09 mmol h^{-1} g^{-1}, highlighting the benefits of cellulose in improving the charge separation, surface area, and active site accessibility. Predominantly, cellulose and its derivatives such as carboxylated, sulfonated, phosphorylated, and aldehyde-functionalized nanofibers have been integrated with carbon nitride frameworks to form highly active photocatalytic systems. These composites exploit hydrogen bonding, π–π interactions, and covalent linkages to improve the adsorption of oxygen and facilitate selective two-electron-oxygen reduction pathways for H$_2$O$_2$ synthesis. However, the future development of cellulose-supported photocatalysts should focus on several key directions, including: (i) rational engineering of cellulose through targeted functional group modification, which can further tune its electronic interactions and catalytic interfaces. Simultaneously, non-metal heteroatom doping and utilization of carbon substrates can modulate band structures and

facilitate interfacial charge transfer dynamics. (ii) The utilization of *in situ* spectroscopic techniques such as Fourier transform infrared spectroscopy (FTIR) and electron paramagnetic resonance (EPR) combined with density functional theory (DFT) simulations will be crucial to unravel the reaction intermediates, charge migration pathways, and active site structures, thereby enabling more predictive catalyst design. (iii) To transition this system toward industrial relevance, comprehensive life-cycle assessments and techno-economic analyses must be conducted to evaluate the sustainability and cost-effectiveness of cellulose-based photocatalysts with respect to conventional production strategies.

6.1.3 Carbon dioxide reduction. The accelerating pace of scientific and technological development has intensified the global energy consumption, deepening the reliance on fossil fuels and elevating CO$_2$ emissions, with atmospheric its concentrations projected to rise from 400 to 750 ppm. Given that the global energy demand is expected to increase by 28% by 2040, the need for sustainable and eco-friendly strategies for clean energy generation and carbon mitigation has become urgent.[191] Photocatalytic CO$_2$ reduction offers a promising pathway by using water as an electron donor to convert CO$_2$ into value-added fuels such as CO, CH$_4$, CH$_3$OH, and formic acid.[192,193] Integrating cellulose-based materials as supports or templates has recently gained traction, as they enhance the photocatalytic performance of materials by improving their

5498 | *J. Mater. Chem. A*, 2026, **14**, 5473–5519

This journal is © The Royal Society of Chemistry 2026

charge separation, increasing their active surface area, and strengthening CO_2 adsorption.

Shi et al. (2022) demonstrated that cellulose fibers (30–50 μm) serve as effective templates for synthesizing 3D CuO–ZnO (CuO–ZnOCel-T) and Cu–ZnO (Cu–ZnOCel-T) nanocomposites for solar-driven CO_2 conversion. The abundant hydroxyl groups and fibriform structure of cellulose facilitated the uniform dispersion of the nanoparticles and prevented their aggregation, unlike carbon fiber-supported or template-free CuO–ZnO, which suffered from severe clustering and lower catalytic activity. CuO–ZnOCel-T achieved a CO production rate of 8.61 $\mu mol\ g^{-1}\ h^{-1}$ (99.8% selectivity), outperforming CuO–ZnOC-T (4.10 $\mu mol\ g^{-1}\ h^{-1}$) and bare CuO–ZnO powder (0.84 $\mu mol\ g^{-1}\ h^{-1}$). Remarkably, the incorporation of metallic Cu^0 via wheat-straw reduction in Cu–ZnOCel-T increased the CO production rate to 30.17 $\mu mol\ g^{-1}\ h^{-1}$, highlighting the synergistic effect of surface plasmon resonance (SPR) and enhanced charge separation. Structural and spectroscopic analyses (HRTEM, XRD, XPS, PL, and EIS) confirmed the high dispersion of nanoparticles, presence of oxygen defects, and efficient electron–hole separation, while photocurrent measurements validated the improved carrier transfer. Optimizing the Cu/Zn ratio (1 : 4) further enhanced the activity, and the catalyst maintained 87% of its performance over six cycles, demonstrating its excellent stability.[194]

Aminated cellulose nanocrystals (NCC-EDA) serve as an effective multifunctional support for TiO_2, enhancing its crystallinity, charge separation, and CO_2 adsorption. XRD and TG analyses confirm that NCC-EDA promotes the formation of high-crystallinity anatase TiO_2, while TEM shows that the NCC-EDA coating reduces the particle size of TiO_2 (~20 nm) and prevents crystal overgrowth. Surface characterization (EDX, XPS, FTIR, and Raman spectroscopy) demonstrates the strong interaction between amino groups and TiO_2, with graphitized cellulose structures analogous to graphene, facilitating electron transfer and suppressing e^-–h^+ recombination. The TiO_2/NCC-EDA composite exhibits a reduced band gap (2.86 eV vs. 3.17 eV for TiO_2), extended visible-light absorption, increased BET surface area (174 $m^2\ g^{-1}$ vs. 43 $m^2\ g^{-1}$), and enhanced CO_2 adsorption. Photocurrent, PL, and EIS studies confirm that NCC-EDA accelerates charge separation and maintains sustained electron availability under illumination. As a result, the reduction of CO_2 to $HCOOCH_3$ is 4.5-times higher than that by pure TiO_2 (372.85 $\mu mol\ g^{-1}$ in 6 h), with optimal activity at 54 g L^{-1} NCC-EDA. Mechanistically, NCC-EDA acts as an electron mediator and structural stabilizer, enabling efficient CO_2 activation and conversion, while minimizing electron–hole recombination. Overall, cellulose in TiO_2/NCC-EDA functions as a structural scaffold, electronic promoter, and surface modifier, demonstrating a clear advantage over non-cellulose-supported TiO_2 for visible-light-driven CO_2 photocatalysis.[195]

Cellulose nanocrystals derived from low-cost bamboo were used to develop a topologically chiral cellulose nanocrystal (CNC)@ZIF-8 3D network via Zn–N–S and Zn–O–S bond formation. This unique architecture not only enhances electron transport and reduces electron–hole recombination in ZIF-8 but also facilitates charge accumulation due to the larger bond angle and stronger electron-withdrawing nature of the Zn–O–S linkage. The CNC@ZIF-8 photocatalyst achieved a CO yield of 301.16 $\mu mol\ g^{-1}$, which is 9.43-times higher than that of pure ZIF-8. A higher content of CNC leads to greater optical rotation and UV sensitivity, showing a positive correlation between catalytic activity and topological chirality. The mechanistic studies (Fig. 9iiia) revealed that the photogenerated electrons transferred to CNCs participate in forming superoxide radicals ($^•O_2^-$), which further enhance the CO_2 reduction process. In the 3D chiral network of CNCs@ZIF-8, the adsorbed CO_2 molecules react with electrons and protons to form the COOH$^•$ intermediate, which subsequently undergoes protonation to yield CO.[144]

In summary, novel cellulose-based hybrid composites (CNC@BOC) were synthesized via an innovative interfacial bonding strategy, demonstrating remarkable and consistent activity for CO_2 photoreduction under blue LED light, achieving a CO production rate of 15.22 $\mu mol\ g^{-1}\ h^{-1}$ with 97% selectivity (Fig. 9iiib and c). Theoretical calculations and experimental studies revealed that the hydroxyl groups on CNC interact with the surface Bi ions of $Bi_2O_2CO_3$ (BOC), forming robust Bi–O–C covalent bonds. These interfacial bonds play multiple key roles in the catalytic system. First, the newly formed metal coordination polymer acts as a photosensitizer via ligand-to-metal charge transfer (LMCT), enhancing visible-light absorption and increasing the affinity of the catalyst toward CO_2 molecules. Second, the covalent linkage facilitates rapid electron transfer from BOC to CNC, generating highly oxidized Bi species and stabilizing the oxygen vacancies (OVs) on the BOC surface, which are essential for CO_2 activation. Third, the integration of CNC and BOC establishes a type II heterostructure, which promotes the efficient separation of photoinduced charge carriers, reduces electron–hole recombination, and enables the facile formation of the key *COOH intermediate. Additionally, the covalent bonding, LMCT effect, and stabilized OVs collectively contribute to a narrowed bandgap, higher reactant adsorption, and accelerated charge transport pathways. These synergistic effects improve both the photocatalytic activity and selectivity toward CO formation.[178]

The incorporation of cellulose and its derivatives as templates or supports in photocatalytic systems has emerged as a sustainable and versatile strategy to enhance their CO_2 reduction performance (Table 7). Cellulose offers unique structural and chemical advantages, including high surface area, tunable functional groups, polar surfaces for CO_2 adsorption, and three-dimensional or chiral architectures, which collectively promote light harvesting, charge separation, and electron transfer. These features facilitate strong interactions between CO_2 molecules and the catalytic surface, improving their adsorption, activation, and conversion efficiency. For instance, TiO_2 supported on aminated cellulose nanocrystals (NCC-EDA) achieves a CO_2 reduction rate of 372.85 $\mu mol\ g^{-1}$ in 6 h, which is nearly seven-times higher than the benchmark TiO_2 system (54 $\mu mol\ g^{-1}\ cat^{-1}$). Mechanistic studies indicate that covalent interfacial bonding between cellulose and the photocatalyst induces ligand-to-metal charge transfer (LMCT), narrows the bandgap, and generates highly reactive sites such as oxygen vacancies, thereby facilitating CO_2

This journal is © The Royal Society of Chemistry 2026

J. Mater. Chem. A, 2026, 14, 5473–5519 | 5499

Table 7 Summary of different photocatalysts employed for CO_2 reduction

Catalyst system	Light source	Non-cellulose benchmark performance	Cellulose-supported photocatalyst performance	Products	Reusability	Reference
TiO_2/nanocellulose crystals-EDA	300 W Xe lamp	NCC-EDA: 54 μmol g^{-1} cat^{-1}	372.85 μmol g^{-1} cat^{-1}	CH_3OH, $HCOOCH_3$, $HCOOC_2H_5$, C_2H_5OH, and CH_2Cl_2	3	195
Cellulose nanocrystal-bonded $Bi_2O_2CO_3$	3 W blue LED lamp	$Bi_2O_2CO_3$: 0.26 μmol g^{-1} h^{-1}	15.22 μmol g^{-1} h^{-1} (CO)	CO, CH_4 and O_2	5	178
Cu-modified GCN nanorod bundles	300 W Xe lamp	g-C_3N_4: 4.16 μmol g^{-1} h^{-1}	49.57 μmol g^{-1} h^{-1} (CO)	CO and CH_4	5	196
Cellulose nanocrystal ZIF-8 3D network aerogel	300 W Xe lamp	ZIF-8: 31.94 μmol g^{-1}	136.37 μmol g^{-1} (CO)	CO	—	144

activation and *COOH intermediate formation. However, despite these advantages, several critical aspects remain underexplored, where surface functionalization *via* amination, oxidation, or other modifications could further improve the CO_2 adsorption and reactivity, but optimized protocols and their effects on electron transfer and reduction kinetics are not yet fully established. Similarly, the interactions of CO_2 with cellulose-supported reaction pathways need to be revealed.

6.1.4 Nitrogen fixation. Ammonia is a key industrial feedstock widely used in the production of fertilizers and chemicals.[197] However, its conventional synthesis through the Haber–Bosch process is energy-intensive and emits tons of carbon dioxide into the environment.[198] As the demand for cleaner technologies grows, photocatalytic nitrogen fixation has emerged as a promising green alternative, utilizing solar energy to convert atmospheric nitrogen into ammonia under mild conditions using water as a proton source.[199] Wang *et al.* (2024) utilized cellulose as a sacrificial reagent for photocatalytic nitrogen fixation using oxygen-vacancy modified MoO_3 nanosheets. The MoO_3 samples exhibited photocatalytic activity for ammonia production using CH_3OH as a sacrificial agent, as confirmed by the Nessler's reagent method. The activity of the catalyst is closely associated with surface oxygen vacancies. Upon the utilization of cellulose as an electron donor, MoO_3-400 showed the highest NH_3 production (146 μmol h^{-1} g^{-1}). However, its overall activity was lower than in the methanol system, likely due to the weaker reducing ability and limited charge-transfer pathways of cellulose. The oxidation of cellulose was primarily driven by the hydroxyl radicals generated by holes.[200]

Balakrishnan *et al.* (2024) demonstrated that carboxymethyl cellulose (CMC), a cellulose derivative, plays a critical role in constructing citric acid-functionalized carbon nitride homo-junction (ICN)/CMC hydrogel beads *via* a simple $FeCl_3$-assisted crosslinking strategy. The abundant hydroxyl and carboxyl groups of CMC facilitated strong hydrogen bonding and electrostatic interactions with ICN, ensuring the uniform immobilization of ICN, enhanced water retention, and a higher surface area for nitrogen adsorption. This structural synergy significantly improved the visible-light absorption, charge separation,

and electron transfer, leading to efficient photocatalytic nitrogen fixation. Under visible-light irradiation with distilled water as the proton source, the ICN/CMC beads achieved the maximum ammonia yield of 501 μmol h^{-1} g^{-1}, which increased to 1168 μmol h^{-1} g^{-1} when methanol was used as a sacrificial agent, highlighting a more than twofold enhancement due to the sacrificial donor. For comparison, pristine g-C_3N_4 exhibited a much lower yield of 65 μmol h^{-1} g^{-1}, emphasizing the significant enhancement imparted by the ICN/CMC hybrid structure. In contrast, ICN without CMC exhibited lower activity and less effective charge separation, confirming that CMC not only acts as a structural scaffold but also contributes actively to the photocatalytic performance by facilitating proton transport and increasing the number of adsorption sites. Mechanistic studies revealed that the photoinduced electrons are efficiently transferred to adsorbed nitrogen molecules, reducing them to ammonium ions, while holes are effectively consumed, demonstrating that the CMC matrix enhances both the stability and activity of the photocatalyst. These results underscore the dual role of CMC as both a structural support and an electronic facilitator, providing a renewable, green scaffold that markedly improves the nitrogen fixation efficiency.[179]

In photocatalytic systems coupling nitrogen fixation with glucose conversion, cellulose serves as a critical substrate that is first enzymatically saccharified to glucose, which then donates electrons and protons during the photocatalytic reaction. The FIS/Fe-Pal composite, with an Fe-Pal to $FeIn_2S_4$ mass ratio of 0.4 : 1, achieved the highest ammonia production of 583 μmol g^{-1} after 6 h of visible-light irradiation, surpassing $FeIn_2S_4$ (100 μmol g^{-1}). The cellulose-derived glucose acts as a sacrificial electron donor, facilitating rapid photogenerated charge separation in the S-scheme heterojunction between Fe-Pal and $FeIn_2S_4$. Sulfur vacancies and Fe ions on the surface of FIS/Fe-Pal provide dual active sites for N_2 adsorption and activation, while the electrons derived from glucose oxidation reduce N_2 to NH_4^+. In comparison, in the absence of glucose, the same catalyst exhibited a lower ammonia yield (314 μmol g^{-1}), underscoring the essential role of cellulose in enhancing photocatalytic nitrogen fixation. This highlights that cellulose not only participates as a renewable sacrificial substrate but also

5500 | *J. Mater. Chem. A*, 2026, **14**, 5473–5519

This journal is © The Royal Society of Chemistry 2026

improves the electron transfer efficiency, thereby boosting NH_4^+ production in the coupled reaction system.[201]

Among the reported nitrogen fixation systems, cellulose-supported catalysts consistently outperform their non-cellulose counterparts, exhibiting higher ammonia yields, improved charge separation, and enhanced stability. This highlights the dual role of cellulose as both a structural scaffold and an electron/proton mediator, which is absent in conventional catalysts. However, challenges such as limited light absorption, catalyst stability, and scalability need to be addressed to advance its practical applications, as follows: (i) the utilization of sustainable electron donors like cellulose and lignin derivatives offers eco-friendly alternatives to methanol or ethanol. (ii) Translating laboratory-scale findings into real-world applications requires the development of scalable, continuous flow photoreactor systems with optimized light distribution and solar tracking technologies. (iii) Deeper mechanistic understanding using isotope labelling studies and DFT-based computational studies can elucidate reaction pathways, catalyst design, and enhance the selectivity towards ammonia over by-products.

A systematic strengths, weaknesses, opportunities, and threats (SWOT) analysis was conducted to provide a comparative evaluation of four major photocatalytic conversion processes: hydrogen production, hydrogen peroxide evolution, nitrogen fixation, and carbon dioxide reduction. Fig. 10 presents the SWOT analysis of cellulose-supported photocatalysts for photocatalytic energy production. These solar-driven pathways are integral for the development of carbon-neutral energy systems and sustainable chemical manufacturing. Photocatalytic hydrogen production is relatively well-developed and benefits from its high energy density and clean combustion characteristics. Hydrogen peroxide synthesis offers a green alternative to the traditional anthraquinone process, operating under ambient conditions using water and oxygen as primary inputs. Photocatalytic nitrogen fixation, though less mature, holds promise as an energy-efficient and decentralized approach for ammonia production. Carbon dioxide reduction facilitates the conversion of greenhouse gases into valuable chemicals and fuels, aligning with the principles of a circular economy. The strengths of cellulose-supported photocatalytic systems include sustainability, mild operating conditions, and the ability to convert abundant, low-cost feedstocks into useful fuels. Their weaknesses include charge recombination losses and poor material durability. Opportunities lie in the development of advanced cellulose-based composites and the integration of this technology into decentralized energy systems. Threats include competition from established energy technologies and the requirement for cost-effective, scalable production methods. Overall, continued research and innovation are essential to fully realize the potential of cellulose-supported photocatalysts in sustainable fuel generation.

6.2 Wastewater remediation

With the significant advancements in industrialization, the environmental repercussions of human activities have become increasingly severe, raising widespread concern.[8,202] One of the most critical challenges is the protection of water resources,

H₂ Production	H₂O₂ Production	NH₃ Production	CO₂ Reduction
Strength			
• High energy density fuel • Established mechanisms • Scalable systems like cellulose foams, papers and hydrogels	• Green alternative to anthraquinone process • Dual oxidant-electron acceptor role • Mild experimental conditions	• Sustainable alternative to Haber-Bosch Process • Can integrate solar and biomass inputs	• CO₂ mitigation and fuel generation • Selective product tuning via tailored photocatalysts
Weakness			
• Dependence on noble metal cocatalysts • Photostability issues under prolonged irradiation	• Low selectivity and limited yield • Competes with oxygen evolution in water	• Nitrogen activation is thermodynamically difficult • Low ammonia yield and poor selectivity	• Multiple-electron transfer complexity • Poor selectivity for desired products such as CH₃OH, CH₄
Opportunities			
• Integration with circular bioeconomy • Floating solar steam systems with humid air	• Coupled disinfection and oxidation • Direct water-to-H₂O₂ production from O₂ under optimal conditions	• Development of bi-functional catalysts (N₂ fixation and H₂ evolution) • Renewable nitrogen-source utilization	• Direct air capture and reduction systems • CO₂-to-fuel hybrid photo-electrochemical reactions
Threats			
• Water scarcity and purity requirements • Challenges in large-scale deployment	• Photocatalyst instability under sunlight • H₂O₂ accumulation and safety constraints	• Competition with Haber-Bosch in terms of cost and scale • Catalyst poisoning and deactivation risks	• Economic viability of large scale implementations • Competition with CCS and fossil-fuel-derived products

Fig. 10 SWOT analysis of cellulose-supported photocatalysts for energy applications.

This journal is © The Royal Society of Chemistry 2026
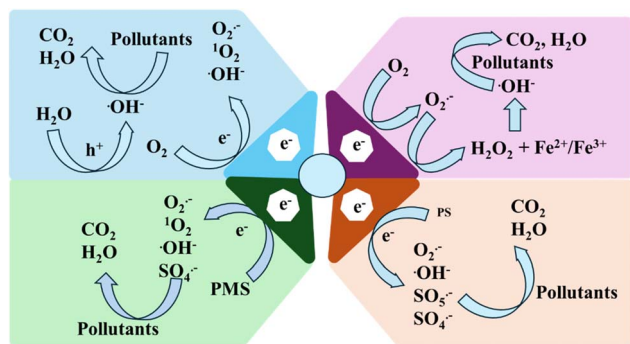
J. Mater. Chem. A, 2026, 14, 5473–5519 | 5501

Fig. 11 Generalized wastewater degradation mechanisms using cellulose-supported photocatalysts.

which has become a focal point in environmental research. Water pollutants typically include heavy metals, pharmaceuticals, dyes, and pesticides.[203] Among the different methods, solar-driven photocatalysis stands out as a clean and sustainable method.[204] Cellulose-supported photocatalysts leverage the biodegradability, porosity, and structural stability of cellulose.[63] This significantly enhances their light absorption, charge separation, and overall photocatalytic performance, offering a promising pathway for efficient solar water purification.[129] Fig. 11 explains the generalized degradation mechanism for aqueous pollutants using cellulose-based photocatalysts via photocatalysis, Fenton process, and sulfate-based AOPs.

Yan et al. (2024) emphasized the construction of a bamboo-based photocatalyst loaded with ZnO/WO_3 towards the remediation of organic dyes. The pretreatment of bamboo with NaOH facilitates the formation of active nucleation sites within the cellulose microchannels, which in turn promotes the uniform growth of the metal oxides. ZnO/WO_3 was immobilized onto the pretreated bamboo via a hydrothermal strategy. According to the experimental studies, the ZnO/WO_3/bamboo photocatalyst exhibited 93% dye degradation, even after 20 consecutive cycles. Its enhanced catalytic efficacy is ascribed to the synergistic interaction between ZnO and WO_3, which ensured effective charge separation via a type-II pathway. The construction of heterojunctions promotes electron delocalization, enhancing hole migration from the valence band of ZnO to that of WO_3 and suppressing electron–hole recombination. The mechanistic studies revealed that $ZnO–WO_3$ forms a type II heterojunction, enabling the effective separation of photogenerated charges. Under light irradiation, the electrons in the conduction band of ZnO transfer to WO_3, while the holes in the valence band of WO_3 migrate to ZnO. This directional charge flow inhibits electron–hole recombination and facilitates redox reactions, including the reduction of W^{6+} to W^{5+}. It is also noted that the fibrous network and porosity of bamboo offer mechanical stability and abundant active sites, making it appealing as a scaffold for constructing heterojunctions towards the degradation of noxious pollutants.[205] Nitrogen- and boron-co-doped carbon dots prepared through the hydrothermal method were embedded into a 3D porous aerogel matrix for photocatalysis. The Cd(ii)-loaded aerogel was

sulfurized and achieved a 95% efficiency for the degradation of methylene blue (MB). Even after six reuse cycles, this photocatalyst maintained over 90% efficiency. The scavenger studies revealed that photogenerated holes (h^+), hydroxyl radicals ($^•OH$), and superoxide radicals ($^•O_2^-$) played key roles in the degradation mechanism, with $^•O_2^-$ being the dominant reactive species.[206]

Tian et al. (2024) developed an efficient 3D cellulose-TiO_2 photocatalyst through freeze drying, forming a highly porous, tubular architecture. The photocatalytic studies confirmed 100% rhodamine B degradation even under low-light conditions in 4.5 h. Even after 10 cycles of reuse, the removal efficiency declined by just 3%, indicating the phenomenal durability and reusability of the aerogel.[207] Lin et al. (2024) developed a composite composed of MXene, ZnS, and chitosan–cellulose for the efficient removal of anionic dyes through the synergistic interaction between adsorption and photocatalytic degradation. The MXene served as a cocatalyst, forming a Schottky heterostructure with ZnS to enhance photocarrier separation and photocatalytic activity. The composite removed 100% of a 50 mg per L anionic dye solution, driven by electrostatic adsorption and photocatalytic generation of $^•O_2^-$, h^+, and $^•OH$.[208] Ag-doped Cu_2O immobilized on cellulose-derived carbon beads was prepared via chemical reduction and in situ solid-phase precipitation reaction to obtain a highly porous interconnected structure. The Ag-doped Cu_2O immobilized on cellulose-derived carbon beads exhibited 99% levofloxacin degradation, following pseudo-first-order kinetics. The improved efficacy is attributed to the presence of Ag, which benefits from enhanced charge carrier separation, while CBs act as electron reservoirs to improve the photocatalytic performance.[209] Sarkodie et al. (2024) employed flame spray pyrolysis to synthesize Bi_2O_3 nanoparticles, which were subsequently integrated with cellulose acetate (CA) polymer via electrospinning to fabricate a nanofiber membrane. This study revealed strong interactions between CA and the Bi_2O_3 nanoparticles, resulting in enhanced electron transport across the membrane surface, a reduced band gap, and suppressed recombination. The Bi_2O_3/CA nanofiber membrane exhibited a photocatalytic dye degradation efficiency of 95% within 90 min. The electron spin resonance and radical scavenger tests identified $^•OH$ as the primary reactive species responsible for the high photocatalytic activity.[210] Table 8 summarizes different cellulose-based photocatalysts towards wastewater remediation.

The escalating environmental challenges posed by industrialization have intensified the urgency for effective water purification technologies. The integration of cellulose-based materials as supports for photocatalysts offers distinct advantages, including enhanced light absorption, improved charge separation, and mechanical stability, while also aligning with the principles of biodegradability and environmental friendliness. 3D cellulose-based catalysts exhibit phenomenal reusability and ease in catalyst recovery in hybrid forms. The following points must be focused on to establish an efficient photocatalytic system:

5502 | J. Mater. Chem. A, 2026, **14**, 5473–5519

This journal is © The Royal Society of Chemistry 2026

Table 8 Review of different cellulose-supported photocatalysts towards wastewater remediation

Catalyst	Light source	Pollutant	Initial concentration	Efficiency	Reusability	Reference
TiO_2–cellulose (mandarin peels)-based nanocomposite	UV lamp (254 nm)	Methyl orange	100	98.87% in 30 min	6	211
Ag/N–TiO_2 aerogel	500 W Xe lamp	Methylene blue	10	100% in 120 min	—	212
CdS nanoparticles anchored on cotton short-based carbon aerogels	Visible light	Methylene blue	15	95% in 90 min	5	213
Cellulose nanocrystals-TiO_2	Sunlight	Azithromycin	10	98% in 300 min	—	214
Au–TiO_2 bacterial cellulose aerogel	150 W UV lamp	Methylene blue	1.28	89% in 360 min	5	215
ZnO/SnO_2/carbon xerogel	300× vitalux	Methylene blue	25	88% in 300 min	3	216
Carbon dots loaded cellulose nanofibrils hydrogels incorporated Bi_2O_3/BiCOOH	500 W Hg lamp	Lignin	100	93% in 180 min	10	217
$BiVO_4$ lignocellulosic	250 W UV lamp	Rhodamine B	10	90% in 120 min	7	218
Cellulose modified Cu–Al double hydroxide composite	50 W LED lamp	Doxycycline	40	100% in 120 min	4	219
Cu_2O/Ag_2MoO_4 nanofibers on cellulose fibers	250 W Xe lamp	Reactive Blue 19	25	98% in 150 min	5	220
TiO_2 using nanocrystal cellulose	300 W Xe lamp	Phenol	0.01	97.4% in 60 min	6	221
Cellulose acetate membrane doped with Ag–rGO nanocomposites	250 W Hg lamp	Rhodamine B	20	97% in 60 min	4	222
Cellulose–chitosan/β-FeOOH hydrogel	100 W Xe lamp	Methyl orange	40	97% in 40 min	5	223
Polydopamine-bacterial cellulose/GCN	100 W LED lamp	Methylene blue	10	95% in 150 min	3	224
Cellulose composite membrane decorated with Prussian blue analogue	300 W Xe lamp	Tetracycline	10	90%	5	225
Cellulose–chitosan–Ag/Ag_2O/ZnO	UV light (253 nm)	Methyl orange	10	97% in 50 min	3	226
Titania-loaded cellulose functional hybrid material	UV-C lamp	Methylene blue	50	98.5% in 40 min	5	227
$H_3PW_{12}O_{40}$/Fe_3O_4 nanocomposite with cellulose scaffolds	300 W Hg lamp	Methylene blue	10	95% in 5 min	15	228
Ag_3PO_4/nanocellulose composite	Sunlight	Methylene orange	—	90% in 80 min	—	229

• Exploring bio-derived and renewable scaffolds to enhance the sustainability and scalability of photocatalytic materials while maintaining their mechanical resilience and chemical stability.

• Developing multifunctional, integrated systems capable of simultaneous detection, adsorption, and photocatalytic degradation of emerging contaminants to address complex pollution scenarios.

• Addressing practical deployment challenges such as catalyst recovery, cost effectiveness, and long-term environmental impacts to facilitate real-world applications.

• Leveraging computational methods to better understand the charge transfer mechanisms and reactive species dynamics, enabling the rational design of next-generation photocatalysts with tailored functionalities.

6.2.1 Photo-Fenton process. Recent advancements in cellulose-based composite photocatalysts have significantly improved the efficiency, stability, and sustainability of photo-Fenton processes for wastewater treatment. By integrating metal or metal oxide catalysts such as Fe, Cu, TiO_2, and Fe_3O_4 into cellulose matrices, hydrogels, or membranes, these multifunctional systems exhibit enhanced visible-light activity, broader pH applicability, and excellent reusability. These innovative materials present environmentally friendly and cost-effective solutions for the degradation of noxious compounds in wastewater. For instance, Fe-complex incorporated into a cellulose acetate (CA) membrane via tape casting demonstrated a promising visible-light-driven photocatalytic performance. Under visible light and low H_2O_2 concentrations, the Fe-complex/CA membrane efficiently degraded basic fuchsin (100%), methylene blue (93.4%), and sulfadiazine (95.7%) within 60 min. The system followed first-order kinetics and retained catalytic efficiency over four cycles.[230]

Xu et al. (2023) emphasized a heterojunction photocatalyst, $BiYO_3$/g-C_3N_4, which was successfully prepared for the efficient remediation of tetracycline under visible light irradiation. Later, the $BiYO_3$/g-C_3N_4 composite was further immobilized on carbon nanofibers via an electrostatic self-assembly method, resulting in the formation of $BiYO_3$/GCN/cellulose nanofibers with a fluffy, and porous structure. This structure enhanced visible light absorption and facilitated the rapid separation and transfer of photoinduced electron–hole pairs (Fig. 12a). The synergistic combination of adsorption and photocatalysis enabled by the cellulose nanofibers led to phenomenal tetracycline degradation. The composite maintained approximately 90% of its initial photocatalytic performance after five reuse cycles, demonstrating good stability and reusability.[136] A sustainable Fe^0@CS/CF hybrid catalyst, synthesized via eco-friendly methods, has shown high efficiency in the photo-Fenton degradation of levofloxacin (LVX). The photocatalytic studies reported that complete degradation of 25 mg per L LVX was achieved within 40 min under neutral pH (7.0), with

This journal is © The Royal Society of Chemistry 2026

J. Mater. Chem. A, 2026, 14, 5473–5519 | 5503

a catalyst dosage of 0.5 g L^{-1} and 0.5 mL H_2O_2. The enhanced catalytic activity is attributed to the synergistic interactions among chitosan, cellulose fibers (CF), and the composite support, which improved the surface area, adsorption capacity, and interfacial contact with Fe^0. The Fe^0@CS/CF-mediated photo-Fenton degradation of LVX operates *via* a synergistic mechanism involving visible-light-induced photocatalysis and Fenton oxidation, where photoexcited electron–hole pairs generate reactive oxygen species ($^{\bullet}$OH and $O_2^{\bullet-}$), which initiate

and sustain the degradation process (Fig. 12b). The adsorption of LVX on the catalyst surface, photolysis of H_2O_2, and cyclic redox conversion between Fe^{2+}/Fe^{3+} boosted the generation of radicals and contributed to the degradation of LVX. The mechanistic analysis indicates that hydroxyl radicals drive a multi-step oxidative pathway involving hydroxylation, de-methylation, decarboxylation, and quinolone ring cleavage, aiding the degradation of LVX.[231]
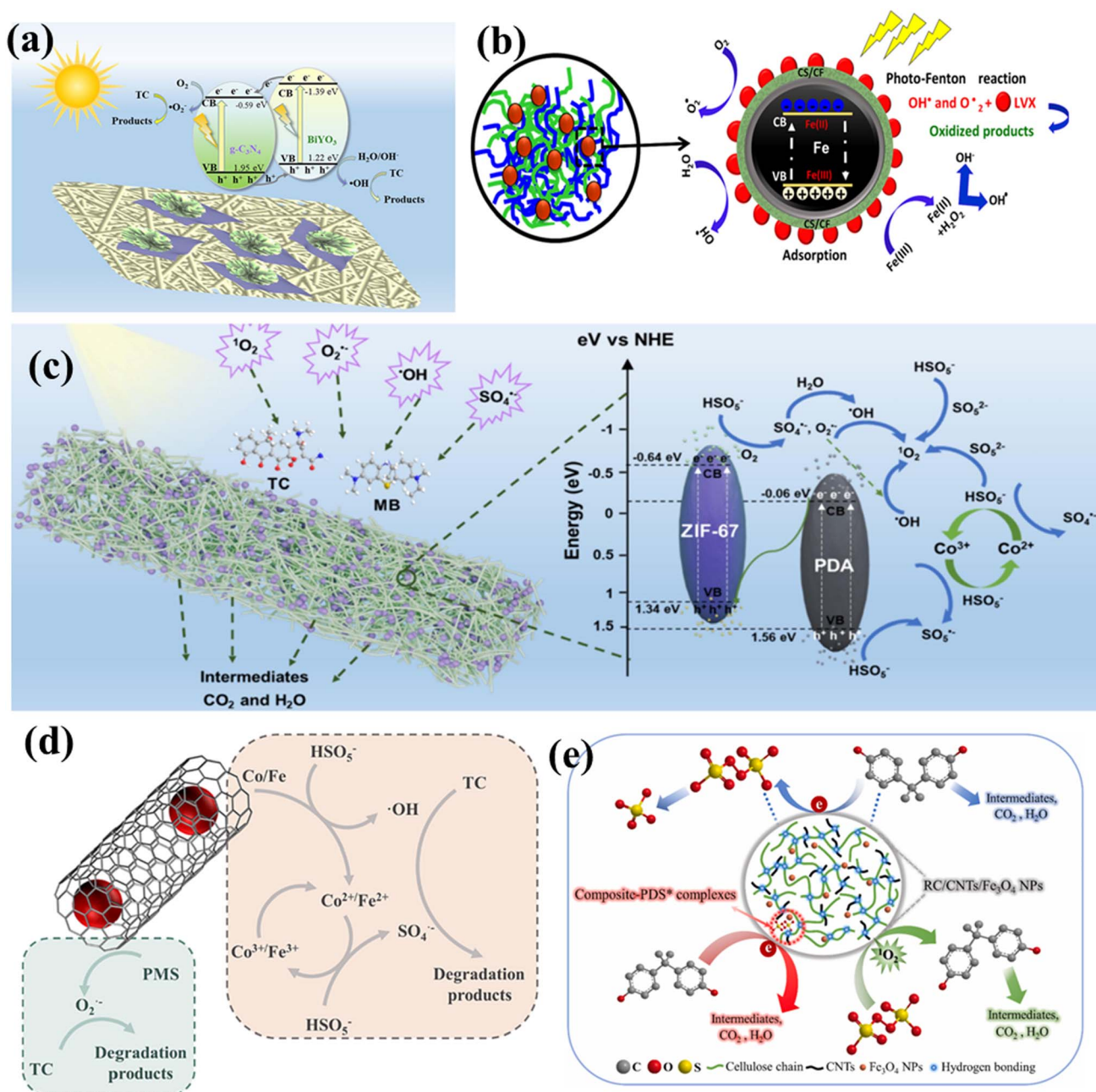

Fig. 12 (a) Diagram of tetracycline degradation using GCN/BiYO$_4$ *via* photocatalysis. Reprinted with permission from ref. 136, Elsevier (2023). (b) Photo-Fenton-assisted mechanism for the degradation of LVX using Fe^0@chitosan/cellulose green hybrid structures. Reprinted with permission from ref. 202, Elsevier (2024). (c) Mechanism for the degradation of tetracycline using the PMS system. Reprinted with permission from ref. 232, Elsevier (2025). (d) Schematic of proposed tetracycline degradation using the CoFe$_{0.8}$@NCNT@CA/PMS catalytic system. Reprinted with permission from ref. 233, Elsevier (2022). (e) Diagram of bisphenol-A degradation using RC/CNT/Fe$_3$O$_4$ nanoparticles. Reprinted with permission from ref. 234.

5504 | *J. Mater. Chem. A*, 2026, **14**, 5473–5519

This journal is © The Royal Society of Chemistry 2026

A recent study reported the development of a cellulose-based nanocomposite hydrogel incorporating TiO_2 and Fe_3O_4 as dual catalysts synthesized via situ synthesis and mineralization. Here, TiO_2 was found to modulate the hydrogen bonding network, contributing to faster gelation, reduced pore size, and improved mechanical strength. Meanwhile, Fe_3O_4 imparted magnetic properties by anchoring onto cellulose chains. This dual-functional hydrogel demonstrated enhanced photocatalytic activity in the photo-Fenton process, achieving up to 97.5% removal of methylene blue within 60 min. Notably, this system maintained high degradation efficiency across a pH range of 4–7 and exhibited excellent stability over five reuse cycles without significant pollutant leakage.[235] Li et al. (2022) emphasized that in situ co-precipitation was employed to fabricate $PVA/CNF/Fe_3O_4$ hybrid hydrogels, wherein Fe_3O_4 nanoparticles are uniformly dispersed within a polyvinyl alcohol (PVA) and cellulose nanofiber (CNF) matrix. The hydrogel not only provides structural stability and magnetic recoverability but also facilitates enhanced Fe^{2+}/Fe^{3+} redox cycling under light irradiation. When applied as a photo-Fenton catalyst, the system effectively activated H_2O_2 to generate reactive ·OH radicals, enabling the efficient degradation of tetracycline. Under the optimal conditions (pH 3, 100 mM H_2O_2, 0.3 g per L catalyst, 25 °C), the hybrid hydrogel achieved 98% removal within 120 min, following pseudo-first-order kinetics.[236]

A $Co_3O_4@Fe_3O_4$/cellulose membrane, prepared by integrating Co_3O_4-coated MOF-derived Fe_3O_4 with a cellulose matrix, was applied in a visible-light-driven photo-Fenton system for PFOA degradation. The EPR and scavenger studies revealed a synergistic mechanism involving photogenerated electrons, holes, and multiple radical species. The membrane achieved 94.5% PFOA removal within 180 min, with minimal metal leaching (Fe: 0.05 ppm and Co: 0.49 ppm), and retained

80.4% efficiency after five cycles.[237] To enhance both the catalytic performance and recyclability, a cellulose-derived carbon-supported Cu–Fe composite (MA–Cu–Fe@C) was synthesized via the mechanical activation of precursors followed by one-step calcination. The mechanical activation promoted the formation of abundant active sites, strong Cu–Fe interactions, and uniform embedding within the carbon matrix, enabling a synergistic enhancement in the photo-Fenton system. The catalyst demonstrated high activity in the pH range of 3–9, achieving 98.8% methylene blue degradation and 73.7% TOC removal. Remarkably, it retained over 96% degradation efficiency after 20 reuse cycles, highlighting its excellent stability and reusability.[238]

The developments in cellulose-supported photocatalysts have marked a significant step towards sustainable and efficient wastewater remediation (Table 9). By combining the structural versatility and biodegradability of cellulose with the redox activity of metal or metal oxide components, these materials offer enhanced photocatalytic performance, broader pH operating ranges, and excellent reusability. However, challenges remain in terms of their scalability, affordability, and fundamental understanding of their mechanisms under dynamic environmental conditions. Addressing these aspects will be essential to transition from lab-scale innovation to practical deployment.

• Utilization of natural sunlight as an effective light source to reduce the energy dependence of the proposed technology.

• Employment of in situ characterization techniques to unravel the radical generation pathways and pollutant degradation mechanisms.

• Development of multifunctional designs that integrate additional capabilities such as antimicrobial activity, pollutant sensing, and self-healing characteristics.

Table 9 Summary of different cellulose-supported catalysts employed in photo-Fenton systems

Catalyst	Pollutant	Initial concentration mg L^{-1}	Efficiency	Reusability	Reference
Co, Fe-bimetallic MIL-88A/MCC composites	Rhodamine B	5	87% in 100 min	5	239
CMC-assisted litchi-like zinc ferrite	Tetracycline	0.04 mM	80% in 18 min	4	240
CuS@carbon nanocomposites	2,4-DCP	25	90% in 150 min	5	241
Magnetite nanoparticle-decorated cellulose aerogel	p-Nitrophenol	2000	92% in 60 min	5	242
Fe(II)-crosslinked alginate CMC beads	Malachite green	10	98% in 30 min	—	243
Polydopamine-coated carbonized cotton fabrics with β-FeOOH nanorods	Methylene blue	50	80% in 70 min	6	244
Wood-converted porous carbon decorated with MIL-101(Fe)	Ciprofloxacin	10	99% in 120 min	5	245
Lignin-based electrospun nanofiber membrane decorated with photo-Fenton Ag@MIL-100(Fe)	Methylene blue		99% in 30 min	—	246
Durian fiber loaded with FeOOH nanoparticles	Tetracycline	5	96% in 100 min	—	247
Cu–Fe/wood-converted porous carbon	Methylene blue Sulfamethoxazole	10	100% in 5 min	5	248
Fe_3O_4-starch-derived carbon	Tetracycline	5 mM	98% in 35 min	5	249
MOF-on-MOF-derived Fe–Zr bimetal oxides supported on hierarchically porous carbon	Ciprofloxacin	20	99% in 120 min	5	250
Red mud supported on rice husk biochar	Ciprofloxacin	20	95% in 120 min	—	251

This journal is © The Royal Society of Chemistry 2026

J. Mater. Chem. A, 2026, 14, 5473–5519 | 5505

• Prioritize sustainable synthesis using bio-based precursors and solvent-free processes for the preparation of cellulose-based photocatalysts.

6.2.2 Sulfate-based AOPs. Advanced oxidation processes (AOPs) have gained prominence as an effective strategy for removing persistent organic pollutants (POPs) from water, owing to their capability to generate abundant and highly reactive oxygen species (ROS), which drive rapid contaminant degradation. Among them, hydroxyl radicals ($E^0 = 2.8$ V) and sulfate radicals ($E^0 = 2.5$–3.1 V) are particularly notable owing to their oxidative strength and broad-spectrum reactivity.[252] In comparison with traditional AOPs, sulfate-based AOPs have attracted substantial attention due to their higher redox potential, longer half-life, and superior reactivity towards a wide range of pollutants.[93] Peroxymonosulfate (PMS) and persulfate (PS) are commonly used oxidants for the generation of sulfate radicals, which are activated via thermal, chemical, photolytic, or catalytic pathways.[253] However, despite their strong oxidative potential, sulfate-based AOPs often fail to fully mineralize pollutants, necessitating the integration of catalytic systems for enhanced activation.[254] These hybrid catalysts enable dual PMS activation via both radical and non-radical pathways, achieving the rapid and selective degradation of pollutants.

Tian et al. (2025) explored an integrated approach for fabricating a cellulose-based electrospun photocatalytic membrane via synchronous electrospinning of cellulose acetate and electrospraying of a core–shell PMMA@PDA@ZIF-67 heterojunction. The catalytic membrane exhibited degradation against tetracycline (93%) and methylene blue (99%) through PMS activation under visible light. Its improved efficacy is ascribed to its enhanced light absorption and charge separation, while its electrospun architecture ensured uniform catalyst distribution and reusability. The synergistic action of light and PMS, a case of reactive species such as a singlet oxygen-dominated non-radical pathway, facilitated the rapid abatement of micropollutants, as shown in Fig. 12c.[232] Ren et al. (2018) described the immobilization of zeolitic imidazole framework (ZIF) materials such as ZIF-9 and ZIF-12 on cellulose aerogels to fabricate hybrid aerogels, which acted as efficient activators towards PMS activation. The hybrid catalytic systems demonstrated superior catalytic activity towards the remediation of Rhodamine B, tetracycline and p-nitrophenol. Mechanistic studies using EPR analysis and radical quenching techniques confirmed that the activation of PMS by the hybrid aerogels generated both $SO_4^{\cdot-}$ and $^{\cdot}OH$, with $SO_4^{\cdot-}$ identified as the dominant reactive species.[255]

Han et al. (2022) reported the degradation of diclofenac using a wood pulp cellulose biochar/GCN composite via PMS activation. The experimental studies demonstrated the complete degradation of diclofenac in 25 min with a reusability of 5 cycles. The integration of waste pine biochar with GCN significantly enhanced the visible light absorption, improved charge separation, reduced the electrical resistance, and boosted both the photocatalytic activity and PMS activation. The key reactive species such as $^{\cdot}OH$, h^+, and $^{\cdot}O_2^-$ were implicated in the radical mechanism, while $^1O_2$ and direct electron transfer dominated the nonradical degradation pathway.[256] Similarly, nitrogen-doped carbon catalysts were synthesized using waste cotton fibers with four distinct crystalline structures as carbon sources via the carbonization process towards the degradation of Reactive Blue 19. The results indicated that within 40 min, the degradation efficiency of the nitrogen-doped carbon catalysts against Reactive Blue 19 reached 99% with a reusability of 4 cycles. The scavenger analysis claimed the superior role of $^1O_2$ as the main ROS involved in non-radical-based electron transfer-mediated dye degradation.[257] Gan et al. (2019) reported the use of carbon nanofibers derived from cellulose as a support to enhance the catalytic performance of $CoFe_2O_4$ for PMS activation. The carbon nanofiber/$CoFe_2O_4$ nanocomposites demonstrated high efficiency in degrading dimethyl phthalate, a model organic pollutant in aqueous media. The phenomenal degradation is indicated to the presence of carbon nanofibers, which enhanced the potential of cobalt ferrite by reducing its tendency towards agglomeration and enhancing electron transfer. The spinel-structured $CoFe_2O_4$ imparted magnetic separability, enabling easy recovery and reusability for 5 cycles.[258]

In another study, a $CoFe_{0.8}$@NCNT@CA composite was prepared, wherein carbon nanotubes (NCNTs) derived from a Co–Fe bimetallic MOF were uniformly loaded onto a cellulose aerogel matrix. The hybrid material demonstrated remarkable catalytic activity for the activation of PMS, achieving a tetracycline degradation efficiency of 97% in 20 min. Its high performance is attributed to the synergistic interplay among its bimetallic active centers, graphitic nitrogen functionalities, and hierarchical porous structure of the aerogel. Notably, the unique semi-coated architecture formed between the carbon nanotubes and the cellulose scaffold enhances the adhesion and stability of CNT, exposes abundant catalytic sites, and facilitates efficient mass transport factors, which play a crucial role in achieving a higher degradation rate in an aqueous environment. The mechanistic investigations reveal that the $CoFe_{0.8}$@NCNT@CA/PMS system operates through a combination of direct electron transfer and radical-mediated pathways (Fig. 12d).[233] Dong et al. (2022) reported the synthesis of magnetic and porous regenerated cellulose/carbon nanotube (CNTs)/Fe_3O_4 nanoparticle composites in a green alkaline-urea medium, which were applied for peroxydisulfate activation to degrade bisphenol A (BPA). The regenerated cellulose/carbon nanotube (CNT)/Fe_3O_4 nanoparticle composites achieved 100% removal of bisphenol-A. This enhanced performance was attributed to their defect sites, nitrogen doping, functional groups, and the formation of a conductive network. The mechanistic studies revealed a dominant non-radical-mediated degradation pathway, as shown in Fig. 12e.[234]

Cellulose-based photocatalytic-PMS/PS systems have demonstrated significant promise for the efficient degradation of POPs in the aqueous environment (Table 10). The integration of cellulose with photocatalysts has led to the development of highly efficient hybrid catalysts with charge carrier dynamics, surface area, light utilization, and pollutant adsorption. These systems not only leverage radical mechanisms but also exploit

5506 | J. Mater. Chem. A, 2026, **14**, 5473–5519

This journal is © The Royal Society of Chemistry 2026

Table 10 Summary of different cellulose-based photocatalysts employed in sulfate-based AOPs

Catalyst	Pollutant	Initial concentration	Efficiency	Reusability	Reference
S-doped cellulose nanocrystals with edge sulfur vacancies	Ciprofloxacin	40	100% in 25 min	5	259
CuS hollow nanosphere@N-doped cellulose nanocrystal composites	Ciprofloxacin	20	99.5% in 180 min	—	260
Fe-MOF (MIL-101-Fe)-derived porous carbon material	Sulfadiazine	20	100% in 15 min	3	261
Co-ZIF@cellulose aerogels	p-Nitrophenol	10	98% in 70 min	3	262
MOF/bacterial cellulose-derived octahedral MnO/carbon nanofiber	Tetracycline	50	90% in 30 min	5	263
Amphoteric CMC/sodium alginate/polyethyleneimine/ZIF-67	Rhodamine B	20	100% in 120 min	5	264
ZIF-67/MXene/carbon nanofiber aerogels	Tetrabromobisphenol-A	40	99% in 40 min	5	265
Cellulose@carbon nitride@ZIF-67	Norfloxacin	50	99% in 60 min	7	266
Fe-doped black phosphorous carbonized cotton fiber	Tetracycline	10	95% in 150 min	—	267
	Congo red	40	98% in 60 min	7	
	Methylene blue	5	99% in 60 min	—	
ZIF-67/cellulose membrane	Methylene blue	10	100% in 1 min	4	268
	Rhodamine B			—	

non-radical pathways, especially $^1O_2$ and direct electron transfer, which are gaining attention due to their selective and less toxic degradation routes. Dual or synergistic activation using light and PMS/PS opens new avenues for effective pollutant abatement. However, future research should focus on (i) the rational design of cellulose-derived frameworks with precisely controlled pore structures, surface functionalities and hierarchical architectures, which will enhance the pollutant–catalyst interactions and activation efficiency. (ii) Considering the increasing environmental concerns regarding metal leaching, there is growing interest in developing robust, metal free-cellulose supported catalysts for water treatment applications. Translating the lab-scale efficiency of pilot and industrial-scale systems requires efforts in reactor design, membrane modularization, and continuous flow operations.

Photocatalytic wastewater remediation offers a sustainable and energy efficient approach to degrade noxious contaminants using efficient photocatalysts. The integration of cellulose as a support material not only enhances the adsorption of pollutants and dispersion of the catalyst but also promotes effective charge separation by acting as an electron mediator, thereby enhancing the photocatalytic efficiency. This green strategy aligns with environmental goals due to its low toxicity, biodegradability, and ability to operate under mild conditions. A SWOT analysis reveals its strong potential due to its renewable energy basis and environmental compatibility, though limitations such as its narrow light absorption and scalability must be addressed (Fig. 13). The future opportunities lie in engineering multifunctional cellulose-based hybrid materials with enhanced light absorption, pollutant selectivity, and reusability as well as deploying decentralized treatment units for remote areas. However, challenges such as ensuring cost-effectiveness, long-term operational stability, and competing with well-established conventional treatment technologies remain critical barriers to its widespread adoption.

6.3 Disinfection

The proliferation of pathogenic microorganisms in the water environment poses critical health hazards, contributing towards the outbreak of infectious diseases and ecological imbalance.[4] However, the conventional antimicrobial methods often fall short due to their poor efficacy, secondary pollution, and microbial resistance. In this context, photocatalytic disinfection has garnered growing attention as a sustainable alternative in environmental applications.[269] Engineered cellulose-photocatalysts exposed to visible light generate highly active charge carriers, which initiate oxidative degradation pathways. These photoinduced ROS species such as $^{\bullet}OH$ and $^{\bullet}O_2^-$ are potent enough to disrupt microbial membranes, damaging intercellular components, and leading to cell death.[270] Cellulose, owing to its high surface area, porosity, and abundant –OH, provides an excellent scaffold for uniform catalyst dispersion and improved light–catalyst interaction. Maślana et al. (2022) developed a scalable cellulose-based substrate functionalized with exfoliated GCN and silver nanoparticles, which demonstrated effective self-cleaning and antimicrobial activities. The composite exhibited 100% inactivation of E. coli and S. aureus within 2 h under light and 24 h under dark conditions. This material exhibited strong potential for antimicrobial surfaces; however, concerns such as nanoparticle leaching, long-term stability, and reusability must be addressed.[271]

CMC-based hydrogels offer renewable and biocompatible platforms for supporting sunlight-responsive photocatalysts; however, their dense matrix often induces a light shielding effect, which hampers disinfection efficacy. Thus, to overcome this, Wang et al. (2025) utilized polydopamine as an interfacial mediator, leveraging its quinhydrone charge-transfer ability to facilitate electron transport between the embedded catalysts. A double network CMC/PDA gel, formed via chemical cross-linking and hydrogen bonding, enabled the in situ formation of an Ag/AgCl/ZnO heterojunction with greater catalytic activity.

This journal is © The Royal Society of Chemistry 2026
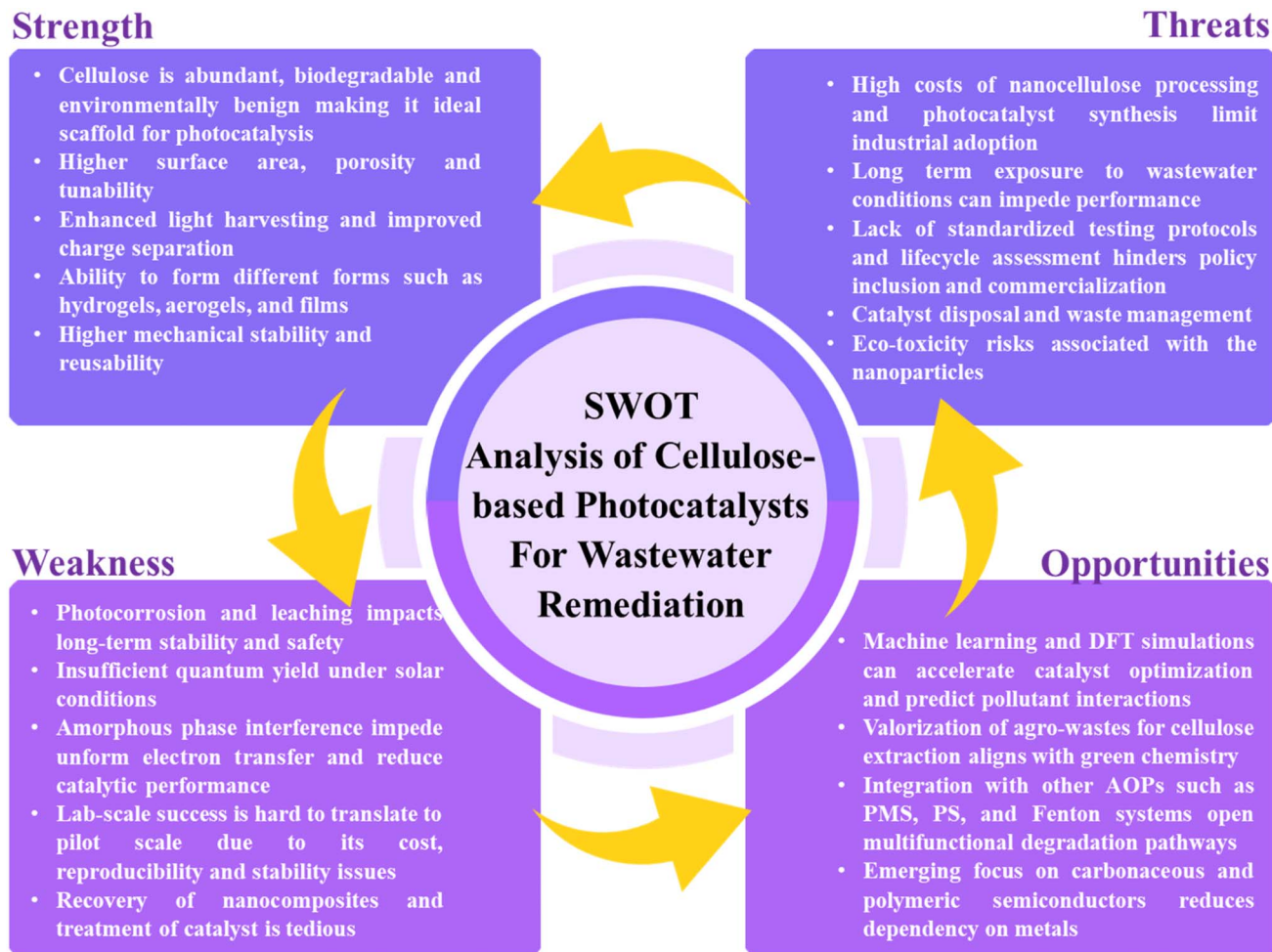
J. Mater. Chem. A, 2026, 14, 5473–5519 | 5507

Fig. 13 SWOT analysis of cellulose-based photocatalysts for wastewater remediation including photocatalysis and photo-Fenton, and sulfate-based AOPs.

The composite gel achieved almost complete bactericidal activity under sunlight, with a larger inhibition zone under irradiation than dark conditions, highlighting its light dependent efficacy.[272] A TiO₂NPs@CMC hydrogel was developed by incorporating hydrothermally synthesized TiO_2 nanoparticles into a carboxymethyl cellulose (CMC) matrix, followed by $CaCl_2$ crosslinking. The hydrogel exhibited strong antimicrobial and antibiofilm activity against key waterborne pathogens, including *S. typhi*, *E. coli* O157, *Shigella dysenteriae*, and *B. cereus*, with inhibition zones up to 29 mm. At 100 μg mL⁻¹, it significantly reduced the bacterial counts, achieving complete pathogen inactivation in sewage within 180 min.[273] Huang *et al.* (2023) developed a photocatalytic hydrogel *via* the *in situ* immobilization of ZnO and/or Ag/AgCl nanoparticles, with epichlorohydrin serving as a crosslinker and Cl source for AgCl deposition. The resulting nanocomposite gels exhibited pH-responsive swelling and enhanced Zn^{2+} release under acidic conditions. The Ag/AgCl-loaded gels demonstrated a superior antibacterial performance against *E. coli* and *S. aureus* under 6 h of sunlight, significantly outperforming dark conditions. Also, these materials showed no cytotoxicity below 0.33 mg mL⁻¹ and maintained structural stability.[274]

Bacterial cellulose (BC) derived from *Acetobacter xylinum* served as a robust 3D scaffold for the *in situ* synthesis of TiO_2 nanoparticles. The BC/N–F–TiO_2 composite exhibited a superior catalytic disinfection performance under visible light, effectively targeting both Gram-negative and Gram-positive bacteria. It is also noticed that its antibacterial activity is influenced by both the bacterial type and the doping level, indicating the need for precise compositional tuning.[275] In another study, Shen *et al.* (2022) reported a one-step biosynthetic approach to immobilize MoS_2 on BC to yield MoS_2/BC composites, which demonstrated synergistic photodynamic and photothermal activity. In the presence of H_2O_2, BC/MoS_2 generated hydroxyl radicals (˙OH) and achieved >99% (6-log) reduction of *E. coli* and *S. aureus* under near-infrared (NIR) light (100 W, 760–5000 nm) within 5 min. The mechanistic insights highlighted the dual action of ROS-mediated oxidative stress and MoS_2-induced hyperthermia as the key contributor towards disinfection efficacy.[276] A GO–TiO_2 nanohybrid was integrated into bacterial cellulose (BC) to form a porous, photocatalytically active composite. TiO_2 nanoparticles (10–30 nm) with mixed anatase–rutile phases were uniformly anchored on GO sheets, maintaining strong ROS generation under near-UV light. The GO–TiO_2/BC composite
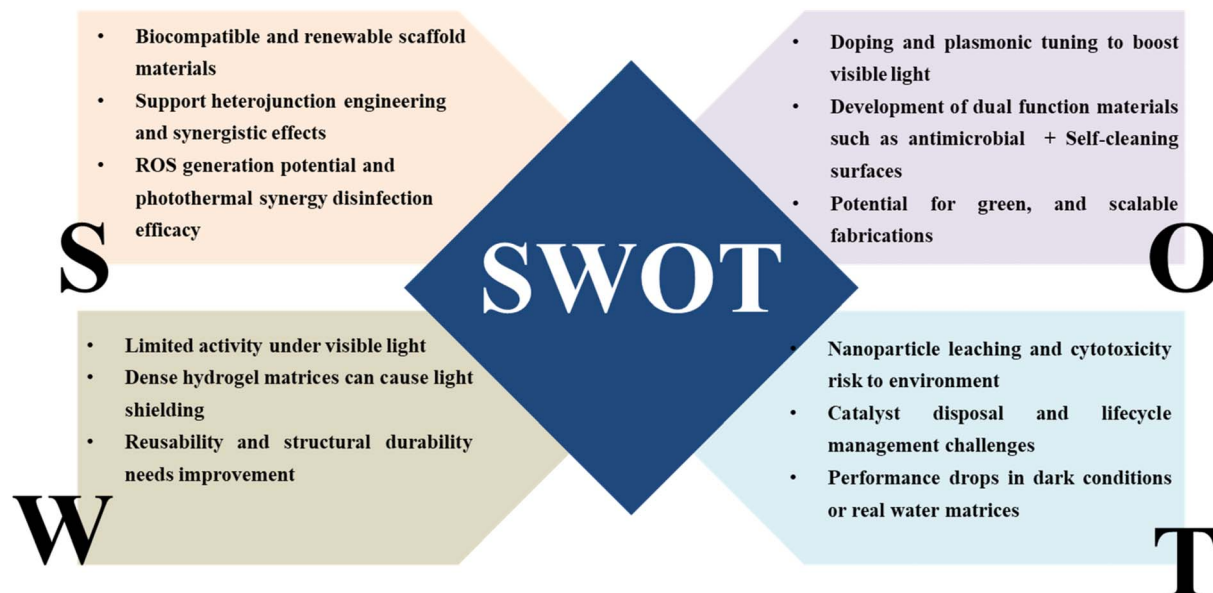
5508 | *J. Mater. Chem. A*, 2026, **14**, 5473–5519

This journal is © The Royal Society of Chemistry 2026

Strengths (S)
- Biocompatible and renewable scaffold materials
- Support heterojunction engineering and synergistic effects
- ROS generation potential and photothermal synergy disinfection efficacy

Opportunities (O)
- Doping and plasmonic tuning to boost visible light
- Development of dual function materials such as antimicrobial + Self-cleaning surfaces
- Potential for green, and scalable fabrications

Weaknesses (W)
- Limited activity under visible light
- Dense hydrogel matrices can cause light shielding
- Reusability and structural durability needs improvement

Threats (T)
- Nanoparticle leaching and cytotoxicity risk to environment
- Catalyst disposal and lifecycle management challenges
- Performance drops in dark conditions or real water matrices

Fig. 14 SWOT analysis for cellulose-supported photocatalysts towards disinfection.

showed effective antibacterial activity against *S. aureus* upon irradiation, with no dark cytotoxicity observed. The hybrid leveraged the charge transport ability of GO and the reactivity of TiO_2, while BC provided structural support. However, although it is promising for antimicrobial and photocatalytic applications, its UV-dependence and oxidative stress risks require further evaluation.[277]

Cellulose-supported photocatalysts, particularly those based on CMC and bacterial cellulose, offer a sustainable, biocompatible platform for light-assisted disinfection. The integration of photocatalysts into these matrices has enabled efficient antimicrobial action through ROS production, photothermal effect and heterojunction engineering. These systems demonstrated broad spectrum pathogen inactivation including bacterial and viral surrogates, with strong performances under sunlight or UV irradiation. However, key challenges like nanoparticle leaching, limited visible light responsiveness, long-term stability, and environmental safety remain unsolved. Thus, future efforts should focus on (i) enhancing visible-light activity *via* doping and plasmonic effects, (ii) ensuring reusability and structural durability, and (iii) minimizing toxicity through safe-by-design nanostructures. Fig. 14 presents the SWOT analysis of cellulose-supported photocatalysts towards disinfection. With these advancements, cellulose-based photocatalytic materials hold strong potential for real-world applications in water purification, antimicrobial surfaces and public health protection.

7. Environmental and economic analysis

The environmental impact of cellulose-based composites is mainly concentrated during their production and use phases (Fig. 15). Cellulose is sourced from renewable plant biomass such as agricultural residues and wood pulp and obtained through eco-friendly and cost-effective processes that minimize ecological harm.[256,278] In contrast, conventional materials like petroleum-based plastics, metals, and synthetic rubbers come from finite mineral reserves whose extraction and refining are resource intensive. For example, fossil-based plastics can produce 1.6–6.4 kg CO_2-eq per kg over their life cycle.[279] Meanwhile, bio-derived cellulose materials such as nanofibrils have reported life-cycle carbon footprints ranging from -1.6 to $+12.2$ kg CO_2-eq per kg, depending on their synthesis route and how biogenic carbon is handled.[280] The fabrication of cellulose composites is generally simpler and potentially more environmentally benign. For example, advanced nanocellulose production processes, especially those using hybrid mechanical + enzymatic treatments, show significantly lower environmental burdens. Life-cycle inventory studies report cumulative energy demands in the range of a few MJ per kg for certain optimized CNF production routes, and pretreatment wastewater volumes of 0.44–1.6 L per 10 g of nanofibrils.[281,282] These numbers underscore how emerging process designs can minimize resource consumption compared with more energy- and chemically intensive manufacturing routes.

Cellulose-based composites also offer strong biodegradability, preventing long-term environmental accumulation.[283] For instance, carboxymethyl cellulose (CMC) shows quantifiable biodegradation in activated-sludge systems, where OECD 301B tests report 41–46.7% mineralization by day 28 and 55.2–63.7% by day 70. Under higher inoculum conditions, degradation accelerates to >60% DOC removal within 15 days. OECD 314B studies further show >60% mineralization in just 6 h, with ultimate biodegradation rate constants of 0.8–1.6 h^{-1} and rapid primary depolymerization at 5.0 h^{-1}. These values clearly demonstrate the rapid microbial breakdown of cellulose derivatives, underscoring their suitability as environmentally benign
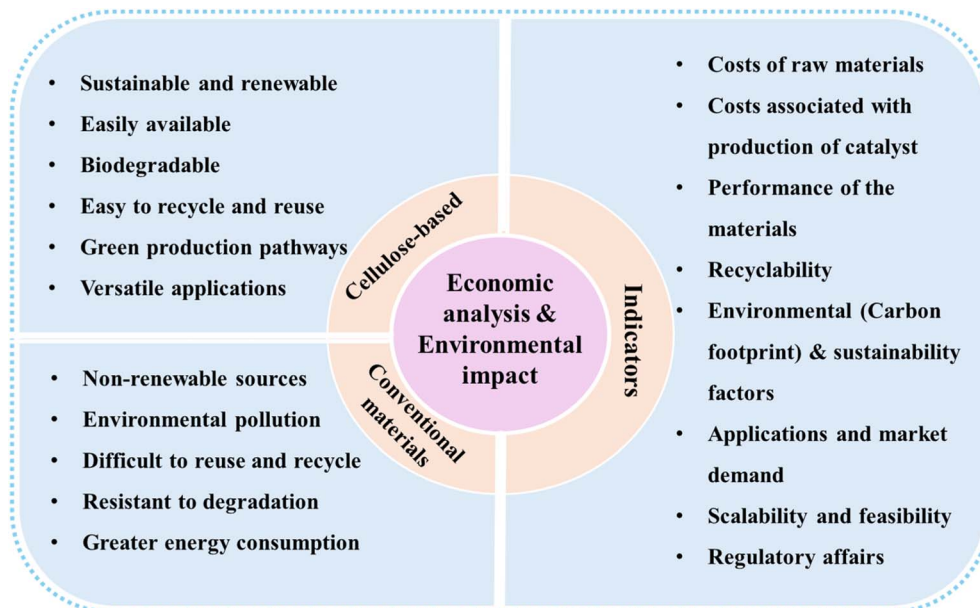
Fig. 15 Economic and environmental analyses of cellulose-supported photocatalysts.

alternatives to persistent synthetic polymers.[284] Additionally, cellulose composites often exhibit strong adsorption and photocatalytic properties, making them effective for water purification and environmental remediation.[159] For example, cellulose/ZnO composites derived from agricultural waste exhibited 45% dye removal of bromophenol blue and methyl orange within 20 min of UV irradiation and 65% removal of methylene blue under either UV or white light, with only a 15–19% loss in performance after three reuse cycles, indicating both strong adsorption and durable photocatalytic activity.[285]

Cellulose-based materials exhibit markedly better reusability and lower operational cost than nano-sized photocatalysts.[36] Regenerated cellulose–carbon hybrids retain 82–85% of their capacity after 10 cycles (2% loss per cycle),[286] whereas granular carbon-based materials often recover only 65% after a single regeneration cycle.[287] Life-cycle assessments further report production costs of US$1.06 per kg for biochar-based materials, compared with US$1.34 per kg for commercial AC.[288] These metrics confirm that cellulose-derived materials offer a significantly lower cost-per-use and superior long-term stability for sustainable adsorption applications.

Mechanically, cellulose composites show enhanced strength and toughness, combined with environmental sustainability attributes that many traditional materials lack. For example, ZnO/cellulose fiber composite membranes exhibit strong wet-state mechanical stability, with tensile stress increasing from 0.07 ± 0.01 MPa (microfiber-dominated structure) to 0.67 ± 0.02 MPa at an optimized nano-/micro-fiber ratio, while maintaining low mass loss (4.68 ± 1.35 wt%) after 48 h of dynamic oscillation in water, confirming the reinforcing synergy between microfibers and nanofibers.[289] Furthermore, cellulose possesses natural antibacterial properties, where synthetic materials typically require added antimicrobial agents.[273] For instance,

Ag@AgCl–cellulose hybrids have shown inhibition zones of 6.9 mm against *E. coli* and 10.8 mm against *S. aureus*, confirming effective microbial suppression through the synergy between the cellulose matrix and active species. Similar cellulose–metal hybrid systems commonly achieve 3–5 log bacterial reduction, underscoring their strong antimicrobial potential. This multifunctionality enables cellulose composites to integrate photocatalysis, adsorption, and antibacterial activity within a single biodegradable platform, enhancing their environmental and application value.[290] These reductions in carbon footprint, energy demand, wastewater generation, and regeneration cost translate into lower operational expenditure (OPEX) and improved process efficiency, thereby strengthening the industrial scalability and market adoption potential of cellulose-supported photocatalysts.

Overall, cellulose-supported photocatalysts integrate low material cost, renewable feedstock availability, excellent recyclability, tunable physicochemical functionality, and strong environmental compatibility.[257] This broad relevance supports their expansion across water remediation, biomedical coatings, active packaging, and sustainable energy systems. The global cellulose market, valued at approximately USD 219.5 billion in 2018, is projected to reach USD 305.1 billion by 2026 at a CAGR of 4.2%, reflecting the growing industrial demand for low-carbon materials.[291] Ongoing scale-up of green fabrication technologies is expected to further reduce costs and improve the device-level efficiencies, strengthening the competitiveness of cellulose-based photocatalytic technologies. These reductions in embodied energy, synthesis-related emissions, and regeneration costs directly translate to improved photocatalytic cost–performance ratios, thereby enhancing the feasibility of the large-scale deployment and accelerating the commercial adoption of cellulose-supported photocatalytic systems.

5510 | *J. Mater. Chem. A*, 2026, **14**, 5473–5519

This journal is © The Royal Society of Chemistry 2026

8. Current challenges and prospects

Cellulose-supported photocatalysts have attained prominent importance in the field of environmental remediation and sustainable fuel production, which contribute to the concept of a green economy, circular economy, and SDGs. However, despite their functionality and efficacy, their challenges need to be addressed to ensure the complete exploration of cellulose as a photocatalyst support. The major identified research areas that must be considered for future research are discussed below:

(i) Technological advancements in cellulose-based photocatalysts: the deployment of cellulose-supported or derived photocatalysts is limited by the intrinsic constraints of cellulose such as low solubility, high crystallinity, restricted chain mobility, and limited accessibility of its surface-active hydroxyl groups. Also, conventional cellulose extraction and modification routes remain energy-intensive and environmentally taxing, limiting their scalability. Future research must focus on developing processing methods that directly exploit the inherent physicochemical characteristics of cellulose including hierarchical morphology, tunable crystallinity, and dense hydrogen-bond networks to optimize light absorption, interfacial charge separation, and catalytic site availability, instead of relying heavily on its chemical post-modification. The integration of nano- and micro-crystalline cellulose *via in situ* assembly or self-templating routes can provide higher surface area and more uniform dispersion of catalytic components. Moreover, AI-assisted optimization of the processing parameters, defect engineering, and rational dopant selection can improve the performance reproducibility and accelerate the transition from laboratory demonstrations to practical systems.

(ii) Engineering smart cellulose platforms towards photocatalytic applications: the chemical richness of cellulose, particularly its abundant reactive –OH groups, enables versatile structure–property tuning through controlled functionalization. Tailored modifications (carbonization, carboxylation, and grafting) can improve adsorption, wettability, and interfacial electron transfer, enhancing its role as an active contributor rather than a passive support. Challenges remain in achieving long-term structural stability, scalable processing, and reproducible functionalization. To avoid overlap with technological constraints, green-chemistry strategies are emphasized here specifically in the context of platform design such as solvent-free functionalization, bio-based modifiers for targeted surface chemistry, and energy-efficient activation pathways that allow the creation of adaptive cellulose architectures with tunable surface states. These engineered platforms can help establish consistent material properties and high compatibility with a wide range of photocatalytic semiconductors.

(iii) Heterostructures in cellulose-based catalysts: incorporating heterostructures into cellulose matrices offers a promising pathway for achieving superior photocatalytic performance through enhanced charge separation, broadened light harvesting, and synergistic interfacial interactions. The intrinsic multi-scale structural order, mechanical flexibility, and high-aspect-ratio fibrils of cellulose enable efficient nanoparticle anchoring, dispersion, and stabilization attributes that conventional supports often lack. However, despite these advantages, several materials-science challenges associated with heterostructure construction remain underexplored. Major obstacles include poorly controlled heterointerface formation, which generates interfacial defects; lattice mismatch between inorganic semiconductors and the semi-crystalline cellulose framework; unpredictable band alignment arising from heterogeneous surface chemistry; and non-uniform nucleation, leading to particle aggregation. Additionally, the effects of interfacial strain, exciton transport behaviour, and charge-transfer pathways across the organic–inorganic boundary are not yet fully understood. Current studies also lack mechanistic clarity on how cellulose modulates the recombination dynamics through its hydrogen bonding networks, surface functional groups, or crystalline polymorphs. Thus, to overcome these limitations, future work must emphasize defect-controlled and morphology-preserving fabrication strategies, coupled with green, solvent-minimal processing routes that align with sustainable material development. Equally important is the implementation of advanced characterization approaches including *operando* spectroscopies, interface-resolved electron microscopy, and multiscale theoretical modeling to establish clear structure–property–performance correlations. These integrated strategies will be essential for engineering next-generation cellulose-based heterojunction systems with predictable interfaces, optimized charge transport, and scalable manufacturability.

(iv) Hydrogels, sponges, and membranes for enhanced reuse: a major challenge in realizing the real-world application of cellulose-based photocatalysts is achieving their easy recovery, mechanical robustness, and long-term operational stability. Conventional powder catalysts often aggregate, exhibit poor recyclability, and lose their activity over repeated cycles, motivating the shift toward structured formats such as hydrogels, sponges, and membranes. Cellulose imparts mechanical reinforcement, flexibility, and tunable functionality, while enabling the uniform dispersion of catalytic components. These macroscopic architectures improve the reusability, stability, and scalability, making them better suited for practical water treatment. Future research should prioritize mechanical strengthening strategies, optimization of the porosity–strength balance, and enhanced fatigue resistance to support sustained performances in continuous-flow systems.

(v) AI-enhanced predictive modeling and kinetic analysis: AI approaches can unravel complex dependencies among the structure of cellulose, material morphology, and photocatalytic behavior. Algorithms such as support vector regression, random forests, and neural networks can enable the data-driven prediction of band structures, heterojunction stability, charge-transfer rates, and reaction kinetics, minimizing the need for iterative experimentation and accelerating material discovery.

(vi) Expanding photocatalytic applications towards fuel generation: cellulose-supported photocatalysts are gaining traction in clean energy and green chemical synthesis, particularly for hydrogen, ammonia and hydrogen peroxide

This journal is © The Royal Society of Chemistry 2026

J. Mater. Chem. A, 2026, **14**, 5473–5519 | **5511**

production. Their high surface area, functional tunability, and ability to support efficient charge separation make them ideal for coupling with semiconductors and co-catalysts. In hydrogen generation, cellulose scaffolds enhance light harvesting and charge transport, but challenges remain in achieving higher efficacy under visible light and ensuring catalyst durability. In the case of ammonia synthesis *via* photocatalytic nitrogen fixation, cellulose-based systems offer eco-friendly alternatives to the energy-intensive Haber–Bosch process; however, their low conversion rates and interference from competing reactions limit their scalability. In hydrogen peroxide production, cellulose supports enable selective two-electron oxygen reduction, but require precise control over the reaction pathways to prevent the generation of undesired by-products. Across all applications, their real-world deployment is hindered by their limited quantum yields and reliance on sacrificial agents.

(vii) Consideration of real wastewater scenarios: despite the extensive research and efficacy, cellulose-supported photocatalysts remain limited to laboratory-scale studies. In contrast, industrial wastewater is complex and composed of a variety of pathogens, organic, and inorganic pollutants, cellulose-based catalysts must be designed not only for higher efficacy under ideal conditions but also for resilience and adaptability in real-world applications. Further efforts should be devoted to the fabrication of hybrid cellulose platforms that are capable of integrating multiple functional units for the simultaneous degradation noxious pollutants. Finally, toxicity studies and pilot-scale validations are critical in transforming cellulose-based photocatalytic systems from proof-of-concept studies to industrial wastewater treatment technologies.

(viii) Advancing disinfection applications *via* photocatalysis: although cellulose-based photocatalysts exhibit strong potential for pathogen inactivation, challenges remain in understanding the cellulose–microorganism interactions, ensuring the non-toxicity of surface modifiers, and maintaining structural integrity in biological environments. Smart antimicrobial platforms with triggered ROS generation, anti-fouling surfaces, and biofilm disruption capabilities must be prioritized.

(ix) Challenges towards commercialization: the commercialization of cellulose-based photocatalysts faces several challenges that hinder their transition from the laboratory to industrial scale. Cellulose is abundant and readily available from renewable resource such as wood pulp, cotton, bio-waste, and agricultural wastes, but ensuring consistent quality, purity, and functional compatibility for advanced photocatalytic applications requires substantial processing and modifications, which result in higher processing costs. Chemical treatments, surface functionalization, and integration with photocatalytic components involve complex, multi-step procedures that can limit scalability and introduce variability. One of the major technical hurdles lies in maintaining the inherent biodegradability, flexibility, and renewability of cellulose, while imparting enhanced photocatalytic functionality, stability, and reusability. Further, performance optimization remains essential to meet the industrial demands of thermal stability, mechanical strength, and long-term photocatalytic activity under diverse environmental conditions. Standardized production protocols,

rigorous quality control, and reproducibility are required to ensure consistent product performance. Environmental consideration must also be addressed, especially regarding the use of toxic chemicals or solvents during the modification of cellulose and the generation of waste streams. Market uncertainty and the lack of established models for bio-based photocatalytic materials further complicate commercialization efforts. Thus, to overcome these obstacles, it is vital to invest in green synthesis technologies, develop low-cost and eco-friendly modification methods, strengthen R&D partnerships with industries, and engage with regulatory bodies to streamline approvals. Strategic collaborations, policy support, and pilot-scale demonstrations will be key to enabling the commercialization of cellulose-based photocatalysts as viable, scalable solutions for environmental remediation and clean energy applications.

9. Conclusions

Cellulose-supported photocatalysts represent a promising and sustainable solution to meet critical global challenges in clean energy production and environmental remediation. Their intrinsic properties including high surface area, biocompatibility, porosity, and chemical tunability make cellulose an ideal support material for photocatalysts. This review has provided an in-depth exploration of the photocatalytic mechanisms, structural strategies, material classifications and application-specific advances in cellulose-based systems. Detailed emphasis is given to the design engineering aspects of cellulose-photocatalysts. This is followed by the classification of cellulose-supported photocatalysts into cellulose-based composite photocatalysts and structured cellulose-based photocatalytic systems. The potential applications of cellulose-supported catalysts are explored in the areas of hydrogen production, hydrogen peroxide production, ammonia generation, carbon dioxide sequestration, wastewater remediation, and disinfection. To comprehensively evaluate this field, a SWOT analysis was conducted, which offers a systematic perspective on the current technological landscape, potential advantages, existing barriers, and future research opportunities. However, despite the significant progress, critical challenges remain in scaling up the fabrication, enhancing the visible-light activity, ensuring the long-term operational stability, and achieving the commercial viability of these systems. Moving forward, innovations in heterostructure design, green processing methods, AI-driven optimizations, and real-world system integration will be pivotal. With focused interdisciplinary efforts, cellulose-supported photocatalysts can play a central role in enabling scalable, eco-friendly, and multifunctional technologies aligned with circular economy principles and the United Nations Sustainable Development Goals.

Conflicts of interest

The authors declare no conflict of interest.

5512 | *J. Mater. Chem. A*, 2026, **14**, 5473–5519

This journal is © The Royal Society of Chemistry 2026

Data availability

Data will be available from the authors on request.

Acknowledgements

References

1 H. Dong, G. Zeng, L. Tang, C. Fan, C. Zhang, X. He and Y. He, *Water Res.*, 2015, 128–146, DOI: 10.1016/j.watres.2015.04.038.

2 X.-J. Wen, X. Wu, L. Hu, X.-K. Wu, H. Guo, B.-B. Qian, Z.-T. Liu, H.-Z. Li and Z.-H. Fei, *Coord. Chem. Rev.*, 2025, **526**, 216377.

3 A. Balakrishnan, F. P. Mathew, E. Sebastian Kunnel, M. M. Varghese, S. Trivedi, M. Binoy, M. Chinthala, N. Rajamohan and B. Weng, *Nanoscale*, 2025, **17**, 18534–18559.

4 A. Balakrishnan, M. M. Jacob, M. Chinthala, N. Dayanandan, M. Ponnuswamy and D.-V. N. Vo, *Environ. Chem. Lett.*, 2024, **22**, 635–656.

5 A. Balakrishnan, S. Appunni, M. Chinthala and D. V. N. Vo, *Environ. Chem. Lett.*, 2022, 3071–3098.

6 X. Song, Y. Duan, S. Li, P. Ouyang, L. Chen, H. Ma, W. Wang, Y. Li and F. Dong, *Coord. Chem. Rev.*, 2025, **526**, 216351.

7 B. Weng, M. Zhang, Y. Lin, J. Yang, J. Lv, N. Han, J. Xie, H. Jia, B. Su, M. Roeffaers, J. Hofkens, Y. Zhu, S. Wang and W. Choi, *Nat. Rev. Clean Technol.*, 2025, **1**, 201–215.

8 A. Balakrishnan, S. Appunni and K. Gopalram, *Int. J. Biol. Macromol.*, 2020, **161**, 282–291.

9 Q. Xu, B. Zhu, C. Jiang, B. Cheng and J. Yu, *Sol. RRL*, 2018, **2**, 1–10.

10 Z. Ding, S. Wang, X. Chang, D. H. Wang and T. Zhang, *RSC Adv.*, 2020, **10**, 26246–26255.

11 S. Li, S. Meng, H. Zhang, A. R. Puente-Santiago, Z. Wang, S. Chen, M. J. Muñoz-Batista, Y.-M. Zheng and B. Weng, *Adv. Funct. Mater.*, 2025, e13682.

12 N. Rana, S. Chand and A. K. Gathania, *Int. Nano Lett.*, 2016, **6**, 91–98.

13 K. Wang, Z. Xing, M. Du, S. Zhang, Z. Li, S. Yang, K. Pan, J. Liao and W. Zhou, *J. Colloid Interface Sci.*, 2021, **592**, 259–270.

14 Q. Chen, Z. Zhang, Y. Chen, J. C. Yu, C. Liu and L. Wu, *Appl. Catal. B Environ. Energy*, 2026, **380**, 125823.

15 A. Balakrishnan, K. Vijaya Suryaa, M. Chinthala and A. Kumar, *J. Colloid Interface Sci.*, 2024, **669**, 366–382.

16 Y. Ai, S. A. C. Carabineiro, X. Xiong, H. Zhu, Q. Wang, B. Weng and M.-Q. Yang, *Chinese J. Catal.*, 2025, **75**, 147–163.

17 H. Yan, Z. Zhu, Y. Long and W. Li, *Colloids Surf., A*, 2019, **582**, 123857.

18 A. Balakrishnan and M. Chinthala, *Chemosphere*, 2022, 134190.

19 A. Balakrishnan, E. S. Kunnel, R. Sasidharan, M. Chinthala and A. Kumar, *Chem. Eng. J.*, 2023, 146163.

20 H. Dong, G. Zeng and L. Tang, *Water Res.*, 2015, **79**, 128–146.

21 S. H. Khan and B. Pathak, *Environ. Nanotechnol., Monit. Manage.*, 2020, **13**, 100290.

22 Y. Ren, Y. Li, G. Pan, N. Wang, Y. Xing and Z. Zhang, *J. Mater. Sci. Technol.*, 2024, **171**, 162–184.

23 J. Thomas, K. S. Ambili and S. Radhika, *Catal. Today*, 2018, **310**, 11–18.

24 A. Balakrishnan, R. Sasidharan, M. Chinthala and A. Kumar, *Ind. Eng. Chem. Res.*, 2024, **63**, 2605–2618.

25 K. Vijaya Suryaa, A. Balakrishnan, M. Chinthala, K. Bidya Devi, H. Tripathy, A. Kumar, T. M. Aminabhavi and S. Rtimi, *Chem. Eng. J.*, 2025, **505**, 159470.

26 I. E. Khalil, C. Xue, W. Liu, X. Li, Y. Shen, S. Li, W. Zhang and F. Huo, *Adv. Funct. Mater.*, 2021, **31**, 2010052.

27 D. Wang, X. Huang, Y. Huang, X. Yu, X. Lei, X. Dong and Z. Su, *Colloids Surf., A*, 2021, **611**, 125780.

28 P. Zhou, X. Meng, L. Li and T. Sun, *J. Alloys Compd.*, 2020, **827**, 154259.

29 D. Hao, Q. Huang, W. Wei, X. Bai and B. J. Ni, *J. Cleaner Prod.*, 2021, **314**, 128033.

30 C. Liu, J. You, Y. Li, H. Zhu, L. Xia and X. Zhuang, *Carbohydr. Polym.*, 2023, **316**, 121072.

31 H. M. Ali, F. Arabpour Roghabadi and V. Ahmadi, *Sol. Energy*, 2023, **255**, 99–125.

32 H. Musarurwa and N. T. Tavengwa, *Carbohydr. Polym.*, 2022, **275**, 118743.

33 H. N. Abdelhamid and A. P. Mathew, *Coord. Chem. Rev.*, 2022, **451**, 214263.

34 M. A. Mohamed, M. Abd Mutalib, Z. A. Mohd Hir, M. F. M. Zain, A. B. Mohamad, L. Jeffery Minggu, N. A. Awang and W. N. W. Salleh, *Int. J. Biol. Macromol.*, 2017, 1232–1256.

35 M. Li, W. Yao, M. Yu, C. Sun, X. Deng, F. Chen, L. Zhou and Y. Zheng, *Sep. Purif. Technol.*, 2022, **299**, 121758.

36 A. Balakrishnan, K. Vijaya Suryaa, H. Tripathy, S. Trivedi, A. Kumar and M. Chinthala, *J. Colloid Interface Sci.*, 2024, **663**, 1087–1098.

37 J. Wen, J. Xie, X. Chen and X. Li, *Appl. Surf. Sci.*, 2017, **391**, 72–123.

38 A. Balakrishnan, M. Chinthala, R. Polagani and D.-V. N. Vo, *Environ. Res.*, 2023, **216**, 18–52.

39 S. Meenakshi and M. Farzana, *Ind. Eng. Chem. Res.*, 2013, **53**, 55–63.

40 R. Bariki, S. Kumar Pradhan, S. Panda, S. Kumar Nayak, D. Majhi, K. Das and B. G. Mishra, *Sep. Purif. Technol.*, 2023, **314**, 123558.

41 K. Das, R. Bariki, S. K. Pradhan, D. Majhi, P. Dash, A. Mishra, R. Dhiman, B. Nayak and B. G. Mishra, *Chemosphere*, 2022, **306**, 135600.

42 Y. Li, Y. Fang, Z. Cao, N. Li, D. Chen, Q. Xu and J. Lu, *Appl. Catal. B Environ.*, 2019, **250**, 150–162.

This journal is © The Royal Society of Chemistry 2026

J. Mater. Chem. A, 2026, **14**, 5473–5519 | 5513

43 M. Chinthala, A. Balakrishnan, P. Venkataraman, V. Manaswini Gowtham and R. K. Polagani, *Environ. Chem. Lett.*, 2021, **19**, 4415–4454.

44 K. Das, R. Bariki, D. Majhi, A. Mishra, K. K. Das, R. Dhiman and B. G. Mishra, *Appl. Catal. B Environ.*, 2022, **303**, 120902.

45 S. Vigneshwaran, P. Sirajudheen, C. P. Nabeena, V. P. Sajna and S. Meenakshi, *Int. J. Biol. Macromol.*, 2021, **183**, 2088–2099.

46 A. Balakrishnan, M. Chinthala, A. Kumar, N. Dayanandan and S. Trivedi, *Int. J. Hydrogen Energy*, 2025, **98**, 1020–1033.

47 W. Kong, Z. Xing, B. Fang, Y. Cui, Z. Li and W. Zhou, *Appl. Catal. B Environ.*, 2022, **304**, 120969.

48 Y. Xue, C. Ma, Q. Yang, X. Wang, S. An, X. Zhang and J. Tian, *Chem. Eng. J.*, 2023, **457**, 141146.

49 X. Liu, R. Ma, L. Zhuang, B. Hu, J. Chen, X. Liu and X. Wang, *Crit. Rev. Environ. Sci. Technol.*, 2021, **51**, 751–790.

50 L. Jiang, X. Yuan, Y. Pan, J. Liang, G. Zeng, Z. Wu and H. Wang, *Appl. Catal., B*, 2017, 388–406.

51 S. Singh, H. Mahalingam and P. K. Singh, *Appl. Catal. A-Gen.*, 2013, **462-463**, 178–195.

52 J. Fu, J. Yu, C. Jiang and B. Cheng, *Adv. Energy Mater.*, 2018, **8**, 1–31.

53 J. Low, J. Yu, M. Jaroniec, S. Wageh and A. A. Al-Ghamdi, *Adv. Mater.*, 2017, **29**, 1–20.

54 J. Lee, L. L. Tan and S. P. Chai, *Nanoscale*, 2021, **13**, 7011–7033.

55 A. Balakrishnan, G. J. Gaware and M. Chinthala, *Chemosphere*, 2023, **310**, 136853.

56 A. Balakrishnan, M. Chinthala, A. Kumar and S. Rtimi, *Chem. Eng. J.*, 2024, **496**, 153899.

57 S. Chen, D. Huang, P. Xu, W. Xue, L. Lei, M. Cheng, R. Wang, X. Liu and R. Deng, *J. Mater. Chem. A*, 2020, **8**, 2286–2322.

58 H. Park, H. Il Kim, G. H. Moon and W. Choi, *Energy Environ. Sci.*, 2016, **9**, 411–433.

59 C. Zhang, Y. Li, D. Shuai, Y. Shen and D. Wang, *Chem. Eng. J.*, 2019, **355**, 399–415.

60 A. Y. Shan, T. I. M. Ghazi and S. A. Rashid, *Appl. Catal., A*, 2010, **389**, 1–8.

61 A. Balakrishnan, E. S. Kunnel, R. Sasidharan, M. Chinthala and A. Kumar, *ACS Sustain. Chem. Eng.*, 2024, **12**(13), 5169–5185.

62 M. Lee, B. Y. Chen and W. Den, *Appl. Sci.*, 2015, 1272–1283.

63 A. A. Adesibikan, S. S. Emmanuel, C. O. Olawoyin and P. Ndungu, *J. Organomet. Chem.*, 2024, **1010**, 123087.

64 A. Sudhaik, P. Raizada, T. Ahamad, S. M. Alshehri, V.-H. Nguyen, Q. Van Le, S. Thakur, V. K. Thakur, R. Selvasembian and P. Singh, *Int. J. Biol. Macromol.*, 2023, **226**, 1284–1308.

65 P. Xu, J. Yang, Y. Chen, Y. Li, X. Jia and H. Song, *Mater. Des.*, 2019, **183**, 108179.

66 T. Shan, Y. Wang, D. Luo, Z. Huang, F. Zhang, H. Wu, L. Huang, J. Li, L. Chen and H. Xiao, *Appl. Catal. B Environ. Energy*, 2024, **349**, 123872.

67 A. Liu, J. Liu, S. He, J. Zhang and W. Shao, *Int. J. Biol. Macromol.*, 2023, **225**, 40–50.

68 T. K. Bindu Sharmila, C. S. Julie Chandra, Sreesha Sasi and C. K. Arundhathi, *Modification of cellulose*, Springer Nature Singapore, Singapore, 2023, pp. 1–37.

69 B. A. Marinho, R. O. Cristóvão, R. Djellabi, J. M. Loureiro, R. A. R. Boaventura and V. J. P. Vilar, *Appl. Catal. B Environ.*, 2017, **203**, 18–30.

70 M. A. Mohamed, W. W. N. Salleh, J. Jaafar, A. F. Ismail, M. A. Mutalib, N. A. A. Sani, S. E. A. M. Asri and C. S. Ong, *Chem. Eng. J.*, 2016, **284**, 202–215.

71 Y. Zhang, F. Liu, L. Zhong, Z. Dong, C. Chen and Z. Xu, *Appl. Surf. Sci.*, 2023, **641**, 158425.

72 H. Xiao, Y. Shan, S. Wu, T. Shan, H. Luo, F. Zhang, L. Huang, L. Chen and G. Liao, *Chem. Eng. J.*, 2024, **492**, 152228.

73 M. Österberg, K. A. Henn, M. Farooq and J. J. Valle-Delgado, *Chem. Rev.*, 2023, **123**, 2200–2241.

74 H. Nasser Abdelhamid, S. Sultan and A. P. Mathew, *Chem. Eng. J.*, 2023, **468**, 143567.

75 R. N. Goldberg, J. Schliesser, A. Mittal, S. R. Decker, A. F. L. O. M. Santos, V. L. S. Freitas, A. Urbas, B. E. Lang, C. Heiss, M. D. M. C. Ribeiro da Silva, B. F. Woodfield, R. Katahira, W. Wang and D. K. Johnson, *J. Chem. Thermodyn.*, 2015, **81**, 184–226.

76 E. Dinand, M. Vignon, H. Chanzy and L. Heux, *Cellulose*, 2002, **9**, 7–18.

77 Y. Liang, W. Zhu, C. Zhang, R. Navik, X. Ding, M. S. Mia, M. N. Pervez, M. I. H. Mondal, L. Lin and Y. Cai, *Cellulose*, 2021, **28**, 7435–7453.

78 C. Huang, H. Yu, S. Y. H. Abdalkarim, Y. Li, X. Chen, X. Yang, Y. Zhou and L. Zhang, *Carbohydr. Polym.*, 2022, **276**, 118766.

79 D. Zhi, J. Wang, Y. Zhou, Z. Luo, Y. Sun, Z. Wan, L. Luo, D. C. W. Tsang and D. D. Dionysiou, *Chem. Eng. J.*, 2020, **383**, 123149.

80 R. S. Riseh, M. G. Vazvani, M. Hassanisaadi and V. K. Thakur, *Ind. Crops Prod.*, 2024, **208**, 117904.

81 P. Gao, H. Y. Khong, A. Wibowo, Y. Zhen, C. Peng and W. Miao, *Heliyon*, 2024, **10**(12), e32321.

82 R. Roy, M. Eldhose, C. George, A. Joseph, S. Thomas, A. A. R., C. Jose Chirayil and B. Thomas, *Nanocellulose-Based (Bio)composites for Optoelectronic Applications*, Springer Nature Singapore, Singapore, 2023, pp. 1059–1084.

83 M. Sumini, G. J. S. Andrade, C. A. Tischer, R. K. T. Kobayashi and G. Nakazato, *Cellulose*, 2025, **32**, 81–94.

84 S. Balkissoon, J. Andrew and B. Sithole, *Biomass Convers. Biorefinery*, 2023, **13**, 16607–16642.

85 N. Lavoine, I. Desloges, A. Dufresne and J. Bras, *Carbohydr. Polym.*, 2012, **90**, 735–764.

86 K. J. Nagarajan, N. R. Ramanujam, M. R. Sanjay, S. Siengchin, B. Surya Rajan, K. Sathick Basha, P. Madhu and G. R. Raghav, *Polym. Compos.*, 2021, **42**, 1588–1630.

87 A. Sharma, M. Thakur, M. Bhattacharya, T. Mandal and S. Goswami, *Biotechnol. Rep.*, 2019, **21**, e00316.

88 G. Yang, H. Kong, Y. Chen, B. Liu, D. Zhu, L. Guo and G. Wei, *Carbohydr. Polym.*, 2022, **279**, 118947.

5514 | *J. Mater. Chem. A*, 2026, **14**, 5473–5519

This journal is © The Royal Society of Chemistry 2026

89 Y. Shan, Y. Guo, Y. Wang, X. Du, J. Yu, H. Luo, H. Wu, B. Boury, H. Xiao, L. Huang and L. Chen, *J. Colloid Interface Sci.*, 2021, **599**, 507–518.

90 T. T. Hong, H. Okabe, Y. Hidaka, B. A. Omoldi and K. Hara, *Polymer*, 2019, **181**, 121772.

91 A. Rana, A. Sudhaik, P. Raizada, A. A. P. Khan, Q. Van Le, A. Singh, R. Selvasembian, A. Nadda and P. Singh, *Nanotechnol. Environ. Eng.*, 2021, **6**, 40.

92 X. Qian, Y. Xu and Y. Xu, *Int. J. Biol. Macromol.*, 2024, **259**, 127873.

93 A. Balakrishnan, M. Chinthala, A. Kumar, D. Barceló and S. Rtimi, *Chem. Eng. J.*, 2025, **503**, 158378.

94 Y. Guo, J. Bae, Z. Fang, P. Li, F. Zhao and G. Yu, *Chem. Rev.*, 2020, **120**, 7642–7707.

95 Y. Wang, X. Wang, Y. Xie and K. Zhang, *Cellulose*, 2018, **25**, 3703–3731.

96 A. Kumar, G. Sharma, M. Naushad, A. H. Al-Muhtaseb, A. García-Peñas, G. T. Mola, C. Si and F. J. Stadler, *Chem. Eng. J.*, 2020, **382**, 122937.

97 C. Shi, B. An, L. Zhang, Z. Zai, Z. Shi, Z. Wang and J. Ma, *Appl. Surf. Sci.*, 2023, **618**, 156633.

98 B. Mohan, *Top. Curr. Chem.*, 2025, **383**, 44.

99 K. M. Alam, P. Kumar, N. Chaulagain, S. Zeng, A. Goswami, J. Garcia, E. Vahidzadeh, M. L. Bhaiyya, G. M. Bernard, S. Goel, V. K. Michaelis, A. E. Kobryn, S. Gusarov and K. Shankar, *J. Phys. Chem. C*, 2022, **126**, 15635–15650.

100 Y. Li, M. Wang, Y. Meng, Q. Wang, Q. Fu, C. Yu, L. Zhu, L. Cai, C. Chen, C. Xia and S. Wang, *ACS Appl. Mater. Interfaces*, 2025, **17**, 30365–30401.

101 S. Ghosh, D. Sarkar, S. Bastia and Y. S. Chaudhary, *Nanoscale*, 2023, **15**, 10939–10974.

102 Y. Shchipunov and I. Postnova, *Adv. Funct. Mater.*, 2018, **28**, 1705042.

103 A. Etale, A. J. Onyianta, S. R. Turner and S. J. Eichhorn, *Chem. Rev.*, 2023, **123**, 2016–2048.

104 M. Hasanin, R. M. Abdelhameed, S. Dacrory, H. Abou-Yousef and S. Kamel, *Mater. Sci. Eng., B*, 2021, **270**, 115231.

105 H. Tian and J. He, *Langmuir*, 2016, **32**, 12269–12282.

106 S. Habibi and M. Jamshidi, *Mater. Sci. Semicond. Process.*, 2020, **109**, 104927.

107 C. Shi, L. Zhang, Z. Shi, Z. Wang and J. Ma, *Int. J. Biol. Macromol.*, 2023, **228**, 435–444.

108 M. Yan, B. An, X. Li, Z. Zai, S. Wu, J. Ma and L. Zhang, *Appl. Surf. Sci.*, 2023, **637**, 157974.

109 J. Liu, S. Tang, P. Zhang, Z. Wang, W. Dai, R. Wen, L. Wang, W. Wang and J. Wang, *J. Colloid Interface Sci.*, 2025, **700**, 138411.

110 C. Wang, J. Li, E. Paineau, A. Laachachi, C. Colbeau-Justin, H. Remita and M. N. Ghazzal, *J. Mater. Chem. A*, 2020, **8**, 10779–10786.

111 G. Chu, H. Yin, H. Jiang, D. Qu, Y. Shi, D. Ding and Y. Xu, *J. Phys. Chem. C*, 2016, **120**, 27541–27547.

112 C. Shi, L. Zhang, H. Bian, Z. Shi, J. Ma and Z. Wang, *J. Cleaner Prod.*, 2021, **288**, 125089.

113 S. Liu, T. Xu, L. Zhu, K. Liu, X. Ji, Z. Yuan and C. Si, *Chem. Eng. J.*, 2025, **503**, 158564.

114 N. Lakshmana Reddy, V. Navakoteswara Rao, M. Mamatha Kumari, R. R. Kakarla, P. Ravi, M. Sathish, M. Karthik, S. Muthukonda Venkatakrishnan and Inamuddin, *Nanostructured Semiconducting Materials for Efficient Hydrogen Generation*, Springer International Publishing, 2018, vol. 16, pp. 765–796.

115 N. Shehzad, M. Tahir, K. Johari, T. Murugesan and M. Hussain, *J. CO2 Util.*, 2018, **26**, 98–122.

116 X. Zhang and S. P. Jiang, *Mater. Today Energy*, 2022, **23**, 100904.

117 B. Palanivel, R. R. Macadangdang, M. S. Hossain, F. A. Alharthi, M. Kumar, J.-H. Chang and S. Gedi, *J. Rare Earths*, 2023, **41**, 77–84.

118 J. Qin, Y. Dou, J. Zhou, V. M. Candelario, H. R. Andersen, C. Hélix-Nielsen and W. Zhang, *Adv. Funct. Mater.*, 2023, **33**, 2214839.

119 F. Guo, W. Shi, W. Guan, H. Huang and Y. Liu, *Sep. Purif. Technol.*, 2017, **173**, 295–303.

120 X. Hu, Y. Yu, D. Chen, W. Xu, J. Fang, Z. Liu, R. Li, L. Yao, J. Qin and Z. Fang, *Chem. Eng. J.*, 2022, **432**, 134375.

121 S. Sugashini, T. Gomathi, R. A. Devi, P. N. Sudha, K. Rambabu and F. Banat, *Environ. Res.*, 2022, **204**, 112047.

122 N. Janpetch, N. Saito and R. Rujiravanit, *Carbohydr. Polym.*, 2016, **148**, 335–344.

123 H. Li, L. Zhang, H. Lu, J. Ma, X. Zhou, Z. Wang and C. Yi, *Carbohydr. Polym.*, 2020, **250**, 116873.

124 H. Helmiyati, N. Fitriana, M. L. Chaerani and F. W. Dini, *Opt. Mater.*, 2022, **124**, 111982.

125 Z. Xu, M. He, Y. Zhou, M. Zhang, S. Feng, Y. Wang, R. Xu, H. Peng and X. Chen, *Chem. Eng. J.*, 2022, **428**, 131127.

126 P. Zhang, J. Zhang, D. Wang, F. Zhang, Y. Zhao, M. Yan, C. Zheng, Q. Wang, M. Long and C. Chen, *Appl. Catal. B Environ.*, 2022, **318**, 121749.

127 S. Pushpalatha, M. V. Arularasu, C. Palanivel, T. V Rajendran and A. Manikandan, *Biomass Convers. Biorefinery*, 2024, **15**, 26687–26694.

128 V. Soni, M. Malhotra, P. Singh, A. A. P. Khan, W. A. Bawazir, V.-H. Nguyen, T. Ahamad, Q. Van Le, P. Raizada and K. A. Alzahrani, *J. Environ. Chem. Eng.*, 2025, **13**, 115151.

129 M. Malhotra, A. Sudhaik, Sonu, P. Raizada, T. Ahamad, V.-H. Nguyen, Q. Van Le, R. Selvasembian, A. K. Mishra and P. Singh, *Ind. Crops Prod.*, 2023, **202**, 117000.

130 T. Zhang, Y. Xiang, Y. Su, Y. Zhang, X. Huang and X. Qian, *Ind. Crops Prod.*, 2022, **187**, 115357.

131 Q. Wang, Y. Xiang, X. Li, W. Zhang, X. Huang and X. Qian, *Ind. Crops Prod.*, 2021, **170**, 113695.

132 S. Jiang, Q. Hu, M. Xu, S. Hu, X.-C. Shi, R. Ding, P.-L. Tremblay and T. Zhang, *Carbohydr. Polym.*, 2020, **250**, 116909.

133 N. Tavker and M. Sharma, *J. Environ. Manage.*, 2020, **255**, 109906.

134 C. Liao, W. Jing, F. Wang and Y. Liu, *Mater. Today Catal.*, 2023, **3**, 100030.

135 Y. Liang, J. Xiong, Q. Yang and S. Wang, *J. Colloid Interface Sci.*, 2023, **651**, 976–986.

This journal is © The Royal Society of Chemistry 2026

J. Mater. Chem. A, 2026, **14**, 5473–5519 | **5515**

136 H. Xu, Y. Zhang, Y. Wang, L. Zhang, Z. Zhang, L. Zhong, Z. He, Y. Zheng and Y. Shen, *Carbohydr. Polym.*, 2023, **312**, 120829.

137 C. Zhao, F. Ran, L. Dai, C. Li, C. Zheng and C. Si, *Carbohydr. Polym.*, 2021, **255**, 117343.

138 N. S. N. Hasnan, M. A. Mohamed, N. A. Nordin, W. N. R. Wan Ishak and M. B. Kassim, *Carbohydr. Polym.*, 2023, **317**, 121096.

139 C. Yue, L. Chen, H. Zhang, J. Huang, H. Jiang, H. Li and S. Yang, *Environ. Sci.:Water Res. Technol.*, 2023, **9**, 669–695.

140 A. Balakrishnan, M. M. Jacob, N. Dayanandan, M. Chinthala, M. Ponnuchamy, D. V. N. Vo, S. Appunni and A. S. Gajendhran, *Mater. Adv.*, 2023, **4**, 5920–5947.

141 S. Bej, H. Sarma, M. Ghosh and P. Banerjee, *Environ. Pollut.*, 2023, **323**, 121278.

142 J. Khodayari, K. Zare, O. Moradi, M. Kalaee and N. Mohammad Mahmoodi, *J. Photochem. Photobiol., A*, 2024, **446**, 115097.

143 L. Zheng, S. Wang, S. Zhang, Y. Zu, X. Huang and X. Qian, *J. Colloid Interface Sci.*, 2024, **676**, 532–542.

144 J. Wang, W. Wang, Y. Deng, T. Yang, Z. Zhang, H. Wang and Y. Wu, *Sep. Purif. Technol.*, 2024, **340**, 126840.

145 S. Jiang, Z. Yan, Y. Deng, W. Deng, H. Xiao and W. Wu, *Int. J. Biol. Macromol.*, 2024, **262**, 129854.

146 Z. Yuan, Y. Chen, C. Qiu, M.-C. Li, J. Qi, C. F. de Hoop, A. Zhao, J. Lai, X. Zhang and X. Huang, *Int. J. Biol. Macromol.*, 2023, **249**, 126118.

147 J.-X. Ren, J.-L. Zhu, S.-C. Shi, M.-Q. Yin, H.-D. Huang and Z.-M. Li, *Carbohydr. Polym.*, 2022, **296**, 119957.

148 Y. Xue, Y. Lu, K. Feng, C. Zhang, X. Feng, Z. YIping and L. Chen, *Int. J. Biol. Macromol.*, 2023, DOI: 10.1016/j.ijbiomac.2023.125891.

149 J. X. Ren, J. L. Zhu, S. C. Shi, M. Q. YIn, H. D. Huang and Z. M. LI, *Carbohydr. Polym.*, 2022, **296**, 119957.

150 X. Qi, X. Xiong, M. Liu, Y. Zhang, X. Zhang, P. Jiang, Y. Wu, X. Guo and H. Tong, *Carbohydr. Polym.*, 2024, **326**, 121623.

151 S. Kang, M. Chen, Y. Wang, F. Tang, Y. Liu, L. Cui and M. Dong, *Sustain. Energy Fuels*, 2022, **7**, 409–419.

152 D. Zhu, S. Handschuh-Wang and X. Zhou, Recent progress in fabrication and application of polydimethylsiloxane sponges, *J. Mater. Chem. A*, 2017, **5**, 16467–16497.

153 P. Zhou, B. Qin, L. Zhang, Z. Wu, Y. Dai, C. Hu, H. Xu and Z. Mao, *Int. J. Biol. Macromol.*, 2023, **239**, 124233.

154 J. You, C. Liu, X. Feng, B. Lu, L. Xia and X. Zhuang, *Carbohydr. Polym.*, 2022, **288**, 119332.

155 E. F. Assanvo, S. Nagaraj, D. Boa and P. Thanikaivelan, *Sci. Rep.*, 2023, **13**, 13365.

156 L. Xia, L. Shi, J. Zhao, C. Liu, Y. Di and X. Zhuang, *Front. Chem. Sci. Eng.*, 2025, **19**, 33.

157 S. Nardecchia, D. Carriazo, M. L. Ferrer, M. C. Gutiérrez and F. del Monte, *Chem. Soc. Rev.*, 2013, **42**, 794–830.

158 L. Chen, S. Liu, X. Guo, S. Wang, Z. He, Q. Xu, Q. Zhang, J. Zhu, P. Zhao, S. Yang and Q. Wang, *Sep. Purif. Technol.*, 2024, **330**, 125192.

159 N. Amaly, A. Y. EL-Moghazy, N. Nitin, G. Sun and P. K. Pandey, *Chem. Eng. J.*, 2022, **430**, 133077.

160 B. Yan, Y. Dai, Y. Li, L. Xin, M. Li, H. Long and X. Gao, *Int. J. Biol. Macromol.*, 2025, **306**, 141748.

161 X. Zou, L. Yao, S. Zhou, G. Chen, S. Wang, X. Liu and Y. Jiang, *Carbohydr. Polym.*, 2022, **296**, 119970.

162 J. Pan, D. Hua, Y. Hong, X. Cheng, F. Guo, K. Bing Tan, Z. Zhong and G. Zhan, *Chem. Eng. J.*, 2023, **466**, 143164.

163 C. N. Rani, S. Karthikeyan and S. Prince Arockia Doss, *Chem. Eng. Process. Process Intensif.*, 2021, **165**, 108445.

164 W. Lu, C. Duan, Y. Zhang, K. Gao, L. Dai, M. Shen, W. Wang, J. Wang and Y. Ni, *Carbohydr. Polym.*, 2021, **258**, 117676.

165 E. J. M. Dantas, M. E. Alves, S. Arias, A. G. Camara, J. V. F. L. Cavalcanti, G. L. Silva, C. M. B. M. Barbosa and J. G. A. Pacheco, *Catal. Today*, 2024, **441**, 114846.

166 H. Wu, T. Inaba, Z.-M. Wang and T. Endo, *Appl. Catal. B Environ.*, 2020, **276**, 119111.

167 A. Rajeswari, S. Vismaiya and A. Pius, *Chem. Eng. J.*, 2017, **313**, 928–937.

168 Z. Yin, X. Chen, T. Zhou, M. Xue, M. Li, K. Liu, D. Zhou, J. Ou, Y. Xie, Z. Ren, Y. Luo and Z. Hong, *Sep. Purif. Technol.*, 2022, **286**, 120504.

169 T. Li, N. Tsubaki and Z. Jin, *J. Mater. Sci. Technol.*, 2024, **169**, 82–104.

170 H. Hou, X. Zeng and X. Zhang, *Angew. Chem., Int. Ed.*, 2020, **59**, 17356–17376.

171 D. Majhi, K. Das, R. Bariki, S. Padhan, A. Mishra, R. Dhiman, P. Dash, B. Nayak and B. G. Mishra, *J. Mater. Chem. A*, 2020, **8**, 21729–21743.

172 M. Zhou, J. Chen, C. Hou, Y. Liu, S. Xu, C. Yao and Z. Li, *Appl. Surf. Sci.*, 2019, **470**, 908–916.

173 P. Wang, Z. Geng, J. Gao, R. Xuan, P. Liu, Y. Wang, K. Huang, Y. Wan and Y. Xu, *J. Mater. Chem. A*, 2015, **3**, 1709–1716.

174 Y. Chen, W. Shao, C. Zhou, G. Tai, G. Wu and W. Xing, *ACS Appl. Energy Mater.*, 2023, **6**, 11705–11717.

175 D. Ke, S. Liu, K. Dai, J. Zhou, L. Zhang and T. Peng, *J. Phys. Chem. C*, 2009, **113**, 16021–16026.

176 L. Zheng, K. Zhong, X. Huang and X. Qian, *Cellulose*, 2024, **31**, 2523–2540.

177 J. Zhou, T. Shan, S. Wu, J. Li, F. Zhang, L. Huang, L. Chen and H. Xiao, *Chem. Eng. J.*, 2024, **492**, 152441.

178 J. Li, Y. Xiao, S. Gu, K. Wu, X. Zhao, X. Zhao, J. Nan and X. Xiao, *Chem. Eng. J.*, 2024, **480**, 147969.

179 A. Balakrishnan, E. S. Kunnel, R. Sasidharan, M. Chinthala and A. Kumar, *ACS Sustain. Chem. Eng.*, 2024, **12**(13), 5169–5185.

180 S. Belda-Marco, P. Ayala, S. N. Myakala, D. Eder, M. Á. Lillo-Ródenas, A. Cherevan and M. C. Román-Martínez, *Environ. Res.*, 2025, **271**, 121141.

181 Z. Chen, D. Yao, C. Chu and S. Mao, *Chem. Eng. J.*, 2023, **451**, 138489.

182 L. Deng, J. Sun, J. Sun, X. Wang, T. Shen, R. Zhao, Y. Zhang and B. Wang, *Appl. Surf. Sci.*, 2022, **597**, 153586.

183 Y. Wu, S. Yan, L. Wang, L. Chen, Y. Li and K. Shen, *Appl. Catal. B Environ. Energy*, 2025, **375**, 125418.

184 G. Zhang, X. Rong, W. Huang, Z. Xiao, Z. Xue, H. Cheng, J. Feng and L. Li, *Colloids Surf., A*, 2025, **709**, 136202.

5516 | *J. Mater. Chem. A*, 2026, **14**, 5473–5519

This journal is © The Royal Society of Chemistry 2026

185 X. Wang, S. Yuan, B. Feng, X. Qiu, C. Yu, W. Lu, X. Xu, Y. Hu and Y. Shi, *J. Colloid Interface Sci.*, 2025, **691**, 137371.

186 W. Miao, D. Yao, C. Chu, Y. Liu, Q. Huang, S. Mao and K. (Ken) Ostrikov, *Appl. Catal. B Environ.*, 2023, **332**, 122770.

187 J. Zhou, T. Shan, F. Zhang, B. Boury, L. Huang, Y. Yang, G. Liao, H. Xiao and L. Chen, *Adv. Fiber Mater.*, 2024, **6**, 387–400.

188 L. Xu, Y. Liu, L. Li, Z. Hu and J. C. Yu, *ACS Catal.*, 2021, **11**, 14480–14488.

189 Y. Liu, X. Wang, Y. Zhao, Q. Wu, H. Nie, H. Si, H. Huang, Y. Liu, M. Shao and Z. Kang, *Nano Res.*, 2022, **15**, 4000–4007.

190 H. Tripathy, A. Balakrishnan, M. Chinthala and A. Kumar, *Ind. Eng. Chem. Res.*, 2024, **63**, 20125–20143.

191 S. Patnaik, D. P. Sahoo and K. Parida, *Carbon*, 2021, **172**, 682–711.

192 P. Chen, X. Dong, M. Huang, K. Li, L. Xiao, J. Sheng, S. Chen, Y. Zhou and F. Dong, *ACS Catal.*, 2022, **12**, 4560–4570.

193 D. Liu, L. Jiang, D. Chen, Z. Hao, B. Deng, Y. Sun, X. Liu, B. Jia, L. Chen and H. Liu, *ACS Catal.*, 2024, **14**, 5326–5343.

194 C. Shi, L. Zhang, Z. Shi, J. Ma and Z. Wang, *Ind. Crops Prod.*, 2022, **186**, 115223.

195 H. Maimaiti, A. Awati, G. Yisilamu, D. Zhang and S. Wang, *Appl. Surf. Sci.*, 2019, **466**, 535–544.

196 L. Wang, L. Zang, F. Shen, J. Wang, Z. Yang, Y. Zhang and L. Sun, *J. Colloid Interface Sci.*, 2022, **622**, 336–346.

197 Y. Sun, Y. Ahmadi, K.-H. Kim and J. Lee, *Renew. Sustain. Energy Rev.*, 2022, **170**, 112967.

198 J. Liu, S. Wang, C. Zhao and J. Zheng, *Nanomaterials*, 2023, 499, DOI: 10.3390/nano13030499.

199 Z. Shen, F. Li, J. Lu, Z. Wang, R. Li, X. Zhang, C. Zhang, Y. Wang, Y. Wang, Z. Lv, J. Liu and C. Fan, *J. Colloid Interface Sci.*, 2021, **584**, 174–181.

200 Z.-Y. Wang, B. Yuan, F.-G. Zhang, Y. Chen, J.-P. Tang, L. Bao and Y.-J. Yuan, *Inorg. Chem.*, 2024, **63**, 9715–9719.

201 T. Liu, L. Sun, Z. Cao, Y. Xue, X. Lu, C. Yao and X. Li, *J. Alloys Compd.*, 2023, **962**, 171181.

202 A. Balakrishnan, S. Appunni, M. Chinthala, M. M. Jacob, D. V. N. Vo, S. S. Reddy and E. S. Kunnel, *Environ. Chem. Lett.*, 2023, **21**, 1881–1905.

203 A. Balakrishnan, S. Appunni, M. Chinthala and D. Viet, *Environ. Chem. Lett.*, 2022, **20**, 3071–3098.

204 H. Liu, C. Wang and G. Wang, *Chem.–Asian J.*, 2020, **15**, 3239–3253.

205 X. Yan, M. Chen, J. Wang, Z. Wang, R. Xin, D. Wu, Y. Song, S. Li, W. Zhu, C. Wang and Y. Mao, *Chem. Eng. J.*, 2024, **495**, 153431.

206 M. Li, P. Zhang, J. Mao, J. Li, D. Wang, B. Xu, J. Zhou, J. Zhang, Q. Cao, Y. Zhang and H. Xiao, *Desalination*, 2025, **600**, 118497.

207 L. Tian, Y. Feng, X. Chen, H. Wang, J. Lin, W. Shi, L. Wei, W. Xia, Q. Sun, Y. Yang and Y. Li, *Int. J. Biol. Macromol.*, 2025, **286**, 138377.

208 J. Lin, D. Gao, J. Zeng, Z. Li, Z. Wen, F. Ke, Z. Xia and D. Wang, *Int. J. Biol. Macromol.*, 2024, **269**, 131994.

209 Y. Wang, J. Yang, Z. Zhang, P. Zhao, Y. Chen, Y. Guo and X. Luo, *Int. J. Biol. Macromol.*, 2024, **269**, 131885.

210 B. Sarkodie, E. K. Howard, Q. Feng, C. Xu and Y. Hu, *Ceram. Int.*, 2024, **50**, 21951–21957.

211 M. Ezzine, A. S. El-Shafie, K. M. Youssef and M. El-Azazy, *Int. J. Biol. Macromol.*, 2025, **306**, 141753.

212 J. Li, Y. Ning, X. Liu, X. Ren and W. Liu, *Cellulose*, 2024, **31**, 1827–1841.

213 X. Yang, C. Hu, X. An, X. Chen and C. Ding, *J. Alloys Compd.*, 2024, **1003**, 175594.

214 A. Saha and S. Varanasi, *Appl. Nanosci.*, 2024, **14**, 675–686.

215 L. Kumalayanti, W. Khamhom, N. Chankhunthod, P. Kidkhunthod and S. Pinitsoontorn, *Radiat. Phys. Chem.*, 2024, **221**, 111757.

216 N. P. de Moraes, R. A. Pereira, T. V. C. da Silva, B. H. B. da Silva, G. P. de Assis, T. M. B. Campos, G. P. Thim, M. R. de Vasconcelos Lanza, L. de Freitas and L. A. Rodrigues, *Int. J. Biol. Macromol.*, 2024, **254**, 127826.

217 X. Qi, X. Xiong, H. Cai, X. Zhang, Q. Ma, H. Tan, X. Guo and H. Lv, *Carbohydr. Polym.*, 2024, **346**, 122601.

218 W. Leng, X. Jiang, S. He, X. Wang, S. Zhai, J. Shi and X. Zhang, *Int. J. Biol. Macromol.*, 2024, **283**, 137948.

219 M. Bansal and B. Pal, *Int. J. Biol. Macromol.*, 2025, **285**, 138329.

220 V.-D. Doan, T. T. N. Nguyen, H. A. Le Pham, T. L. H. Nguyen, O. E. Lebedeva, H. P. Dang, A.-T. Nguyen, V. A. Tran and V. T. Le, *J. Mol. Liq.*, 2024, **398**, 124261.

221 W. Cui, S. Luo, H. Hou, Z. Wu, B. An, M. Xu, C. Ma, S. Liu and W. Li, *Ceram. Int.*, 2024, **50**, 52218–52227.

222 S. Elbakry, F. A. Alharthi, A. A. Abutaleb, M. Alshareef, K. Althumayri and M. E. A. Ali, *J. Mater. Res.*, 2024, **39**, 3218–3231.

223 X. Yang, Y. Ci, P. Zhu, T. Chen, F. Li and Y. Tang, *Int. J. Biol. Macromol.*, 2024, **274**, 133201.

224 P. Charurungsipong, B. Than-ardna and H. Manuspiya, *Int. J. Biol. Macromol.*, 2024, **283**, 137738.

225 C. Duan, X. Liu, G. Tian, D. Zhang, Y. Wen, Y. Che, Z. Xie and Y. Ni, *Int. J. Biol. Macromol.*, 2024, **274**, 133317.

226 Y. Peng, H. Zhou, Y. Wu, Z. Ma, R. Zhang, H. Tu and L. Jiang, *J. Colloid Interface Sci.*, 2022, **609**, 188–199.

227 M. N. Morshed, S. Al Azad, H. Deb, B. B. Shaun and X. L. Shen, *J. Water Process Eng.*, 2020, **33**, 101062.

228 Z. Lin and J. Huang, *Sep. Purif. Technol.*, 2021, **264**, 118427.

229 L. Lebogang, R. Bosigo, K. Lefatshe and C. Muiva, *Mater. Chem. Phys.*, 2019, **236**, 121756.

230 D. Wang, J. Yang, H. Yang, P. Zhao and Z. Shi, *Carbohydr. Polym.*, 2022, **296**, 119960.

231 S. I. Othman, H. E. Alfassam, H. A. Alqhtani, M. A. Al-Waili, A. A. Allam and M. R. Abukhadra, *Int. J. Biol. Macromol.*, 2024, **265**, 130615.

232 G. Tian, C. Duan, S. Che, B. Zhao, B. Zhou and Y. Ni, *Sep. Purif. Technol.*, 2025, **354**, 129183.

233 Y. Wu, Y. Li, T. Zhao, X. Wang, V. I. Isaeva, L. M. Kustov, J. Yao and J. Gao, *Carbohydr. Polym.*, 2022, **296**, 119969.

234 Y.-D. Dong, L.-Q. Zhang, P. Zhou, Y. Liu, H. Lin, G.-J. Zhong, G. Yao, Z.-M. Li and B. Lai, *J. Hazard. Mater.*, 2022, **423**, 127054.

This journal is © The Royal Society of Chemistry 2026

J. Mater. Chem. A, 2026, **14**, 5473–5519 | 5517

235 J.-L. Zhu, M.-L. Wang, S.-C. Shi, J.-X. Ren, H.-D. Huang, W. Lin and Z.-M. Li, *Cellulose*, 2022, **29**, 1929–1942.

236 Y. Li, H. Cao, W. Liu and P. Liu, *Chemosphere*, 2022, **307**, 135665.

237 J. Gao, W. Chen, H. Shi, Z. Li, L. Jing, C. Hou, J. Wang and Y. Wang, *Surf. Interfaces*, 2022, **34**, 102302.

238 Z. Zhao, X. Cai, S. Fan, Y. Zhang, Z. Huang, H. Hu, J. Liang and Y. Qin, *J. Alloys Compd.*, 2021, **877**, 160260.

239 S. Patial, Sonu, S. Thakur, Q. Van Le, T. Ahamad, P. Singh, V.-H. Nguyen, A. A. P. Khan, C. M. Hussain and P. Raizada, *J. Taiwan Inst. Chem. Eng.*, 2023, **153**, 105189.

240 X. Yan and X. Qian, *Int. J. Biol. Macromol.*, 2024, **283**, 137978.

241 Y. Chen, R. Su, F. Wang, W. Zhou, B. Gao, Q. Yue and Q. Li, *Chemosphere*, 2021, **270**, 129295.

242 T. T. Van Nguyen, Q. K. Nguyen, N. Q. Thieu, H. D. T. Nguyen, T. G. T. Ho, B. L. Do, T. T. P. Pham, T. Nguyen and H. Ky Phuong Ha, *Heliyon*, 2023, **9**(11), e22319.

243 D. Karadeniz, N. Kahya and F. B. Erim, *J. Photochem. Photobiol., A*, 2022, **428**, 113867.

244 W. Chen, T. Zhou, D. Gu, Y. He, Z. Zhang, J. Tian and F. Fu, *Appl. Surf. Sci.*, 2023, **637**, 157955.

245 K. Li, X. Zhang, X. Huang, X. Li, Q. Chang, J. Wang, S. Deng and G. Zhu, *Environ. Sci. Pollut. Res.*, 2024, **31**, 23924–23941.

246 G. Tian, C. Duan, B. Zhou, C. Tian, Q. Wang and J. Chen, *Front. Chem. Sci. Eng.*, 2023, **17**, 930–941.

247 G. Wu, S. Bian, J. Wang, T. Xu, Y. Pan, J. Han, W. Xing and H. Bian, *J. Mol. Struct.*, 2025, **1340**, 142613.

248 K. Li, X. Zhang, J. Wang, L. Guo, S. Deng, T. Xie, J. Wang and G. Zhu, *J. Photochem. Photobiol., A*, 2026, **470**, 116616.

249 C. Wu, T. Guo, Y. Chen, Q. Tian, Y. Zhang, Z. Huang, H. Hu and T. Gan, *Sep. Purif. Technol.*, 2024, **329**, 125174.

250 K. Li, X. Zhang, X. Huang, X. Li, Q. Chang, S. Deng and G. Zhu, *J. Water Process Eng.*, 2024, **63**, 105442.

251 N. Thi Mai, D. Van Thanh, N. Nhat Huy, D. Danh Bich, T. Thi Minh Hang, N. Huu Hao and N. Manh Khai, *Sep. Purif. Technol.*, 2025, **354**, 129039.

252 Y. Peng, H. Tang, B. Yao, X. Gao, X. Yang and Y. Zhou, *Chem. Eng. J.*, 2021, **414**, 128800.

253 X. Li, B. Jie, H. Lin, Z. Deng, J. Qian, Y. Yang and X. Zhang, *J. Environ. Manage.*, 2022, **308**, 114664.

254 F. Ghanbari and M. Moradi, *Chem. Eng. J.*, 2017, **310**, 41–62.

255 W. Ren, J. Gao, C. Lei, Y. Xie, Y. Cai, Q. Ni and J. Yao, *Chem. Eng. J.*, 2018, **349**, 766–774.

256 Y. Han, L. Gan, H. Gong, J. Han, W. Qiao and L. Xu, *Biochar*, 2022, **4**, 35.

257 W. Yang, L. Yang, Y. Yang, C. Fu, C. Sheng and P. Zhang, *Cellulose*, 2024, **31**, 3221–3242.

258 L. Gan, Q. Zhong, A. Geng, L. Wang, C. Song, S. Han, J. Cui and L. Xu, *Sci. Total Environ.*, 2019, **694**, 133705.

259 Z. Zhang, J. Wang, H. Zhang, Y. Deng, B. Tan, J. Wang, T. Yang and W. Wang, *Appl. Surf. Sci.*, 2024, **671**, 160717.

260 F. Nekouei, S. Nekouei and H. Kargarzadeh, *Chem. Eng. J.*, 2018, **335**, 567–578.

261 K. Zheng and L. Xiao, *Int. J. Biol. Macromol.*, 2023, **248**, 125902.

262 W. Sun, K. Thummavichai, D. Chen, Y. Lei, H. Pan, T. Song, N. Wang and Y. Zhu, *Polymers*, 2021, **13**, 1–14.

263 R. Su, Z. Wang, M. Zhao, F. Xiao, L. Zhang, L. Yang, Z. Wu, J. Bai and P. He, *J. Alloys Compd.*, 2023, **968**, 171896.

264 Y. Lin, Q. Wang, Y. Huang, J. Du, Y. Cheng, J. Lu, Y. Tao and H. Wang, *Int. J. Biol. Macromol.*, 2023, **247**, 125559.

265 Y. Wang, L. Ma, F. Xu, R. Ren, J. Wang and C. Hou, *Carbohydr. Polym.*, 2022, **298**, 120100.

266 X. Xue, Z. Sui, Y. Zou, C. Sun, F. Sefat, P. Coates, W. Zhang and C. Lu, *Carbohydr. Polym.*, 2025, **358**, 123508.

267 Y. Zhang, H. Zhang, J. Yao, Y. Song, W. Li and X. Xuan, *Chem. Eng. J.*, 2024, **483**, 149326.

268 S. Zhang, M. Zhao, H. Li, C. Hou and M. Du, *Cellulose*, 2021, **28**, 3585–3598.

269 J. He, A. Kumar, M. Khan and I. M. C. Lo, *Sci. Total Environ.*, 2021, **758**, 143953.

270 Y. Ding, G. Yang, S. Zheng, X. Gao, Z. Xiang, M. Gao, C. Wang, M. Liu and J. Zhong, *J. Environ. Manage.*, 2024, **366**, 121875.

271 K. Maślana, T. Kędzierski, A. Żywicka, B. Zielińska and E. Mijowska, *Environ. Nanotechnol., Monit. Manage.*, 2022, **17**, 100656.

272 J. Wang, C. Huang, Y. Tu, Z. Chen, Y. Zhao and Y. Ke, *Int. J. Biol. Macromol.*, 2025, **309**, 143019.

273 H. M. Abd El-Lateef, M. M. Khalaf, M. A. Alsaeed, M. F. Abou Taleb and M. Gouda, *Int. J. Biol. Macromol.*, 2024, **282**, 137410.

274 C. Huang, M. Xiao, H. Cui, J. Wang, Y. Cai and Y. Ke, *Int. J. Biol. Macromol.*, 2023, **252**, 126495.

275 N. Janpetch, C. Vanichvattanadecha and R. Rujiravanit, *Cellulose*, 2015, **22**, 3321–3335.

276 H. Shen, S. Liao, C. Jiang, J. Zhang, Q. Wei, R. A. Ghiladi and Q. Wang, *Carbohydr. Polym.*, 2022, **277**, 118853.

277 L.-P. Liu, X.-N. Yang, L. Ye, D.-D. Xue, M. Liu, S.-R. Jia, Y. Hou, L.-Q. Chu and C. Zhong, *Carbohydr. Polym.*, 2017, **174**, 1078–1086.

278 Y. D. Chai, Y. L. Pang, S. Lim and W. C. Chong, *Mater. Today Proc.*, 2021, **42**, 50–55.

279 M. Bachmann and M. Bachmann, *From Life Cycle Assessment to Absolute Environmental Sustainability of Plastics from Alternative Carbon Feedstocks Von der Lebenszyklusanalyse zu absoluter ökologischer Nachhaltigkeit von Kunststoffen aus alternativen Kohlenstoffquellen.*

280 A. Sudheshwar, K. Vogel, G. Nyström, N. Malinverno, M. Arnaudo, G. Enrique, R. Hischier and C. Som, *RSC Sustain.*, 2024, **5**, 1487–1497.

281 F. Foroughi, E. R. Ghomi, F. M. Dehaghi, R. Borayek and S. Ramakrishna, *Materials*, 2021, **14**, 714.

282 P. G. Stampino, L. Riva, C. Punta, G. Elegir, D. Bussini and G. Dotelli, *Molecules*, 2021, **26**, 2558.

283 A. salah omer, G. A. El Naeem, A. I. Abd-Elhamid, O. O. M. Farahat, A. A. El-Bardan, H. M. A. Soliman and A. A. Nayl, *J. Mater. Res. Technol.*, 2022, **19**, 3241–3254.

284 A. Wilcox, M. Hall, J. Menzies, N. Yates, J. Price, T. Neal, S. Stilianoudakis, S. Isaacs, Y. Sun, M. Sivik and K. McDonough, *Sci. Total Environ.*, 2025, **991**, 179942.

5518 | *J. Mater. Chem. A*, 2026, **14**, 5473–5519

This journal is © The Royal Society of Chemistry 2026

285 J. Belhaj, R. Khiari, V. García-Caballero, A. A. Romero and A. García, *Polymers*, 2025, **17**(13), 1737.

286 A. Singh, J. G. Vijayan and K. G. Moodley, Surface Functionalizations of Nanocellulose for Wastewater Treatment, in *Handbook of Nanocelluloses*, ed. A. Barhoum, 2021, Springer, Cham, DOI: 10.1007/978-3-030-62976-2_49-1.

287 A. Sánchez-Yepes, A. Santos, J. M. Rosas, J. Rodríguez-Mirasol, T. Cordero and D. Lorenzo, *Chemosphere*, 2023, **341**, 140047.

288 J. Shaheen, Y. H. Fseha and B. Sizirici, *Heliyon*, 2022, **8**(12), e12388.

289 X. Li, L. Zhang, Z. Wang, S. Wu and J. Ma, *Colloids Surf., A*, 2022, **636**, 128156.

290 Y. Y. Dong, Y. H. Zhu, M. G. Ma, Q. Liu and W. Q. He, *Sci. Rep.*, 2021, **11**, 3366.

291 F. Business Reports, Cellullose Market, https://www.fortunebusinessinsights.com/cellulose-market-102062.

This journal is © The Royal Society of Chemistry 2026

J. Mater. Chem. A, 2026, **14**, 5473–5519 | 5519